Forschungszentrum Jülich

Institut für Festkörperforschung

Femtosecond electron dynamics of image-potential states on the transition-metal surfaces of Pt and Ni

Sven Link

Jül-3878

Femtosecond electron dynamics of image-potential states on the transition-metal surfaces of Pt and Ni

Sven Link

Berichte des Forschungszentrums Jülich ; 3878
ISSN 0944-2952
Institut für Festkörperforschung Jül-3878
D 38 (Diss., Köln, Univ., 2001)

Zu beziehen durch: Forschungszentrum Jülich GmbH · Zentralbibliothek
52425 Jülich · Bundesrepublik Deutschland
☎ 02461/61-5220 · Telefax: 02461/61-6103 · e-mail: zb-publikation@fz-juelich.de

Kurzfassung

Im Rahmen dieser Arbeit wurde der Einfluß der elektronischen Struktur auf das Relaxationsverhalten optisch angeregter Elektronen an Festkörperoberflächen untersucht. Mit der Methode der zeitaufgelösten 2-Photonen Photoemissionsspektroskopie ist es möglich, die Dynamik elektronischer Anregungen zu verfolgen. Der Schwerpunkt lag hierbei auf der Bestimmung der Beiträge von *d*-Bändern und Oberflächenzuständen auf den Populationszerfall und die Lebensdauern von sogenannten "Bildpotentialzuständen" in Übergangsmetallen. Bildpotentialzustände sind gebundene - normalerweise unbesetzte - elektronische Oberflächen- zustände, die im Vakuum vor der Oberfläche lokalisiert sind und energetisch - vergleichbar einer Rydbergserie beim Wasserstoffatom - gegen die Vakuumenergie konvergieren. Es wurde gezeigt, daß eine gezielte Veränderung der Oberfläche durch Adsorbate die Lebensdauern der Zustände, die im Femtosekundenbereich liegen, sowohl verlängern als auch verkürzen kann. Somit ist es möglich, elektronische Lebensdauern auf ultrakurzen Zeitskalen zu kontrollieren und zu be- einflussen.

Im speziellen wurden die ersten beiden Bildpotentialzustände auf der Pt(111) Oberfläche sowie der jeweils erste Bildpotentialzustand auf den (111) und (100) Orientierungen von Nickel untersucht.

Auf der Pt(111) Oberfläche wurden Lebensdauern von 26 ± 7 fs und 62 ± 10 fs für die ersten beiden Zustände gemessen, die um einen Faktor zwei nach Adsoption einer viertel Monolage Sauerstoff verkürzt werden. Dies läßt sich im wesentlichen durch eine Reorganisation der Valenzbandstruktur erklären, die knapp unterhalb des Ferminiveaus beobachtet wurde.

Die gemessenen Lebensdauern des jeweils ersten Bildpotentialzustandes auf den beiden Nickeloberflächen sind mit weniger als 20 fs deutlich kürzer verglichen mit solchen auf Edelmetalloberflächen. Dies ist auf den Einfluß von *d*-Zuständen zurückzuführen, die am Ferminiveau lokalisiert sind. Es wurde ein Modell entwickelt, mit dem sich die gemessenen Lebensdauern auf den Oberflächen von Übergangs- und Edelmetallen sehr gut beschreiben und voraussagen lassen.

Abstract

The influence of the electronic structure upon the relaxation dynamics of optically excited electrons has been investigated on the transition metal surfaces of Pt and Ni. Using time-resolved two-photon photoemission spectroscopy the population dynamics of excited electronic states can be observed. It was the purpose of this thesis to extract the influence of d-band and surface-state contributions onto the dynamis and lifetimes of so called "image-potential states". Image-potential states are a special class of bound, normally unoccupied, electronic surface states. They are localized in the vacuum region in front of a metal surface and energetically converge - similar to the Rydberg series of a hydrogen atom - with quantum number n towards the vacuum energy. It has been demonstrated that changes in the surface geometry caused by adsorbates influence the lifetimes of those states, which typically lie in the femtosecond range. Our experiments show that the lifetimes of image states can be both lowered and increased depending on the the sort of atoms adsorbed at the surface. Therefore, it is possible to control lifetimes of surface states on ultrashort time scales.

In particular, we have investigated the first two image-potential states on the Pt(111) surface as well as the first state ($n = 1$) on the (111) and (100) orientations of Ni.

On Pt(111), lifetimes of 26 ± 7 and 62 ± 10 fs have been measured for the first two image states, respectively. The adsorption of a quarter of a monolayer leads to a reduced lifetime for both states by a factor of 2. This decrease can be explained by the redistribution of the density of states close below the Fermi energy.

The observed lifetimes of < 20 fs for the first image-potential state on Ni(100) and Ni(111) are significantly shorter compared to those on Pd, Pt and the noble metals Cu and Ag. This can be essentially attributed to the high density of states of d-bands at the Fermi level, which contribute to the population decay. In order to understand the lifetimes of image-potential states on the transition and noble metal surfaces, a model has been developed which is able to describe the observed lifetimes reasonably well and allows to predict up to now unmeasured lifetimes.

Contents

Chapter 1

Introduction

The time resolution of the human eye is limited to ≈50 ms. It is, therefore, not suited for the investigation of dynamic processes on shorter timescales. We meet this restriction in time resolution in our daily life. Watching movies is only enjoyable since the repetition rate of the pictures exceeds 20 Hz. A variety of methods has been developed for the investigation of processes that happen on μs or even shorter timescales. The common problem concerning the investigation of ultrafast dynamics is the available temporal resolution. For instance, high-tech electronic instruments provide a time resolution somewhat better than 100 picoseconds (ps). However, a lot of interesting and important phenomena in physics and chemistry happen on ps and femto second (fs) timescales [1, 2, 3, 4, 5].

The development of femtosecond-laser systems opened the door to study ultrafast dynamical processes which range from relaxation dynamics of charge carriers in solids [1, 4] to the formation or breaking of chemical bonds in molecules [5]. Typically pulses are about 100 fs long, presently the shortest is 4.5 fs [6].

The field of femtosecond spectroscopy is a remarkable and fascinating new topic in science. It has met great fundamental and technological interest and opens a wide range of research in different fields of physics and chemistry. Consequently, one of the pioneers in femtosecond chemistry, A. Zerwail, was awarded the Nobel Prize in chemistry in 1999.

Femtosecond spectroscopy is based on the pump-probe technique. Two individual fs-laser pulses, which can be delayed in time with respect to each other, are used to excite (pump) and probe the physical system. A characteristics of this approach is that the investigated system is no longer in thermodynamic equilibrium. After excitation by the pump pulse, the system is in an excited state whose decay into other degrees of freedom is being probed. The observed state at a given pump-probe delay can thus be regarded as a "snapshot" of the momentaneous condition of the system. Hence, fs spectroscopy is also referred to as the "fastest camera in the world".

A challenging aim of current research is the investigation and understanding

of electron dynamics at surfaces and interfaces after optical excitation [7, 8, 9]. Electron-hole excitations play a key role in a variety of phenomena such as surface chemistry [10], charge transport [11], electron stimulated desorption [10], and device physics [1, 12]. Moreover, it has been demonstrated that hot electron distributions govern the demagnetization of ferromagnetic thin films via spin flip processes and the creation of magnons [13].

Time-resolved 2-photon photoemission spectroscopy (TR2PPE) is a powerful technique for investigating ultrafast electron dynamics with the unique possibility of directly studying the population of normally unoccupied electronic states. This is the main advantage compared to "indirect" optical techniques such as measuring the transient absorption [14] or reflection [15].

Initially TR2PPE experiments with ps time resolution focused almost 20 years ago on the transient electron populations in conduction bands and normally unoccupied surface states on semiconductor surfaces in the fs regime [16, 17]. Advances in laser technology have finally enabled the observation of excited electronic-state lifetimes on a variety of metal surfaces [7, 8]. Before it was possible to use ultrafast lasers, the only method available for obtaining information about the electron lifetimes on metal surfaces was the measurement of spectroscopic linewidths.

The main difficulty with linewidth measurements is associated with the assumption that the linewidth is dominated by lifetime broadening. Interestingly, it has been shown that so called "dephasing" or "initial state" effects give rise to complicated and unexpected behaviour of the linewidth [18, 19, 20]. Therefore, lifetime measurements in the time domain are highly preferred. Recent TR2PPE experiments on a variety of metal surfaces focused on

- hot electron distributions above the Fermi level [4, 8, 11, 21],
- the transient response of the population of surface states [7, 22, 23].

The general aim of these time-resolved experiments is the determination and understanding of the scattering mechanisms which govern the decay of excited electrons. The relaxation time of excited electrons reflects a number of interactions such as electron-electron, electron-phonon, electron-plasmon, or electron-impurity scattering. In addition, it has been demonstrated that excited electronic states in metals influence chemical reactions [10] and open the possibility of observing adsorbate-atom motion above a metal surface in real time [2].

A special class of surface states are the so-called "image-potential states". These normally unoccupied states are similar to the highly excited Rydberg states in atoms or molecules. They occur if electrons are trapped close to a metal surface by their own positive image charge inside the metal. In analogy to the hydrogen atom, this gives rise to a series of novel electronic states with quantum numbers n converging towards the vacuum level E_{Vac}. Image-potential states are localized mainly in the vacuum. Parallel to the surface their wave functions are delocalized. With increasing n, electrons populating image-potential states are localized further and further in

the vacuum. For example, the $n = 7$ state on Cu(100) is localized about 200 Å away from the surface [24].

Image-potential states provide a useful model to study the interaction of surface electrons with the underlying substrate. This coupling is responsible for the cross-sections and branching ratios of all electronically induced adsorbate reactions at metal surfaces.

Recent research has focused on the dynamics of image-potential states on clean and adsorbate covered surfaces of Cu and Ag [7, 23, 25]. The observation of quantum-beats between coherently excited high-order image-potential states on Cu(100) [24] provide new information about binding energies and lifetimes of image-potential states with $n \geq 4$. By exciting electronic states close to the vacuum level, electron-wave packets are formed which travel more than 200 Å away from the surface and oscillates back. Moreover, those quantum beats provide information about dephasing by the loss of coherence in the quantum beats [26].

However, up to now almost no information is available about image-potential state dynamics on transition metal surfaces. Electron dynamics on these surfaces should provide additional information about the influence of *d*-bands and surface states on the decay of electrons populating image-potential states. The *d*-band contribution is of considerable interest since *d*-levels are responsible for magnetism on the transition metal surfaces of Fe, Co, and Ni.

Within this thesis we present first measurements of image-potential state dynamics on Pt and Ni surfaces in the time domain by using TR2PPE. The chapters in this thesis are arranged in the following way. First we give a short introduction into the experimental technique of TR2PPE in chapter 2. Chapter 3 provides a general overview about the physical properties of image-potential states such as lifetimes, effective masses and binding energies. Before we start the presentation of the measurements, the experimental setup is described in chapter 4. In chaper 5, the dynamics of the first two members of the image-potential series on the clean and oxygen covered Pt(111) surface will be presented. Our results will be compared with a theoretical calculation performed in collaboration with E.V. Chulkov et al.. The dynamics of the first image-potential state on the (100) and (111) faces of Ni are explored in chapter 6. In order to separate the various decay channels of the image-state population, hydrogen was adsorbed on the Ni(111) surface. In chapter 7, a comparison of $n = 1$ state lifetimes on various surfaces is given. It is the aim of this chapter to find a general trend by accounting for the wave-function penetration into the crystal and the electronic states involved into the decay. Finally, chapter 8 summarizes the results.

Chapter 2

Principles of photoemission

It is the scope of this section to give a short introduction into the techique of two-photon photoemission which has been used throughout this thesis to probe the dynamics of normally unoccupied electronic states after optical excitation. We start the description with an overview of direct and inverse photoemission spectroscopy. These techniques probe the occupied and unoccupied electronic levels, respectively. We then introduce two-photon photoemission as suitable tool for the direct investigation of electron dynamics in normally unoccupied electronic states.

2.1 Historical remarks

The interaction of light with matter, such as scattering or absorption of photons provides a variety of techniques for studying structural and electronic properties of solids. In particular, photoemission spectroscopy is one of the most powerful methods to probe electronic core levels, valence bands and the dispersion $E(k)$ of energy bands of solids and their surfaces.

The photoelectric effect was first observed by Hertz in 1887 [27]. He observed that an arc between two electrodes occurs more easily if the negatively biased electrode is illuminated with UV radiation. In the following years additional experiments were performed by Thompson [28] and Lenard[29], who showed unambiguously that the effect observed in Hertz's experiment can be explained by the emission of electrons. Moreover, Lenard found that the number of emitted electrons from an illuminated metal is proportional to the intensity of the incident light. However, the velocity of the emitted electrons depends on the wavelength of light, not on the light intensity. The observed behaviour could not be explained within the framework of the classical electromagnetic theory.

These observations led Einstein to postulate his theory of the photoelectric effect in 1905 [30], which was capable to explain the experiments of Lenard and Thompson. Within this theory only portions of light of an energy $E = h\nu$ could be absorbed by the sample where ν is the frequency of light and h denotes the Planck constant.

Therefore, the quantum nature of light and the existence of light particles, referred to as "photons", were established. For this work Einstein was awarded the Nobel Prize in Physics 16 years later in 1921.

The development of angle-resolved photoelectron spectroscopy [31] opened the door for detailed studies of the occupied electronic structure. Using this technique, the kinetic energy E and the momentum $\vec{k}$ of the emitted electron is measured such that the band structure of solids can be mapped. On the other hand, angle resolved inverse photoelectron spectroscopy has become a versatile method to expand the investigation to the unoccupied electronic structure [32]. The advent of fs-laser systems introduces time resolution in photoemission experiments. The new technique of time-resolved two-photon photoemission spectroscopy offers the opportunity of studying electron dynamics in real time. In addition, its improved energy resolution compared to inverse-photoemission experiments makes it favourable for the investigation of unoccupied electronic states.

2.2 Direct and inverse photoemission spectroscopy

The energy E of allowed electronic states in dependence of the electron wave vector $\vec{k}$ is referred to the electronic bandstructure $E(\vec{k})$. Due to the periodic crystal potential the dispersion relation $E(\vec{k})$ for the crystal electrons deviates from the dispersion relation for free electrons. The dispersion of energy bands in solids has been the focus of interest in the last years. A powerful tool to investigate the $E(\vec{k})$ dependence is the technique of angle resolved ultraviolet photoemission spectroscopy (ARUPS). Using this technique, both the kinetic energy and the emission angle of the photoemitted electrons are measured.

In order to obtain information about the electronic structure of a solid, it is illuminated with monochromatic light of energy $h\nu$. If the photon energy exceeds the work function, electrons can be excited into normally unoccupied states above the vacuum level E_{Vac} and can be photoemitted. Since the energy of an absorbed photon is completely transferred to the excited electron, the kinetic energy of the photoemitted electron is

$$E_{kin} = \hbar\omega - (E_{Vac} - E_F) + E_B = \hbar\omega - \Phi + E_B \tag{2.1}$$

where $E_B = E_F - E_{initial}$ denotes the binding energy relative to the Fermi level E_F. The photoemitted electrons can then be separated with respect to their kinetic energy and detected. From the obtained energy distribution curve (EDC) the position of the Fermi level[1], the vacuum level and the energy position of electronic states can

[1]It should be noted that the Fermi level can only be measured on metals. In many cases the binding energies for electronic states in semiconductors are also referenced to E_F, which then usually was taken from a reference metal sample. Thus E_F serves as a physical reference in solids. However, one should keep in mind that the kinetic energy is measured with respect to the vacuum level.

be obtained. The work function Φ of a metal sample is given by the width of the EDC between E_F and the low energy cutoff according to equation 2.1.

The inverse-photoemission process can be thought of as the time reversal to the process of direct photoemission [32]. In inverse-photoemission experiments a beam of monochromatized electrons hits the sample under a defined angle. The electrons injected into the sample occupy states above E_{Vac}. Such electrons in excited states may decay via radiative transitions to lower lying empty states between E_{Vac} and E_F. The emitted photons are counted and energy analyzed.

The process of photoemission is a quantum phenomenon and has, therefore, to be described within the theory of quantum mechanics. Since the optical perturbation due to the incident electromagnetic field of light is only small, the problem can be treated in first order perturbation theory. The transition probability per unit time for the excitation of an electron from the initial state $\mid i\rangle$ with energy $E_{initial}$ to an excited state $\mid f\rangle$ with energy E_{final} is then given by Fermi's Golden Rule as

$$w_{fi} = \frac{2\pi}{\hbar} \mid \langle f \mid H^{int} \mid i\rangle \mid^2 \delta(E_{final} - E_{initial} - \hbar\omega) \quad . \tag{2.2}$$

The δ-function guarantees the conservation of energy in the photoemission process. H^{int} is the Hamiltonian describing the interaction between the electron and the incident electromagnetic wave and can be written as

$$H^{int} = \frac{e}{2mc}(\vec{A}\cdot\vec{P} + \vec{P}\cdot\vec{A}) - e\varphi + \frac{e^2}{2mc^2} \mid \vec{A} \mid^2 \quad . \tag{2.3}$$

$\vec{A}$ and φ are the vector and skalar potentials of the incoming light. In general the diamagnetic term $\mid \vec{A} \mid^2$ is small and can be neglected. Further on, a gauge transformation could be found such that the skalar potential Φ can be set to zero.

2.2.1 The three-step model

The process of direct photoemission is often described in the so-called three-step model which is useful in the interpretation of photoemission spectra and relatively simple.

In a first step a photon is locally absorbed and its energy is transferred to a bound electron in an initial state $\mid i\rangle$ with energy $E_{initial}$ below the Fermi level E_F, which is excited into an unoccupied final state $\mid f\rangle$ with energy E_{final} above E_F. Here, the interaction between electron and photon is characterized by energy and momentum conservation:

$$E_{final} = E_{initial} + \hbar\omega \tag{2.4}$$

$$\vec{k}_{final} - \vec{k}_{initial} = \vec{K} + \vec{k}_{ph} \quad . \tag{2.5}$$

$\vec{k}_{final}$ and $\vec{k}_{initial}$ denote the electron momenta of the final and initial states, respectively. $\vec{K}$ represents a wave vector of the reciprocal lattice and can be neglected in

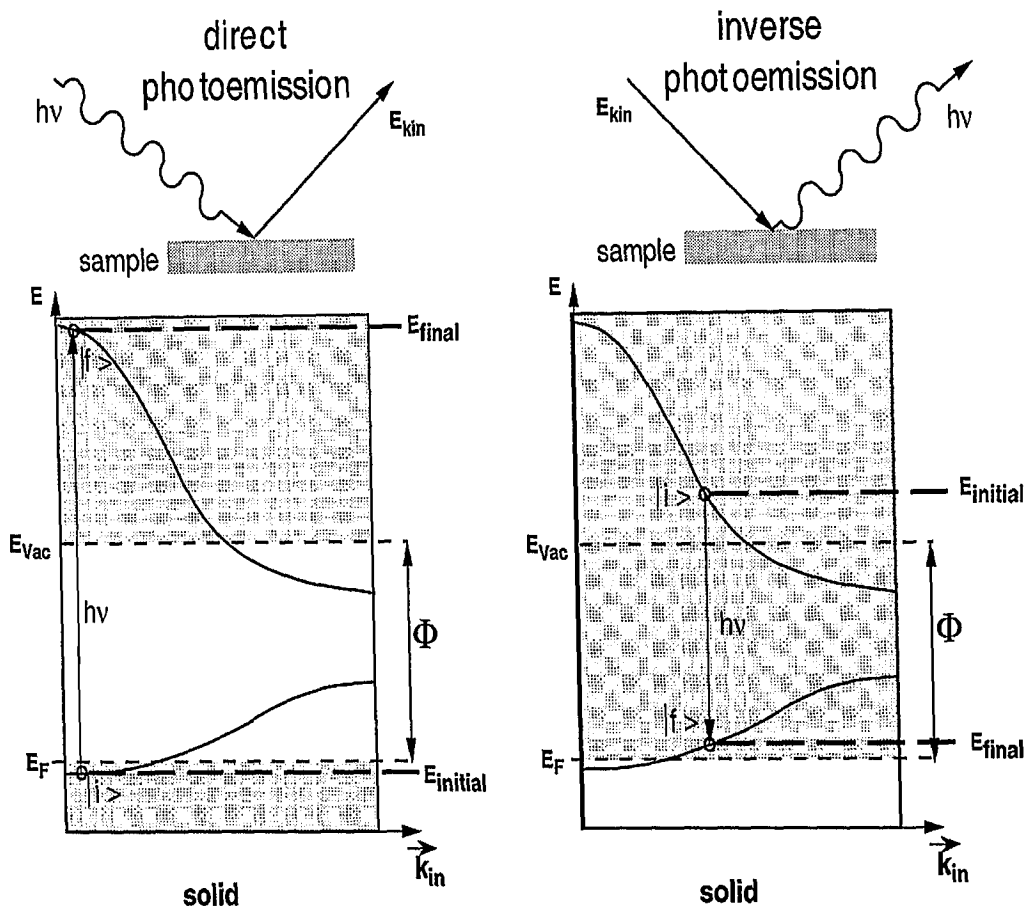

Figure 2.1: (**A**) In the photoemission process an electron is excited by the absorption of a photon with energy $E = \hbar\omega$. It can leave the surface and escape into the vacuum if the photon energy exceeds the work function Φ. Using this technique, one can probe states below E_F (initial state) and above E_{Vac} (final state). (**B**) The inverse photoemission process can be thought of the time reversal process of direct photoemission. This technique allows to probe bands in the energy range between E_F and E_{Vac} (final state) and bands at energies above E_{Vac}. Hatched areas denote electronic states which are accessible with direct (inverse) photoemission spectroscopy. In both processes, energy and momentum are conserved as described in the text.

the reduced scheme of the Brillouin zone. The wave vector of the photon, $\vec{k}_{ph}$, is rather small compared to those of electrons and to the expansion of the Brioullin zone and can also be neglected. Thus, only vertical transitions in the reduced scheme of the Brillouin zone are possible:

$$\vec{k}_{final} - \vec{k}_{initial} = 0 \quad . \tag{2.6}$$

In a second step the excited electron propagates through the sample to the surface. If now the state $\mid f\rangle$ lies energetically above the vacuum level E_{Vac}, the electron can finally couple to a free-electron like vacuum state, can leave the surface and escape into vacuum. The process of photoemission is schematically shown in the left panel of Fig. 2.1. The necessary condition for the last step implies that the photon energy, $\hbar\omega$, exceeds the work function, $\Phi = E_{Vac} - E_F$, of the sample.

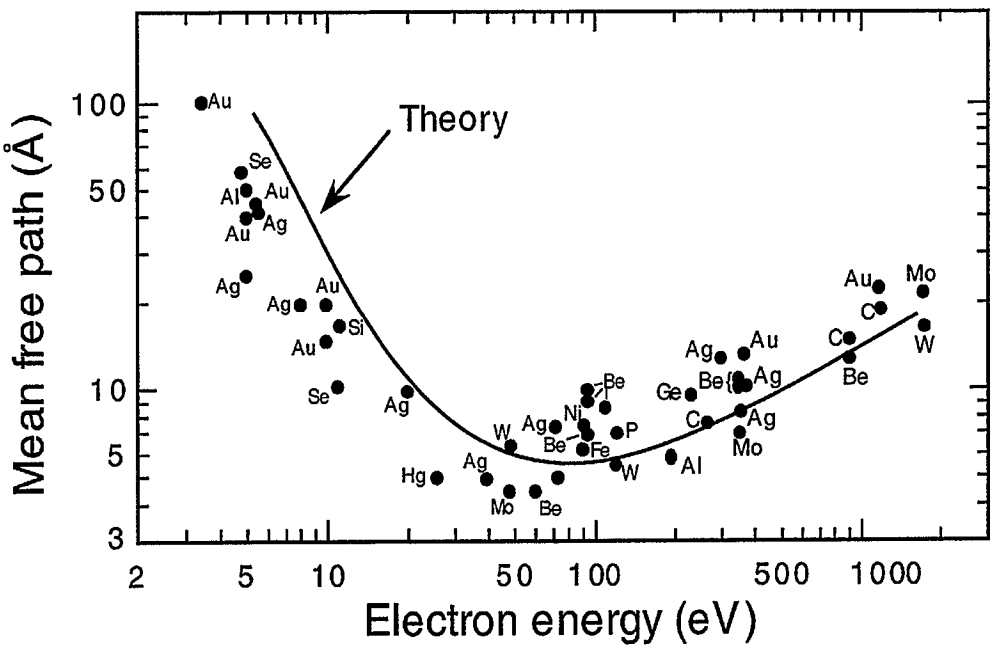

Figure 2.2: The mean free path of electrons in a solid plotted as function of their kinetic energy [33]. The curve shows an universal behaviour for all elements and is calculated by Penn [34]. The dots represent experimental data for the indicated elements [35]. By selecting the photon energy one is able to control the escape depth of electrons from the sample and the surface sensitivity of the experiment.

During the propagation to the surface the electrons can scatter inelastically with other electrons or phonons resulting in a loss of energy. However, if the energy loss

is small enough so that the electron energy remains above the vacuum level, the electron is still able to escape into the vacuum. This leads to a background in the energy distribution curve due to secondary electrons. The probability of such scattering events is described by the "mean free path" of electrons inside the solid. The mean free path of an electron is the statistical propagation length without inelastic scattering, that means without losing a fraction of its energy. Hence only electrons which are excited within a distance given by the mean free path away from the surface provide useful information about the electronic structure in a photoemission experiment. It is interesting to see that the mean free path of electrons is approximately independent of the material. This is shown in Fig. 2.2, where the kinetic energy of electrons is plotted versus the mean free path. The universal curve has a minimum of 4 Å around a kinetic energy of 50 eV and increases again towards lower and higher energies. The surface sensitivity of the photoemission experiment can then be controlled by the chosen photon energy.

When the electron leaves the surface (third step in the three-step model), one has to take into account the termination of the three-dimensional periodicity perpendicular to the surface. The momentum $\vec{k}$ of the electron can be divided into components parallel and perpendicular to the surface:

$$\vec{k} = \vec{k}_{\parallel} + \vec{k}_{\perp} \tag{2.7}$$

Since the period of the whole system is still conserved parallel to the surface the value of $\vec{k}_{\parallel}$ is unchanged and one obtains

$$\vec{k}_{\parallel}^{in} = \vec{k}_{\parallel}^{out} \tag{2.8}$$

$$\mid \vec{k}_{\parallel}^{in} \mid = \mid \vec{k}_{\parallel}^{out} \mid = \frac{\sqrt{2mE_{kin}}}{\hbar} cos(\vartheta) \tag{2.9}$$

where ϑ is the angle between the surface and the emitted electron. The question for the component perpendicular to the surface is more complex since this component is not conserved:

$$\mid \vec{k}_{\perp}^{in} \mid \neq \mid \vec{k}_{\perp}^{out} \mid \quad . \tag{2.10}$$

When the electron leaves the surface, its energy is renormalized. In the solid, the energy of the electron is referred to the inner potential which usually is close to the bottom of the valence band. After the photoemission process the kinetic energy of the electron is measured relativ to the vacuum level. Hence the value for $\mid \vec{k}_{\perp}^{out} \mid$ can be calculated by

$$\mid \vec{k}_{\perp}^{out} \mid = \frac{\sqrt{2m(E_{kin} + E_0 + \Phi)}}{\hbar} sin(\vartheta) \tag{2.11}$$

where E_0 is the, so called, inner potential of the sample.

Similar to the process of direct photoemission, the inverse photoemission process can be divided in three steps of reversal order. However, in this case the third step is characterized by energy and momentum conservation, i.e.

$$E_{final} = E_{initial} - \hbar\omega \tag{2.12}$$

$$\vec{k}_{final} - \vec{k}_{initial} = 0 \quad . \tag{2.13}$$

2.2.2 Linewidths measurements

The technological development in photoemission spectroscopy has made possible precise linewidth measurements of electronic states. State of the art electron analyzers possess an energy resolution below 100 meV, in some cases an energy resolution below 5 meV has been reported [36]. The intrinsic linewidth Γ and the lifetime τ of an electronic state are intimately connected through the relation

$$\Gamma = \frac{\hbar}{\tau} \quad . \tag{2.14}$$

Therefore, accurate linewidth studies provide information about elementary excitations and, thus, about dynamical processes such as the scattering length of electrons. Due to the finite spot of the light source on the sample, the photoemission experiment integrates over a relatively large area of the surface. Thus, the roughness of the surface, i.e. residual defects, steps and other imperfections, can be expected to increase the linewidth.

Another method for the investigation of electronic states is the spectroscopy with a scanning tunneling microscope (STM). Using this technique, in a first step an atomically resolved image of the surface is scanned. By selecting an almost perfect, defect free position on the surface, finally the current-voltage characteristics (scanning tunneling spectroscopy: STS) at this particular position is measured [36]. From the width of the steplike onset in the $\frac{dI}{dV}$ curve the linewidth of electronic states at their band minimum and, thus, their lifetimes can be determined [36, 37].

One should note, that, despite of the mentioned advantage in STS, recent high resolution photoemission and STS experiments yield almost identical values for the linewidths of occupied surface states[2] on noble metal surfaces [36, 37].

A major disadvantage in inverse photoemission experiments is the relatively low energy resolution (> 200 meV). Therefore, the linewidths of unoccupied electronic states can only be resolved with minor accuracy. This problem can be overcome by using the technique of two-photon photoemission spectroscopy, which provides an energy resolution as good as in direct photoemission experiments. This method is described below in the next section.

[2] A brief description of surface states will be given in the next chapter.

2.3 Investigation of electron dynamics after optical excitation

As described in the previous section, direct and inverse photoelectron spectroscopy are appropriate techniques for the investigation of the occupied and unoccupied electronic structure in solids, respectively. However, inverse photoemission spectroscopy probes "quasi static" processes and fails in the investigation of electron dynamics in normally unoccupied states. Therefore, additional methods are required for studying dynamics in states between E_F and E_{Vac}.

As soon as electrons are optically excited into normally empty states they start to interact with their environment since the physical system is now far away from thermal equilibrium. The excited electrons start to scatter in order to cool down. Those scattering events lead to a depopulation of the excited states induced through an energy transfer to the environment. In all possible relaxation mechanisms energy and momentum conservation is required. The relaxation pathways depend on the individual physical system and govern the time scale of the decay and lifetimes of excited electrons. On short time scales of up to 200 fs, the so called "coherent regime"[3] [38], electron-electron scattering dominates the relaxation dynamics. On longer timescales carrier-phonon scattering appear and is the most likely decay path. Note that a number of other mechanisms could be involved in the relaxation process, for instance electron-hole scattering, carrier-capture in quantum wells or carrier recombination. The measured lifetimes are therefore excellent hints for the involved decay channels and the involved final states in which the electrons are able to scatter.

A large number of experimental investigations in this field use the so called pump-probe technique. Here a first light pulse (pump pulse) is used to excite the electronic system whereas a second light pulse at variable time delay probes the momentary state.

2.3.1 Two-photon photoemission

If light of sufficient intensity interacts with matter, an electron can be excited simultaniously with twice the photon energy $\hbar\omega$ of the incoming light. This process is referred to as a two photon process or two-photon absorption. As a consequence, even if the work function Φ exceeds the photon energy, a photocurrent can be detected if $2\hbar\omega > \Phi$. The simultaneous absorption of two photons is a nonlinear process of second order. Thus, the probability of such a process is by far smaller than the excitation of an electron by only one photon. Accordingly, these processes are negligible in standard photoemission experiments which were described in the previous section. One has to distinguish between *nonresonant* and *resonant* processes. In a nonresonant process, the photocurrent I_{photo} due to two-photon pho-

[3] In the "coherent regime" the excited electrons retain their coherence among themselves and with the electromagnetic radiation.

toemission is proportional to the square of the light intensity I_{light}. If, for example, an unoccupied surface state[4] serves as intermediate state, the observed 2PPE intensity exceeds the I^2_{light} behaviour. The dependence of the photocurrent is linear in one-photon photoemission: $I_{photo} \propto I_{light}$.

Pulsed laser sources can generate light pulses with pulse energies of up to a few mJ which provide sufficient light intensities to cause two-photon processes and in a smaller extend three- and four-photon processes can occur[5]. In the following the description will mainly focus on two-photon processes.

Two-photon photoemission (2PPE) spectroscopy is similar to the above described technique of photoemission, but can give additional information of the electronic structure. A first photon of energy $h\nu_1$ excites an electron from an occupied state $|i\rangle$ below E_F into an unoccupied state $|n\rangle$ between E_F and E_{Vac}. A second photon with energy $h\nu_2$ lifts up the electron above the vacuum level into the final state $|f\rangle$ so that the electron can leave the surface and escape into the vacuum where its kinetic energy is analyzed. The distinction between ν_1 and ν_2 is necessary since both photons may have different energies and polarizations.

Furthermore, if the time delay between the two photons can be controlled, time resolution as an additional experimental parameter can be achieved since the population of state $|n\rangle$ can be probed through the second photon by varrying the time delay between photon 1 and photon 2. This is accomplished by the use of two ultrashort laser pulses as shown in Fig. 2.3(A). Time resolution is then determined by the temporal duration of the laser pulses. If both pulses have the same photon energy, $h\nu_1 = h\nu_2$, the experiment is referred to a $one - colour$ experiment, else it is called a $two - colour$ experiment.

Due to the high intensity of both light pulses, a variety of possible electronic transitions are expected to occur which contribute to the energy distribution curve in a 2PPE experiment. Let us assume that in a $two-colour$ experiment[6] both photon energies are smaller than the work function of the sample and both pulses arrive at the same time at the sample surface. There are four possibilities for transitions involving both pulses as sketched in Fig.2.3(B) in a schematic bandstructure.

Processes (1) Here only photons of one pulse take part in the photoemission process. Two photons with energy $h\nu_1$ are absorbed simultaneously and lift an electron above E_{Vac}. Since no electronic intermediate states are involved, this process is referred to a nonresonant process. Photoemission is only possible via a virtual state [39]. In this case, only occupied electronic states can be observed in the EDC.

[4]Surface states will be described in the next chapter.

[5]In general, depending on the light intensity on the sample, the number of photons involved in the excitation of one electron is not restricted so that the whole of these processes can be referred to as multi-photon processes.

[6]This problem can be easily transferred to a $one - colour$ experiment.

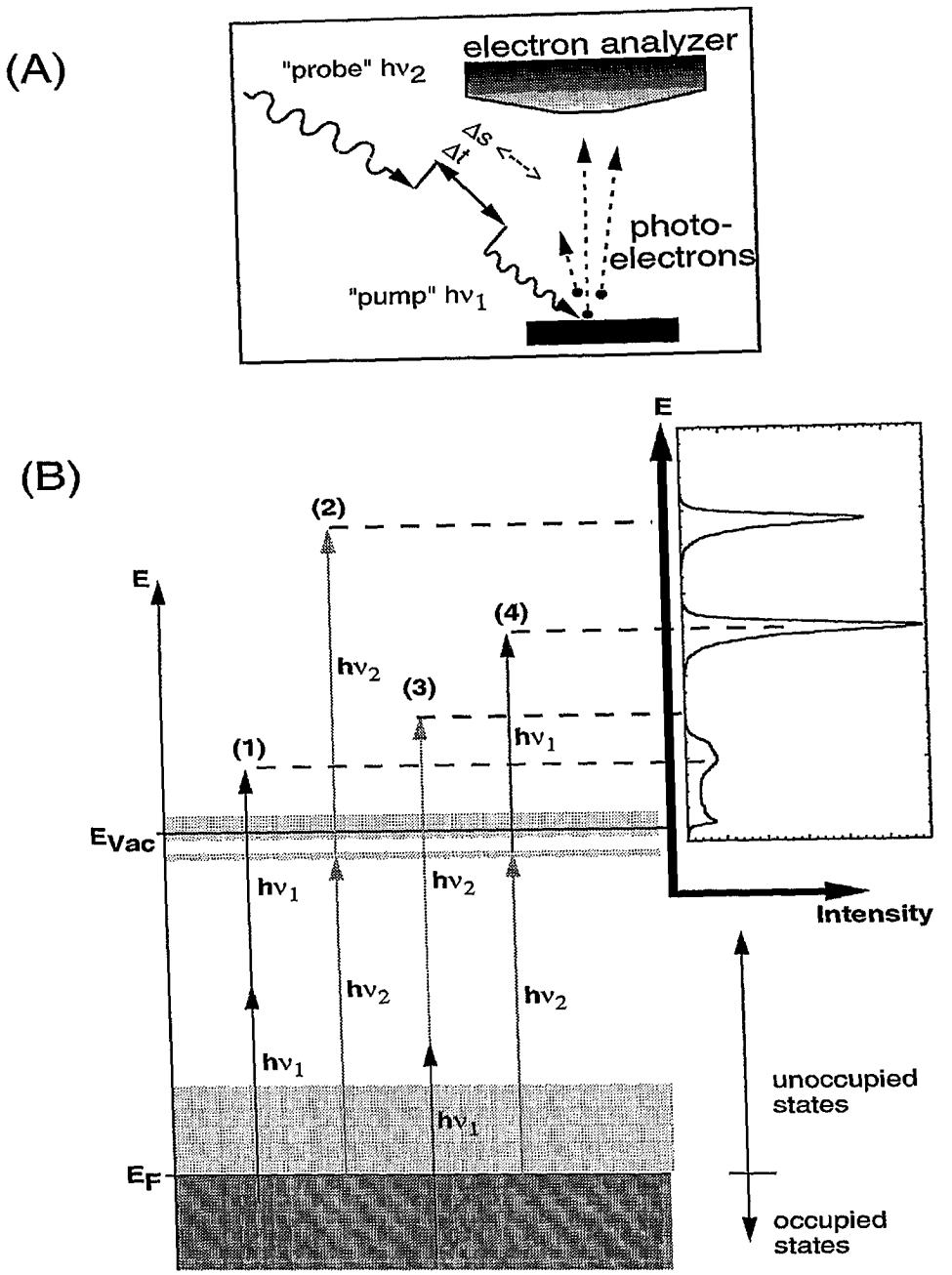

Figure 2.3: (A) The realisation of TR2PPE experiments requires precice control of the time delay between pump and probe pulse at the sample. By taking photoelectron spectra at different time delays, time resolution can be achieved. The population decay of excited electrons can therefore be investigated in the time domain. (B) Possible transitions in a *two – colour* 2PPE experiment. Occupied and unoccupied electronic states are marked by shaded areas. An example for a resulting EDC is shown in the upper right part of the figure. Only the processes (3) and (4) can be used to investigate the dynamics of excited electrons in the time domain.

Process (2) A first photon with energy $h\nu_2$ excites the electron into a previously unoccupied state while a second photon with the same photon energy photoemits the electron. The difference between the processes (1) and (2) is the resonant nature of process (2) since an intermediate electronic state is involved.

Process (3) A photon of pulse 1 (pump pulse) with energy $h\nu_1$ excites the electron into a normally unoccupied state, whereas a second photon of pulse 2 (probe pulse) with energy $h\nu_2$ lifts the electron into the vacuum. Similar to process (1), this case is an example for a nonresonant transition.

Process (4) The reverse of process 3 with the difference that this process possesses an intermediate state, thus it is concerned to be a resonant transition. A photon with energy $h\nu_2$ populates unoccupied states, the second pulse containing photons with energy $h\nu_1$ probes those states.

The first two processes can be distinguished form the processes (3) and (4) by blocking one of the two beams. Moreover, the first two processes are independent of the time delay between pump and probe pulse. Thus, peaks resulting from the processes (3) and (4) change significantly in intensity if the delay between the pulses is scanned. However, care has to be taken concerning the classification of peaks originating from the processes (3) and (4). Such a peak must not consequently belong to an excited state. For example, photoemission from an occupied state in a non-resonant two-photon process via a virtual state might be responsible for an observed peak.

It should be noted that, by using different photon energies in the pump and probe pulses, the processes 3 and 4 usually probe dynamics of different states as can be seen in figure 2.3. The choice of the photon energy depends on the energy position of the intermediate states which should be investigated. The processes 1 and 2, if not desired, can be reduced by decreasing the light intensity of each pulse. However, this may reduce the time dependent pump-probe signal as well. Usually the pulse with the smaller photon energy is kept more intense. Its photon energy, if possible, can be chosen such that a three photon process is necessary to overcome the work function and reduce 2PPE within this pulse.

Some experiments require photon energies close to the work function. In such a case the laser pulse can excite electrons from the high energy side of the Fermi tail right above the vacuum level via the absorption of only one photon leading to a large number of photoemitted electrons per pulse due to the high light intensity. Since the electrons are only photoemitted[7] within the laser pulse duration, the emitted electrons can affect each other as long as they are close to the surface. The electrons next to the surface are retarded, whereas the electrons which are far away are accelerated. This leads to a broadening of the resulting EDC, the structures and

[7]The photoemission event takes place on a time scale in the 10^{-18}s regime. Therefore it can be treated as an instantanous process on a femtosecond timescale.

peaks in the EDC may be broadened or smeared out, in other cases new artificial structures can occur. This phenomenon is called "space charge effects" and should be avoided. To avoid space charge effects care must be taken in the choice of the used photon energy and the intensity of the laser pulses. Space charge effects can also occur in two- or three-photon absorption if the intensity at the sample surface is too large. However, R. Haight has shown that time resolved 2PPE (TR2PPE) is possible on a large number of semiconductor surfaces with probe photon energies around 10 eV by choosing low light fluences and pikosecond pulses.

2PPE experiments provide an energy resolution between 20 and 100 meV, depending on the used spectrometer. In inverse photoemission experiments, a lower limit of about 250 meV is reported. Thus, due to the improved energy resolution, 2PPE is also superior for the investigation of the electronic structure above E_F. However, the major aspect of TR2PPE compared with IPE is the feasibility of measuring dynamics and lifetimes of excited electrons directly in the time domain. Together with the energy resolution in photoemission experiments direct access to the population of every individual excited state is possible.

This can be accomplished by recording photoemission spectra at different time delays between pump and probe pulse. Each photoelectron spectrum at various delay can then be seen as a "snapshot" of the momentanous occupation of the electronic states. Time dependent structures should than decrease in the EDC for increasing time delay after the pump pulse has passed by. The population decay of normally unoccupied states after the excitation with a short laser pulse can therefore qualitatively and quantitatively be detected in a direct measurement.

Chapter 3

Image-potential states: a special class of surface states

The subject of this thesis is the investigation of electron dynamics in a special class of surface states, the so called "image-potential states". These occur if an electron placed in front of a metal surface is attracted by its own image charge leading to a series of unoccupied bound states converging towards the vacuum level. Due to their reduced overlap with bulk wave functions, electrons populating image-potential states exhibit significantly longer lifetimes compared to other electronic states in metals thus providing useful systems to study the interaction of excited surface electrons with the underlying substrate. This chapter gives a general introduction into the properties of electronic states localized at surfaces with a focus on image-potential states. It starts with a description of novel electronic states occuring at the surface. In a second step elementary multiple-reflection theory is discussed as an elegant way of looking at surface states, especially image-potential states. Finally, their binding energies, effective masses and lifetimes are briefly discussed.

3.1 Crystal-induced surface states

The three-dimensional periodicity of the crystal lattice is reduced to two dimensions at the surface. The broken symmetry gives rise to modifications of the electronic and geometrical structure due to redistributions of the electronic surface charge density. Electronic wave functions must no longer be periodic in the direction perpendicular to the surface plane. This leads to novel electronic states at the surface which can be distinguished from electronic bulk states arising from the three-dimensional periodicity of the crystal lattice [40, 41]. Wavefunctions of those states decay rapidly into the crystal. In addition, as do all bulk states below E_{Vac}, the wavefunction is also strongly damped in the vacuum. Thus, these two dimensional states are spatially confined at the surface. If their wave function is confined to the outermost atomic layers, they are somewhat artificially called crystal-induced "surface states"

or "surface resonances" [42]. They can thus be separated from image-potential states discussed in the next section. "True" crystal-induced surface states are located inside a gap of the projected bulk-band structure whereas crystal-induced surface resonances decay slower into the crystal and may be degenerate with bulk bands.

How can we distinguish surface states (or resonances) from crystal bulk states in photoemission experiments?

There are three criteria which can be applied [43]. First of all surface states are, as mentioned above, two dimensional systems. Therefore only the quantum numbers for energy and momentum parallel to the surface plane are of interest since $k_\perp$ is no longer a good quantum number. Hence, perpendicular to the surface an $E(\vec{k})$ dependence could not be observed since the state can not disperse in that direction. The latter could easily be checked by varying the photon energy and detecting the photoelectrons in normal emission.

A second criterion is the sensitivity of surface states to contamination. One can expect that changes at the surface due to adsorbates may also influence the electronic structure specially of the first few layers since surface state are mostly located at the topmost layer. Therefore a number of experiments have been performed in order to investigate how the electronic structure has changed after exposure of the sample to only one sort of atoms or molecules. Surfaces of reactive materials rapidly contaminate even under UHV conditions through adsorption from the residual gas. Hence, surface states are expected to be strongly attenuated with time. However, one should be careful to take this criterion into account alone, because it must not be valid in all cases.

The last criterion concerns the location of surface states in $\vec{k}$ space. Surface states can only exist in regions of the Brillouin zone where a hybridisation with bulk states is impossible. The symmetry of bulk bands must be in such a manner, that at given energy E and wave vector $\vec{k}_{||}$ a coupling between the surface state and bulk states can not occur. A projection of the bulk band structure to the surface plane results in regions of allowed bulk states. The gaps in this projected bandstructure are regions in $\vec{k}$ space where surface states can occur.

It has become customary [42] to distinguish between *Shockley* and *Tamm* states depending on their origin and concentration near the surface. *Shockley* states are created in a gap of the sp-bulk band structure due to the termination of the crystal by the surface. Their wavefunctions may extend more than one atomic layer into the crystal.

Tamm states are d- or f-like surface states in transition metals. In contrast to *Shockley* states *Tamm* states are more localized in real space. They are split-off from a band (e.g. a d-band) of the crystal due to the deviation of the periodic potential at the surface.

3.2 Image-potential states at surfaces

Image-potential states discussed in the following have a somewhat different origin from the crystal-induced surface states described above. These surface states arise, when electrons in front of a metal surface are trapped by their own positive image charge inside the metal.

Image-potential states where first predicted by Cole and Cohen [44]. Using a multiple-reflection approach, Echenique and Pendry considered these states as electrons trapped between the bulk crystal via a band gap and the attractive surface barrier which prevents them from escaping into the vacuum [45]. The gap in the projected bulk-band structure prevents the electron from escaping into the crystal. Within their model an electron with corresponding wave function Ψ_+ travels towards the crystal[1] and is reflected at the crystal surface due to the lack of bulk states. The reflected wave function can be expressed by

$$\Psi_- = r_c \exp(i\Phi_c)\Psi_+ \tag{3.1}$$

where Ψ_- travells from the crystal towards the surface barrier. Reflection of Ψ_- at the surface barrier towards the crystal leads to [45]

$$\Psi_+ = r_b \exp(i\Phi_b)\Psi_- = r_b \exp(i\Phi_b) r_c \exp(i\Phi_c)\Psi_+ \tag{3.2}$$

where r_c and r_b are the reflection coefficients and Φ_c and Φ_b are the phase changes occuring upon reflection at the crystal and the vacuum barrier, respectively. Summing over an infinite number of reflections yields the total scattering amplitude [45]:

$$[1 - r_c r_b \exp(i(\Phi_b + \Phi_c))]^{-1}. \tag{3.3}$$

In such a scattering formalism bound surface states are characterized by poles in the amplitude [45]. A pole requires that the denominator in equation 3.3 must be zero. Thus the necessary condition for the excistence of a surface state is given by

$$r_c \cdot r_b = 1 \tag{3.4}$$

and

$$\Phi_c + \Phi_b = 2\pi n \tag{3.5}$$

where n is an integer comparable to a quantum number in a hydrogen atom. Since by definition $r_c \leq 1; r_b \leq 1$, the first condition may also be read as

$$r_c = r_b = 1 \quad . \tag{3.6}$$

Condition 3.6 can only be satisfied for energies below E_{Vac} where the electron can not escape into the vacuum ($r_b = 1$). Another requirement is a bulk-band gap providing high reflectivity at the crystal surface ($r_c = 1$).

[1] For simplicity the authors viewed in a first step only plane waves.

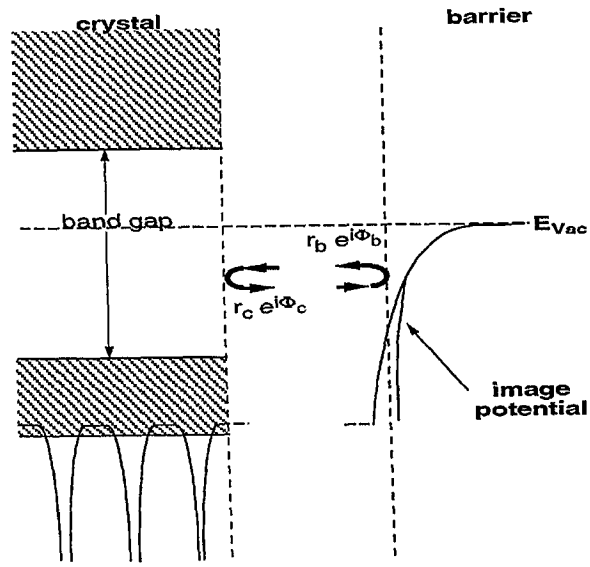

Figure 3.1: Schematic potential in the vicinity of a crystal surface. Dashed areas indicate electronic bulk bands. Due to the lack of allowed electronic states in the gap the wave can not penetrate into the crystal and is therefore reflected. Surface states arise by multiple reflection between the crystal surface and the surface barrier [46].

The phase condition 3.5 determines the energy of the surface states since the phases Φ_c and Φ_b are functions of energy [45, 46]. The variation of either Φ_c or Φ_b with energy is an important element in the creation and classification of surface states. The greater the variation the greater the chance of sweeping through the $2\pi n$ condition.

A rapid variation of the phase Φ_c leads to a crystal induced surface state and that induced by a rapid variation of Φ_b is referred to as a barrier induced state. The formation of surface states also depends on the used potential for the surface barrier. Models using a step-potential barrier or a pure image potential give similar results for the lowest energy state $n = 0$ [46], which is a crystal-induced surface state. However, only the image potential gives barrier-induced surface states for $n = 1, 2, ...$[2] forming a Rydberg series. These $n \geq 1$ states are located in a narrow energy range. Hence, in a first approximation a reasonable assumption is to treat the phase Φ_c as a constant over the whole range of the Rydberg series [46]. These barrier-induced surface states are called "image-potential states".

[2]It should also be mentioned that all surface states emerging from the multiple reflection approach are *Shockley*-type states.

3.3 Binding energies

The exact form of the barrier potential is difficult to estimate. However, an approximation with a Coulomb-like potential

$$V \sim \frac{1}{4z} \tag{3.7}$$

for the barrier gives surprisingly good results [45, 47]. The factor 4 in the denominator of this image potential arises because the electron and the image charge are separated by a distance $2z$. Using this potential the phase Φ_b can be written as a simple function of the vacuum energy E_{Vac} and the perpendicular energy E [48, 49]. In order to calculate the energies of surface states ($n \geq 0$) on low-index faces of metals, a phase analysis of Φ_c and Φ_b including a combination of the multiple reflection approach described above and elemtary nearly-free electron theory (2-band model) can be used [46].

The rough approximation of a pure Coulomb-like potential in order to model the barrier potential can also be rationalized by the following consideration[50]. The electric field induced by an electron placed at a distance z away from a metal surface is identical to the one produced by an opposite charge placed at the same distance inside the metal. This situation is shown schematically at the top of Fig. 3.2. The attractive force due to the image charge is then given by a Coulomb potential:

$$V(z) = E_{Vac} - \frac{e^2}{4\pi\epsilon_0}\frac{1}{4z} \quad . \tag{3.8}$$

The situation reflects the hydrogen problem in one dimension. A calculation leads to a series of bound states with energies [50]

$$E(n) = E_{Vac} - \frac{0.85eV}{n^2} \quad ; \quad n = 1, 2, ... \tag{3.9}$$

converging towards the vacuum level. This equation leads to binding energies relative to E_{Vac} of $E(1) = -0.85$, $E(n) = -0.21$ and $E(3) = -0.09$ eV for the first three members of the Rydberg series, respectively, independent of the metal surface and orientation. Fig. 3.2 shows schematically the first two members of the image-potential state series. In addition, the square of their wave functions are displayed. The localization of the wave function maxima in the vacuum reflects their nature as barrier-induced surface states. With increasing quantum number n the wave-function maxima are localized further and further away from the metal surface.

At metal surfaces image-potential states were first detected using the technique of inverse photoemission [51, 52, 53]. Due to the limitations in energy resolution of inverse photoemission experiments, a systematic and accurate investigation of binding energies for higher quantum numbers n is impossible. Thus, a detailed

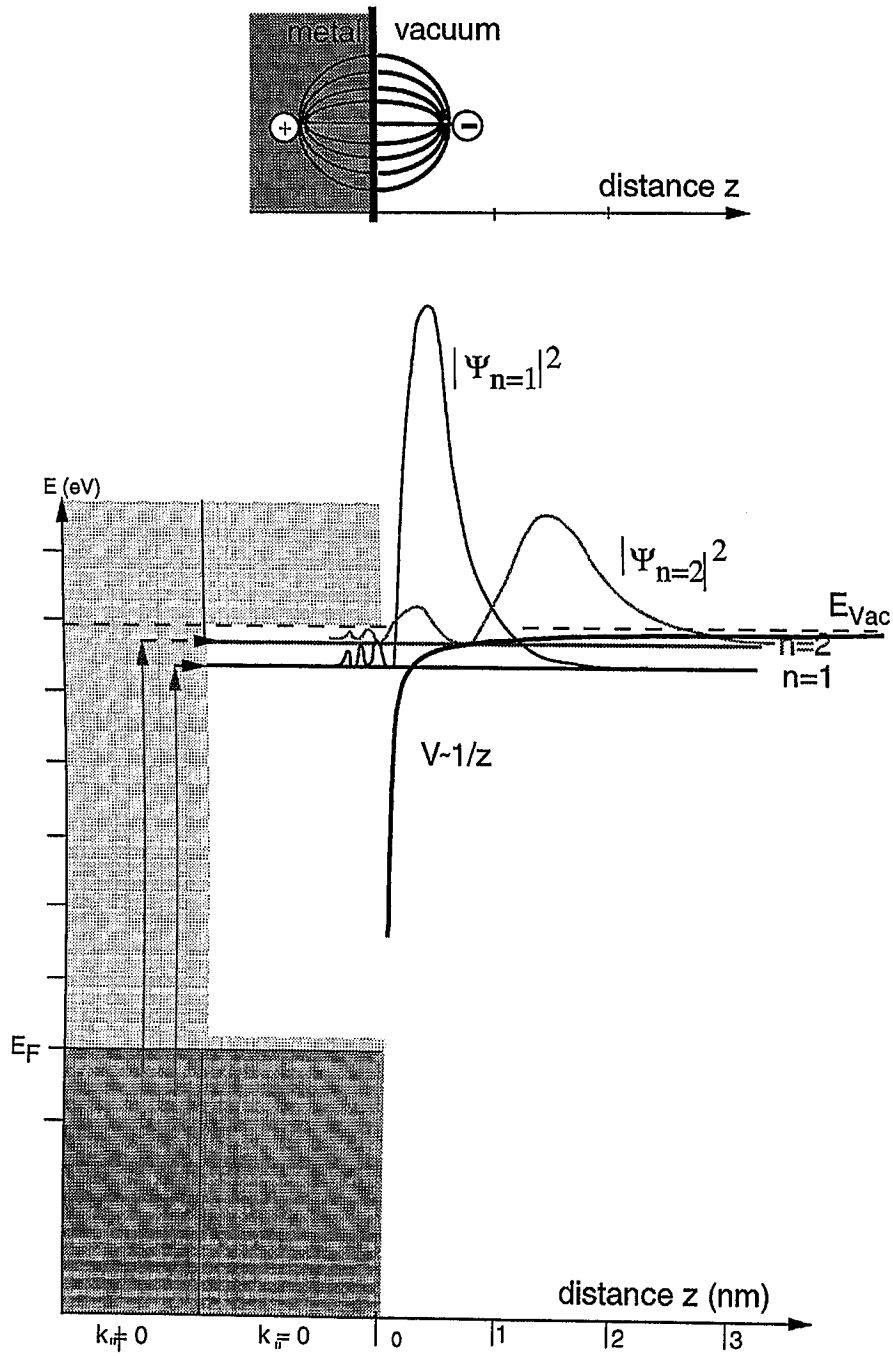

Figure 3.2: An electron near a metal surface induces its own image charge. This gives rise to a series of bound states converging towards the vacuum level. The first two image-potential states and their wavefunctions are shown. Shaded areas display the projected bulk bandstructure.

surface	E(n=1) (eV)	E(n=2) (eV)	ref.
Cu(100)	0.57 ± 0.02	0.18 ± 0.02	[73]
Cu(111)	-0.82 ± 0.05	-0.25 ± 0.07	[56]
	-0.83 ± 0.03	-	[73]
Ag(100)	-0.53 ± 0.02	-0.16 ± 0.02	[55]
Ag(111)	-0.77 ± 0.03	-0.23 ± 0.03	[73]
	-0.78 ± 0.05	-	[57]
Au(111)	-0.80 ± 0.03	-	[58]
Pd(111)	-0.55 ± 0.03	-0.15 ± 0.03	[59]
Ni(100)	-0.61 ± 0.03	-0.18 ± 0.03	[61]
Ni(111)	-0.80 ± 0.03	-0.25 ± 0.05	[62]

Table 3.1: Binding energies with respect to the vacuum level E_{Vac} of the first two members of the Rydberg series for different fcc-metal surfaces.

investigation of image-potential states on different metal surfaces requires experimental methods with improved energy resolution. The development of high-power laser systems offered the opportunity of measuring normally unoccupied states in a photoemission setup [54]. Image-potential states up to the $n = 4$ state have been identified using 2PPE with an energy resolution better than 50 meV [54, 55].

Binding energies for a number of surfaces are listed in table 3.1. It can clearly be seen that binding energies at different metal surfaces for the $n = 1$ state range between -0.53 and -0.83 eV, while the $n = 2$ state exhibits values between -0.15 and -0.26 eV. These results deviate significantly from the values of -0.85 and -0.21 eV for the first two members of the image-potential series, respectively, obtained from equation 3.9, which predicts binding energies independent of the metal surface. At first sight it seems that the binding energies depend on the crystal orientation and a first assumption leads to the distinction between (100) and (111) surfaces. Only the Pd(111) surface deviates from this first classification.

A more physical explanation can be given by taking into account the bandstructure and the energetic position of image-potential states within the band gap. Since image-potential states are pinned to the vacuum level, the position of E_{Vac} with respect to the upper band-gap edge determines the localization of image-potential states inside the band gap. Since the phase change Φ_c upon reflection at the crystal surface of electrons in image states varies across the band gap, the binding energy with respect to E_{Vac} will also change. This leads to a modification of equation 3.9 to [46, 48]

$$E(n) = E_{Vac} - \frac{0.85eV}{(n+a)^2} \quad ; \quad n = 1, 2, 3, ... \tag{3.10}$$

where the quantum defect a depends on the phase Φ_c as

$$a = \frac{1}{2}(1 - \frac{\Phi_c}{\pi}) \quad . \tag{3.11}$$

The quantum defect varies in the range between $0 \geq a \geq 0.5$ across the gap. At the bottom of the band gap a would have a value of $a = 0.5$. It changes to zero as the top of the band gap is approached. The image-potential states on (111) surfaces of the noble metals such as Cu, Ag and Au lie close to the top of the band gap ($n = 1$ state) or are even degenerate with bulk bands ($n \geq 2$ states) leading to a quantum defect a close to zero. On the other hand on the (100) noble metal surfaces (Cu, Ag) and on Pd(111) image-potential states lie close to the middle of the gap and $a \approx 0.25$. Thus with the introduction of the quantum defect a, the binding energies of image-potential states on different surfaces can be explained.

3.4 Effective masses

Image-potential states show, as do all surface states, no $E(k_\perp)$ dispersion perpendicular to the surface. Since electrons in image states are localized in the vacuum region in front of the surface, they represent a quasi free-electron like two dimensional system. Therefore one would expect that the effective mass m^*

$$m^* = \hbar^2 \cdot (\frac{d^2E}{dk_\parallel^2})^{-1} \tag{3.12}$$

is close to the reciprocal of the free electron mass m, that means $\frac{m^*}{m} \simeq 1$. This is indeed observed for a large number of surfaces with the exception of Ag(111), where angle resolved 2PPE studies yield a value of $\frac{m^*}{m} = 1.3 \pm 0.15$ [47, 63]. A ratio $\frac{m^*}{m}$ different from unity results when the phase Φ_c and consequently $E(n)$ depends on $k_\parallel$ [63]. Moving away from $k_\parallel = 0$ the projected band gaps decrease with increasing $k_\parallel$. The lower band-gap edge disperses upwards in energy more rapidly than in the case of free-electrons. The upper gap edge, however, is relatively flat. These characteristics are imposed on the dispersion relation of surface states at the lower and upper band-gap edges. Hence surface states localized close to the upper (lower) band gap edge show a weaker (stronger) dispersion leading to a value $\frac{m^*}{m} > 1$ ($\frac{m^*}{m} < 1$).

3.5 Lifetimes

The decay of image-potential state populations is mostly governed by the creation of electron-hole pairs [45, 64]. In a simple picture the overlap of the wave function with bulk states is responsible for the relaxation dynamics of electrons in image states.

surface	$\Gamma_{n=1}$ (meV)	$\Gamma_{n=2}$ (meV)	reference
Cu(100)	28 ± 6	-	[23]
Cu(111)	16 ± 4	-	[61]
	85 ± 10	-	[19]
	62 ± 5	-	[65]
Ag(100)	21 ± 4	5 ± 5	[23, 61]
Ag(111)	44 ± 9	$< \Gamma_{n=1}$	[66]
Pd(111)	70 ± 20	$< \Gamma_{n=1}$	[59]
	32 ± 4	-	[60]
Ni(100)	70 ± 8	$< \Gamma_{n=1}$	[61]
Ni(111)	84 ± 10	12 ± 10	[61]
Fe(110)	130*	25*	[67]
Co(0001)	95*	18*	[67]

Table 3.2: Linewidths for image-potential states on different surfaces measured with 2PPE. The lifetime can be deduced by $\tau(fs) \approx \frac{0.66}{\Gamma(eV)}$. *: no value for the error given.

Their lifetimes τ within a Rydberg series are theoretically predicted to increase with quantum number n as [45]

$$\tau \propto n^3 \quad . \tag{3.13}$$

With increasing n image states are localized further and further away from the metal surface leading to a decreasing wave-function overlap with adjacent bulk states. Hence the overlap with bulk bands decreases with increasing quantum number n and conesquently lifetimes for higher Rydberg members should increase according to the n^3-power law. However, one can expect that this general law is not valid for all surfaces since the interaction of image-potential states with bulk states or crystal-induced surface states may change from surface to surface. As mentioned above, 2PPE measurements yield considerable variations of image-potential state binding energies on different surfaces. To obtain a deeper understanding of these model systems, lifetime investigations of image-potential states are therefore of great fundamental interest.

The intrinsic linewidth Γ of an electronic states is inversely proportional to its lifetime τ (see equation 2.14). Thus, by measuring the linewidth one has access to the lifetime τ of the corresponding state. However, one has to take into account that the surface roughness and defects may increase the linewidth. Electronic states with lifetimes of some ten femtoseconds possess linewidths below 100 meV. In order to accomplish accurate linewidths measurements, spectroscopic techniques with sufficient energy resolution are required. Using high resolution 2PPE, the linewidths of image-potential states have been measured on a number of metal surfaces. The results are listed in table 3.2.

surface	$\tau_{n=1}$ (fs)	$\tau_{n=2}$ (fs)	$\tau_{n=3}$ (fs)	reference
Cu(100)	40 ± 6	120 ± 15	300 ± 20	[23]
Ag(100)	25 ± 10	180 ± 20	-	[7, 25]
	55 ± 5	160 ± 10	360 ± 15	[23]

Table 3.3: Lifetimes of the first three members of the Rydberg series on the (100) faces of Cu and Ag, measured with TR2PPE. The observed lifetime values increase with quantum number n, thus following the trend predicted by the n^3 power law.

The linewidths given in table 3.2 for a number of $n = 2$ image states are significantly reduced compared to the $n = 1$ states. This indicates a longer lifetime according to equation 3.13. For the $n = 2$ states a correct linewidth determination becomes problematic due to the large relative error. This demonstrates that despite of the improved energy resolution in 2PPE compared with inverse-photoemission spectroscopy, accurate linewidth measurements for $n \geq 2$ states will fail. The first problem arises from the energetic position of higher Rydberg members close to the vacuum level E_{Vac}. In order to populate these states, the photon energy has to be tuned close to the work function so that a peak broadening due to space charge effects may occur. Another problem arises from the reduced energy spacing for states with $n > 3$ according to equation 3.10. Even with an improved energy resolution, these states cannot be resolved.

The limitation for states with $n \leq 3$ can be overcome by real-time investigations of the electronic population in time-resolved pump-probe 2PPE experiments. Moreover, in time resolved 2PPE (TR2PPE) experiments a direct comparison of the lifetime, measured in the time domain, and the linewidth, obtained from the energy distribution curve within the same experiment, is possible.

In recent TR2PPE experiments on noble-metal surfaces of Cu and Ag lifetimes of image states up to the $n = 3$ state were obtained. The results are shown in table 3.3. A significant lifetime increase with quantum number n is indeed observed confirming the trend predicted in equation 3.13.

A comparison between lifetime values obtained from TR2PPE with those obtained from linewidth measurements shows relatively large deviations even for the $n = 1$ state. This observation can be explained by the dephasing of the image-potential population after the coherent excitation. The lifetime τ describes the population decay due to inelastic scattering processes and is measured directly in the time domain with TR2PPE. Additional elastic scattering events leave the electrons in the excited states but destroy their phase coherence. This introduces the pure dephasing time T^* [39] of the initial and intermediate states, which increases the linewidth Γ to

$$\Gamma = \hbar \cdot (\frac{1}{\tau} + \frac{2}{T^*}). \tag{3.14}$$

The observation of quantum beats in TR2PPE on Cu(100) [24, 20] directly shows the loss of coherence due to the influence of pure dephasing. If the laser bandwidth of the excitation pulse is comparable to the energy spacing of the image-potential levels, the optical excitation creates a coherent superposition of several states forming a wavepacket.

Fig. 3.3 shows quantum beats occuring after the coherent excitation of image-potential states on Cu(100) with quantum numbers $n = 4, 5$, and 6. The curve corresponds to the measured 2PPE signal as a function of pump-probe delay. Image-potential states are populated via optical excitation from bulk bands near the Fermi level. Since the image-potential states are delocalized some ten $\AA$ away from the surface, the initial wavepacket is localized in the region of largest wavefunction overlap with the initial states. Hence this leads to an increased probability of finding the excited electron close to the surface immediately after excitation. After the wavepacket has been created, it periodically moves away from the surface and travells back. Far away from the surface, the electron is nearly free and therefore it cannot absorb a photon from the probe pulse. This leads to dips in the time-dependent pump-probe signal. Only close to the surface the crystal lattice is able to provide momentum for photon absorption. Thus the probe pulse measures the recurrences of the wavepacket at the surface.

The loss of coherence can be increased by adsorption of molecules or atoms which then reduce the number of quantum beats due to rapid dephasing. The observation of quantum beats provides further information about binding energies and lifetimes for higher image-potential states with $n \geq 4$. Up to now, the spacing between image-potential levels for states $n \geq 4$ has not been resolved in the energy domain, since an energy resolution beyond 10 meV is difficult to achieve experimentally.

Höfer et al. deduced the binding energy difference between $n = 4$ and 5 from the Fourier transform of the data shown in Fig. 3.3 to $\Delta E_{4,5} = 17.8$ meV and that for $n = 5$ and 6 to $\Delta E_{5,6} = 9.6$ meV. Furthermore, quantum beat spectroscopy on Cu(100) also provides information on the lifetimes of the states with quantum numbers $n = 4, 5$ and 6 with value of 0.63 ps, 1.2 ps and 2 ps, respectively. This is in reasonable agreement with the n^3 power law.

3.6 Influence of adsorbates

So far we have focused on the description of physical properties of image-potential states on bare metal surfaces. We now extend the discussion to adsorbate induced changes in binding energies and lifetimes. A modification of the surface due to adsorbates affects the surface geometry and electronic structure. It, therefore, may have a large impact on the formation of image-potential states and their interaction with the bulk electronic structure. The adsorption of atoms or molecules usually leads to a change in the work function of the sample. Since image-potential states are pinned to the vacuum level (see equation 3.10), a work function change will also

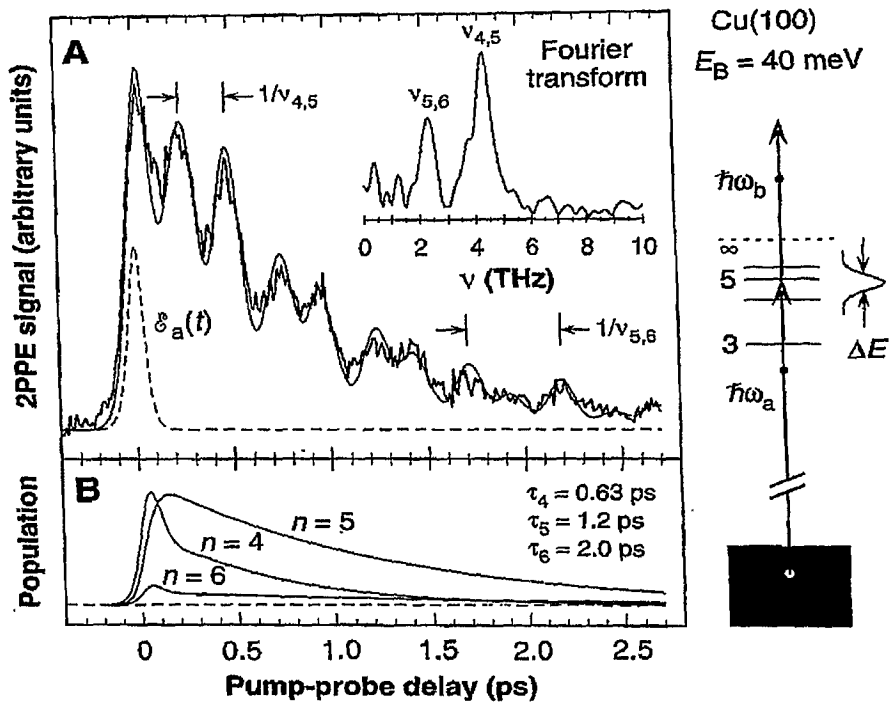

Figure 3.3: (A) Temporal response of the coherent excitation of image-potential states with quantum numbers 4, 5 and 6. The formation of a wave packet which travels away from and back towards the surface results in the observed dipsin the response. (B) Relative population of the individual image-potential states. Taken from reference [24].

influence their energy positions relative to E_F. In other words, the adsorbtion of atoms or molecules changes the energetic position of the Rydberg series relativ to the band gap and will therefore affect their lifetime as well. Several experiments have been performed to investigate the lifetime dynamics on adsorbate covered Cu(111) and Ag(111) surfaces[22, 56]. For instance, the adsorption of 1 monolayer Xe on Cu(111) [56] lowers the work function by 0.5 eV. The work function change shifts the image-potential states towards the band gap center which in turn leads to stronger damping of their wavefunctions. In addition the wave-function overlap with bulk states is reduced by the Xe layer. This reduces the binding energy of the $n = 1$ state to $E_{n=1} = 0.68 \pm 0.05$ eV. The lifetimes of the first two Rydberg states are increased to 75 ± 15 and 40 ± 10 fs for the $n = 1$ and $n = 2$ state, respectively, as compared to lifetimes of 18 ± 5 and 17 ± 5 fs[3] obtained for the pure metal surface.

[3]The reason for the relatively short lifetime of the $n = 2$ state will be explained in chapter 5.

Chapter 4

Experimental setup

TR2PPE measurements were performed under ultrahigh-vacuum (UHV) conditions at a base pressure better than $6 \cdot 10^{-10}$ mbar. The UHV apparatus consists of two different UHV chambers for sample preparation and photoemission measurements, respectively, separated through a valve as shown in Fig. 4.1. Using a transfer rod, the sample can be easily moved from chamber to chamber. Photoelectron spectra were recorded using a Ti:sapphire ($Ti : Al_2O_3$) laser system (Coherent) as light source in combination with a commercial hemispherical analyzer (Leybold) or a homebuilt time-of flight spectrometer (TOF) for electron detection. In order to measure the density of occupied states, the measurement chamber is also equipped with a HeI-discharge lamp (21.22 eV photon energy). Samples were prepared in the other chamber equipped with standard preparation and analysis tools. In particular, the preparation chamber contains a sputter gun (ion-bombardment gun) for cleaning the sample, a quadrupole mass spectrometer for the residual gas analysis, a LEED[1] system for characterisation of the samples and several leak valves in order to introduce gases like Ar, O_2, or H_2. In addition, the sample can be heated up to 1000 K while the sample temperature could be controlled using a Ni-Cr/Ni thermocouple.

During this thesis the existing laser system was upgraded from a 200 fs to a 50 fs version. For this purpose, the whole optical setup (pulse compressor, mirrors, focusing elements), containing the optical paths from the laser system to the UHV chamber, was completely new designed. This was necessary since care has to be taken in order to keep the pulse length at the sample as short as possible. Moreover, the setup for a photon energy of 4.5 eV has been realized in the experiment.

The photoelectron detection has been improved, as well. In order to enhance the energy resolution, the above mentioned time-of flight spectrometer, which will be described in section 4.2.2, has been developed and was successfully used in our experiments. The second advantage of the TOF compared with the previously used hemispherical analyzer lies in the reduction of the measuring time per photoelectron spectrum. In addition, the use of the TOF makes possible the simultaneous mea-

[1]Low energy electron diffraction

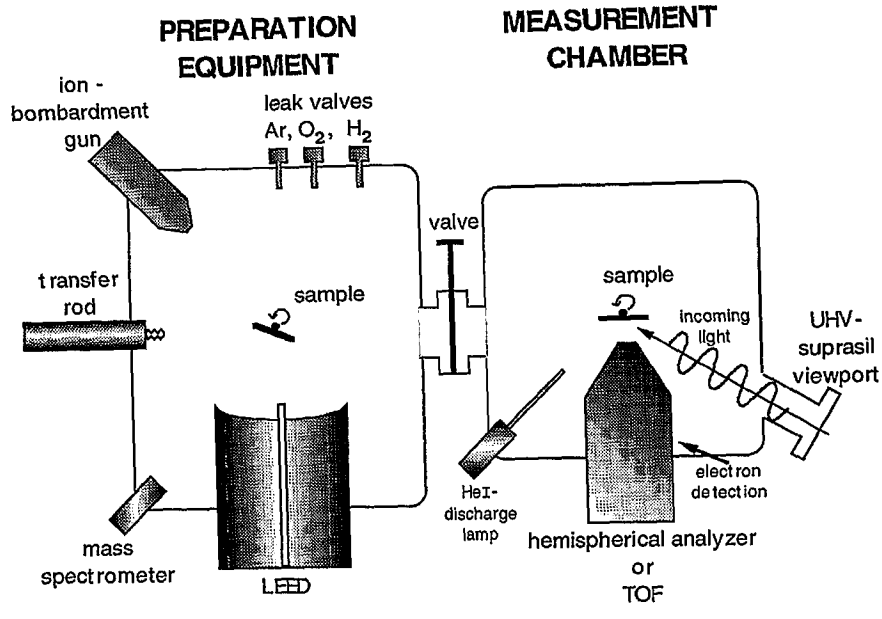

Figure 4.1: The UHV system consists of two parts separated through a valve. The left part is used for sample preparation and characterization, while photoemission experiments are performed in the right "clean" chamber.

surement of the instrumental cross-correlation and the temporal responses of several electronic states.

This chapter is divided into three parts: the first part describes the laser system and the optical setup, the second illustrates the electron detection while the last part describes the sample preparation and surface cleaning procedures in detail.

4.1 Laser system and optical setup

4.1.1 Generation of fs-laser pulses

We start the description of the femtosecond-laser system with a short introduction into laser technology. Three important components for the optical resonator of all lasers are a mirror with 100 % reflectivty, a laser medium and an output coupler with a reflectivity <100 %. Light amplification is only possible if the gain of the laser medium exceeds the loss inside the resonator. In general this condition is only fulfilled for a small wavelength range depending on the used laser medium. In addition, the light path L inside the resonator determines the number of modes with wavelengths λ which could be amplified:

$$L = m \cdot \frac{\lambda}{2} \quad ; \quad m = 1, 2, 3, \ldots \quad . \tag{4.1}$$

where m is an integer. Wavelengths which satisfy condition 4.1 are referred to as longitudinal modes.

We now turn to the general requirements for the formation of ultrashort laser pulses. According to Heisenberg's uncertainty principle, pulse length and bandwidth of the laser pulse are intimately connected. This means, that the pulse length is proportional to the reciprocal bandwidth. Using the relation $\lambda = c/\nu$, the difference in frequency of two adjacent modes according to equation 4.1 can be written as

$$\Delta\nu = \frac{c}{2L} \quad . \tag{4.2}$$

A fs-pulse shorter than 100 fs, which propagates through an optical resonator with $L = 1.5$ m length, contains around 10^4 modes. Thus the laser medium should be able to amplify light over a wide- and quasi continuous energy range. Using Ti:sapphire ($Ti : Al_2O_3$) as laser medium, this condition is fulfilled since Ti:sapphire is able to amplify light anywhere from 680 nm - 1100 nm. The coupling of up to 10 adjacent modes is depicted in Fig. 4.2a) taken from reference [68]. If several modes are lasing simultaneously, they add to each other on a random basis depending on their relative timing or phase. Therefore, intensity and length of the laser pulses are randomly distributed. Nevertheless, a noticable amount in intensity and a reduction of the pulse length could be observed. In order to obtain a stable and well defined train of fs pulses, the phase between each mode should be adjusted non-randomly and held constant as shown at the right part in Fig. 4.2a). In this case the peak intensity becomes much larger and the random distribution between the main peaks diminishes. It is schematically shown that the larger the number of locked modes, the higher the peak intensities and the shorter the laser pulses.

In order to realize these conditions, thousands of modes have to be locked together. In addition, all longitudinal modes must operate simultaneously. In general the laser will operate with minor power fluctuations in a cw[2] mode with only one or two simultaneously operating longitudinal modes. In order to enhance the number of modes, a starting mechanism inside the cavity[3] rapidly changes the optical length inside the cavity. This change in the cavity length terminates the previously oscillating modes, leaving atoms in the laser medium available for new modes so that there will be a period during which all these modes can be lasing simultaneously and power fluctuations can start.

Once power fluctuations start, pulses with more or less intensity are formed. Let us first consider an intense laser pulse with a gaussian beam profile perpendicular to the direction of propagation. This means that the beam intensity decreases from the center of the beam with a factor of $exp(-\alpha r^2)$, where r denotes the distance from the beam center and α is a constant. If the beam travels through matter and its light is intense enough, its electric field can distort the atoms of the material

[2]continuous wave

[3]The region of space between the output coupler and the high reflector is referred to as the laser cavity.

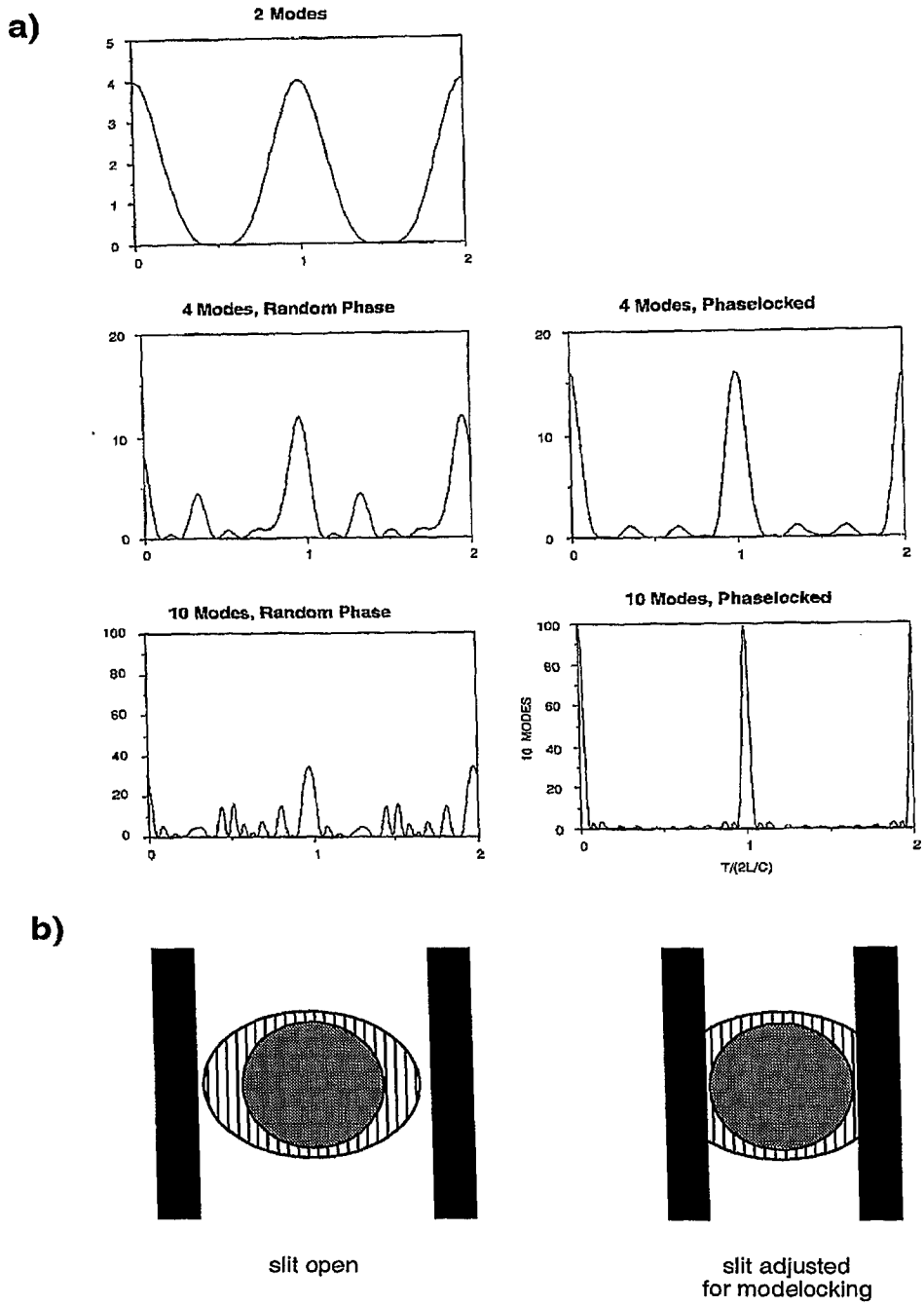

Figure 4.2: a) Superposition of up to ten modes with a random (left part) and a locked (right part) phase distribution. If the phases are non-randomely adjusted and held constant, the peak power becomes much larger and the random spiking diminishes. b) If the slit is open (left side), both the focused, randomely created pulse and the continuous laser beam can pass through without any loss. After adjusting the slit for modelocking operation, only the narrowed intense pulse passes unattenuated.

and alter the refractive index n^*. The change in n^* is larger at the beam center and decreases with increasing distance r, thus a gradient index lense is formed. Changes in the refractive index due to the beam intensity alter the beam diameter inside the cavity and the beam is narrowed. This effect of self focusing is referred to as optical Kerr effect.

Consider now a randomly created pulse caused through power fluctuations oscillating in the cavity. This pulse travels through the Ti:sapphire crystal which acts as Kerr lens and narrows the pulse (shaded area at the left part of Fig. 4.2b)). Less intense power fluctuations are not able to modify the Ti:spphire crystal so that they remain as an unnarrowed low-power background as shown in the left part of Fig. 4.2b) (dashed area). A slit aligned in the cavity at the focal point permits only the focused high intense pulse to pass, while the unfocused cw background is interrupted at its edges and attenuated (right part of Fig. 4.2b)). This is the start of passive modelocking. Since the Kerr lens is only formed upon the arrival of the intense pulse, only narrowed modelocked pulses pass unattenuated through the slit.

It can be shown that once a fs-pulse is formed, the pulse lengthens after it has passed through optical elements. For instance, a 10 fs-laser pulse with a center wavelength of 795 nm is broadened to 100 fs after traversing a 1 cm thick fused silica plate [69]. It is well known from fundamental optics that the refractive index n^*, which determines the phase velocity of each material, depends on the wavelength λ. The first derivative $\frac{dn^*(\lambda)}{d\lambda}$ determines the group velocity and thus defines the velocity of a wavepacket with a central wavelength λ. The second derivative finally determines the group-velocity dispersion which governs the relative phase change of the different frequency components. The material shows positive (negative) group-velocity dispersion (GVD), if the red (blue) spectral components exhibit a larger phase velocity compared to the blue (red) components. In the wavelength regime between 200 nm and 1000 nm almost all materials exhibit a positive GVD, which means that n^* increases with decreasing wavelength. As mentioned above, a fs-laser pulse contains a large number of adjacent longitudinal modes. Since the different frequency components possess different phase velocities, the fs-pulse is reshaped after the propagation through matter. The pulse experiences a modulation which leads to a change in frequency with time (*chirp*).

Another phenomenon affecting the fs-pulse length and structure occures when the pulse traverses the Ti:sapphire crystal. When the pulse propagates through the crystal, the refractive index is changed as a function of the light intensity and a Kerr lens is formed. The caused refractive index change is small at the leading and trailing edges, but large at the center of the laser pulse. Thus some parts of the pulse move faster altering the pulse shape. This effect is referred to as "self phase modulation" (SPM) and is equivalent to another source of positive GVD [33].

Since the pulse oscillates in the cavity, it receives a slight chirp from the dispersive optics (starter, wavelength tuning element, Ti:sapphire crystal) at each roundtrip. In order to keep the oscillating pulse short inside the cavity, the positive GVD has to be compensated. For this purpose an optical element with negative dispersion is

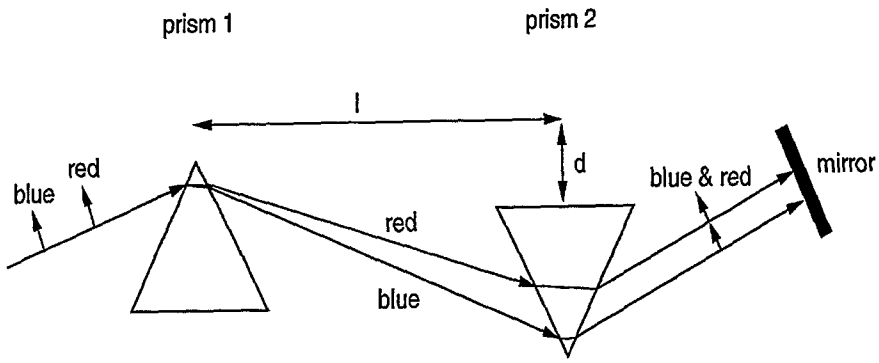

Figure 4.3: Chirp compensation using a pair of prisms.

required, which is able to totally compensate the positive chirp. A pulse compressor inside the cavity could easily be realized using a pair of prisms as shown in Fig. 4.3 [70]. Prisms bend different wavelength into different angles, so that the pair of prisms opens the possibility of forming wavelength dependent paths length for different frequencies.

The magnitude of the GVD compensation could be easily controlled by varying the distance between the two prisms or by shifting prism 2 perpendicular to its baseline. If the distance l between the two prisms is increased, the light path difference between the red and the blue parts also increases. This results in an amount of negative GVD due to the large optical path of the red part in prism 2 (optical path L = geometrical path · refractive index = $\tilde{L} \cdot n^*$). On the other hand, shifting prism 2 towards the beam increases the amount of glass in the optical path thus enhancing positive GVD. Therefore the adjusting parameters l and d allow one to tune the net cavity GVD to zero.

4.1.2 Laser system

The laser system used in our experiments consists of a $Ti : Al_2O_3$ oscillator (Coherent Mira Seed) and a $Ti : Al_2O_3$ regenerative amplifier (Coherent RegA 9000) pumped by an Ar^+ laser (Coherent Innova 400). The oscillator is tunable in a wavelength range between 780 nm and 855 nm with a bandwidth of 35 nm at a repetition rate of 76 MHz. This wavelength interval corresponds to photon energies between 1.59 eV and 1.45 eV. The restriction in the wavelength range results from the optics used (mirrors, tuning element) inside the cavity. It should be noted that the pulse-length specification for the oscillator is based on the bandwiths and not

Ti:sapphire-laser system	
wavelength	780 - 855 nm
intensity	up to 5μJ/pulse
repetition rate	250 kHz
average power	up to 1.25 W
number of photons	$2 \cdot 10^{13}$/pulse
	$5 \cdot 10^{18}$/s
beam diameter	3 mm
beam divergence	3 mrad
pulse length	50 - 60 fs

Table 4.1: Technical data of the fs-Ti:sapphire laser system.

on the pulse length, because the Mira output is highly *chirped*, which means that due to group-velocity dispersion the pulse length is broadened after the propagation through optical elements like output coupler or Ti:sapphire crystal[4]. If needed, the pulse can be compressed again below 50 fs using a second pair of prisms for external GVD compensation.

In order to enhance the energy per laser pulse, the pulses from the oscillator are first stretched to a length of more than 100 ps to guarantee safe operation during amplification and then amplified in a regenerative amplifier (RegA) by a factor of 1000 yielding a pulse intensity of up to 5 μJ at a repetition rate of 250 kHz. After subsequent compression laser pulses of 50-60 fs are available over the whole wavelength range. It is worthwhile to note that the stretcher and compressor stages use gold-coated diffraction gratings (1200 grids per mm) instead of pairs of prisms. However, the principle of compressing or stretching the laser pulses remains the same. The corresponding power of a 50 fs-laser pulse can then be calculated to 100 MW. Table 4.1 displays the technical data of the laser system.

Apart from alkali metals, most materials possess work functions between 4 and 6 eV, thus even in a two-photon process the laser output of around 1.5 eV is insufficient to photoemit one electron. In order to overcome this problem, laser pulses with photon energies of up to 6 eV are required. Higher photon energies can be generated using nonlinear optical processes in crystals. The infrared output can be doubled (second harmonic), tripled (third harmonic) or quadrupled (fourth harmonic). Since the conversion efficiencies especially for higher harmonics are low, high pulse intensities are required to provide sufficient photons per laser pulse even at photon energies around 6 eV.

As mentioned above, higher photon energies are required to perform a TR2PPE

[4]The optics inside the cavity are arranged in the following way: after the pulse has passed through the prism compressor, it has to traverse the Ti:sapphire crystal and a birefrigent filter which selects the wavelength. Finally the emitted part of the pulse traverses the output coupler.

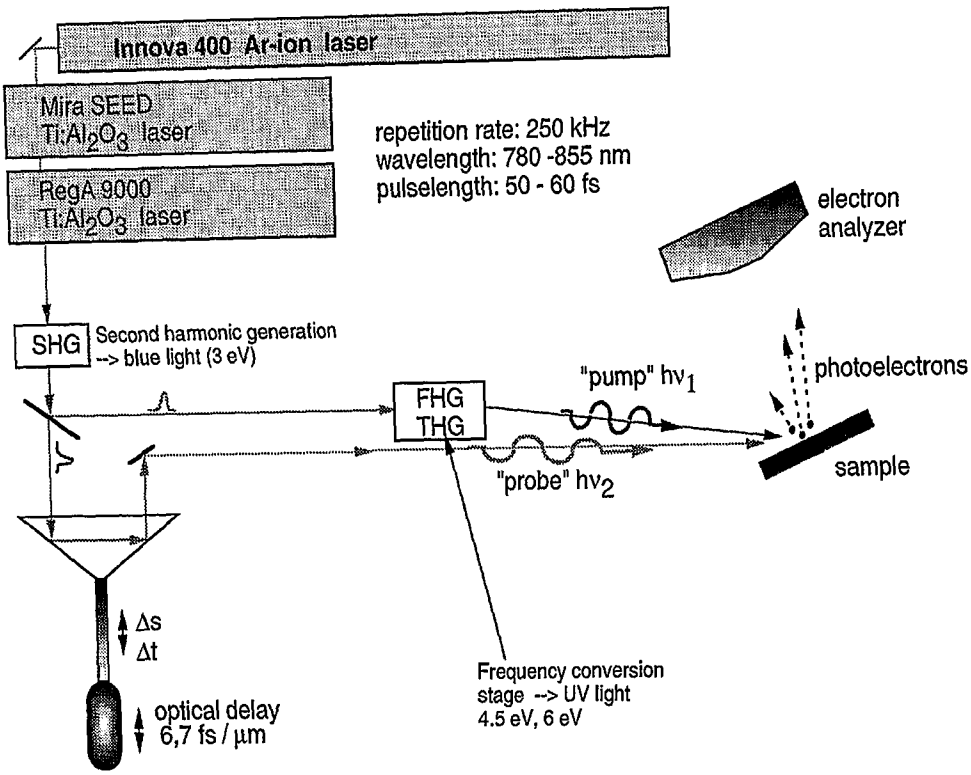

Figure 4.4: The emitted infrared radiation is frequency doubled and split into two parts. The reflected light is again frequency converted ($\Rightarrow$ UV light), while the other part could be delayed in time using a retroreflector. Both beams are focused onto the same spot of the sample, which is mounted in a vacuum chamber.

experiment. It has become favorable to use β-barium borat ($\beta - BBO$) crystals to generate radiation down to a wavelength of 205 nm via nonlinear optical frequency-conversion processes. In a first step the RegA output is therefore frequency doubled using a thin ($< 1mm$) β-BBO crystal. This generates the second harmonic (blue light) with photons of around 3 eV energy. A conversion efficiency of 20 - 30 per cent was obtained using a concave mirror with 30 cm focal length as focusing element. The choice of the second frequency conversion stage depends on the physical system under investigation. Since image-potential states are pinned to the vacuum level with binding energies < 0.85 eV, the photon energy should be high enough to populate those states, but one should keep the photon energy well below the work function to avoid space charge effects. Hence, samples with a work function of 5 eV require photon energies below 5 eV.

The third harmonic with photon energies between 4.35 eV and 4.77 eV is generated by sum-frequency mixing of the fundamental and the second harmonic radiation in a second β-BBO. Since the laser pulses possess durations far below 100 fs, care has to be taken to avoid different arrival times of the 1.5 eV and 3 eV pulses at the

BBO crystal. Therefore only concave mirrors instead of lenses are used to avoid a time delay between pulses of the fundamental and the second harmonic due to their different group velocities in the lenses.

Photons of arround 6 eV are required for samples like Pt(111) (Φ=5.97 eV). For this purpose, the fundamental and the second harmonic could be separated using a dichroic mirror. The second harmonic is then focused into an appropriate $\beta - BBO$ crystal generating the fourth harmonic ($\approx$ 6 eV) via another non-linear process[5]. Unfortunately, the wavelength range of the generated radiation is restricted to wavelength $>$ 205 nm. The conversion efficiencies for the third and fourth harmonic are on the order of 10 % and 1 % [71], respectively.

Pump- and probe pulses for a TR2PPE experiment could be created by using beam splitters or, in order to separate the harmonics, dichroic mirrors. A schematic overview for the whole optical setup is displayed in Figure 4.4[6]. After the first frequency conversion stage, a beam splitter generates two pulses. The reflected part which contains 70 % of the beam intensity is again frequency converted producing UV photons of around 4.5 eV or 6 eV and serves as pump pulse. The transmitted part runs through an computer-controlled optical delay line (retroreflector) and serves as probe pulse. Both pulses are focused onto the sample and are brought into spatial overlap. By physically moving the retroreflector, both pulses can be delayed in time with respect to each other. A retroreflector shift of 1 μm corresponds to a delay of 6.7 fs, so that precise time-resolved measurements are possible.

4.1.3 Measurement of ultrashort laser pulses

A major ingredient in time resolved experiments is the exact knowledge of the pulse durations at the sample. The laser pulse duration has to be measured indirectly since all direct methods fail due to the long relaxation times of common photodetectors[33]. In order to obtain information about the pulse structure, an autocorrelation technique is used. In an autocorrelation setup the beam is split into two parts of approximately equal intensity. One part is sent through a variable optical delay stage before both parts are recombined at the measurement point, for example at a $\beta - BBO$ crystal. The superposed beam has to induce a nonlinear effect, in this case second-harmonic generation or sum-frequency mixing, which is measured using a photodiode. The measured signal depends on the combined light intensity, which is a function of the time delay between both pulses and the temporal pulse width of the laser. Since the beam is split into two parts which are subsequently combined, a correlation of the beam with itself is created, hence the name autocorrelation. The pulse structure of the infrared RegA output is monitored using such an autocorrelator with integrated spectrometer (APE pulsescope) in order to measure pulse duration and bandwidth in situ.

[5]In other words one may say that the second harmonic of the 3 eV radiation is generated, yielding the fourth harmonic.

[6]Detailed setups for a variety of pump- and probe photon energies are given in appendix A.

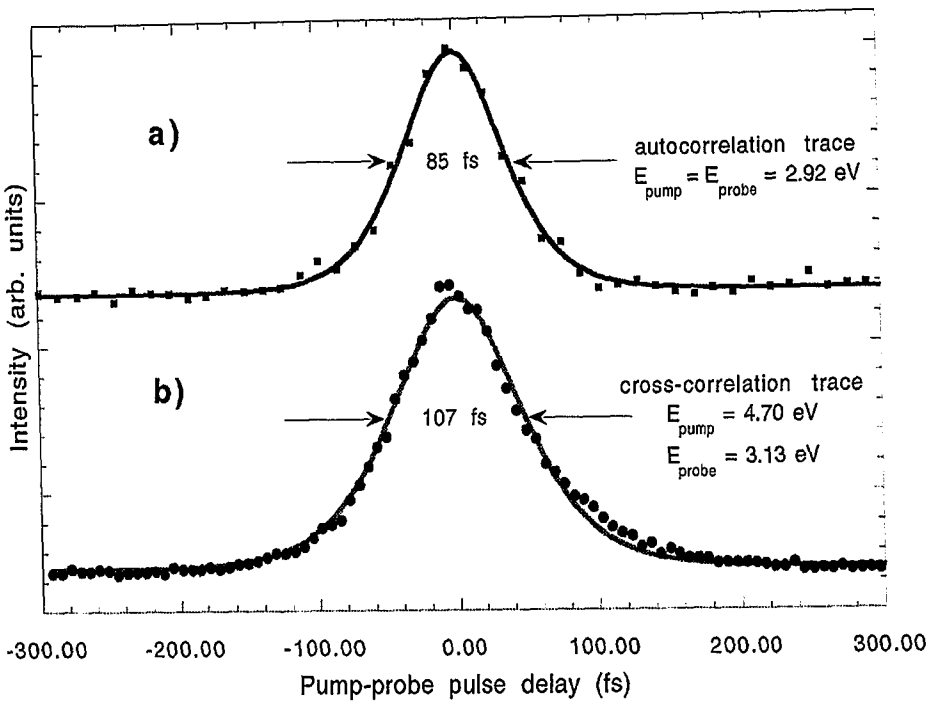

Figure 4.5: a) Autocorrelation curve of a blue laser pulse with a duration of 55 fs. b) Cross-correlation curve in a two-color experiment ($\hbar\omega_{pump} = 4.7$ eV, $\hbar\omega_{probe} = 3.13$ eV). The corresponding fits are based on a $sech^2$ function.

However, the monitored pulselength of the compressed RegA output is not necessarily the same as that used for pump- and probe pulses at the sample. On the way to the sample, the beams pass through $\beta - BBO$ crystals, beam splitters, lenses and the suprasil-vacuum viewport. As described above, these materials possess GVD and therefore broaden the pulse length. In order to keep the pulses at the sample as short as possible, the grating-compression stage behind the RegA amplifier can be used to impart a negative chirp to the pulse. This negative chirp is then compensated by traversing the optical elements on the path to the sample. Some experiments require independent pre-chirps for pump- and probe pulses. For this purpose a pair of SF10 prisms was set into the light pass of the probe beam to vary its pulse length independently.

The determination of the pulse duration of the frequency doubled blue light (≈ 3 eV) at the sample can be done by using the TR2PPE photoemission setup. Since the same photon energy and intensity in pump- and probe pulse is used, this technique is referred to as "electronic autocorrelation". Within this technique, the nonlinearity of the 2PPE process is employed to determine the autocorrelation function of the laser pulse. Due to the intense light, each pulse causes an independent two-photon

photoemission signal which is detected using an electron spectrometer. It can be shown that the photocurrent intensity is enhanced by a factor of 3 [72] if both pulses are in exact temporal overlap. If the delay between pump- and probe pulse is scanned, the pulse length can be extracted from the temporal response of the 2PPE signal. An autocorrelation trace of second-harmonic light pulses with a photon energy of 2.92 eV is shown at the top of Figure 4.5 (filled squares), indeed exhibiting a peak to background ratio close to the expected value of 3:1. The full width at half maximum (FWHM) is deduced to 85 fs by fitting a $sech^2$ function ($sech^2(t) = \frac{1}{exp(-1.76\frac{t}{\tau})+exp(1.76\frac{t}{\tau})}$) (solid line)to the data. The assumption of a $sech^2$ pulse shape yields a better fit result compared to a gaussian function. A deconvolution of the $sech^2$ fit yields a duration of 55 fs for the second-harmonic laser pulse.

If the polarizations or photon energies of pump- and probe pulses are different, the time dependent 2PPE signal is referred to as cross-correlation. All TR2PPE measurements presented within this thesis are performed using different photon energies in the pump and probe beams. In order to populate image-potential states UV photons of $\approx$4.5 eV or $\approx$6 eV were used, while the excited electronic distribution was probed with infrared or blue light. Since the UV-laser pulses could not be measured using the electronic-autocorrelation technique without big efforts in the rearrangement of the whole optical setup, their durations has to be deduced from a cross-correlation. This seems to be a disadvantage, but one should consider that in our case electronic lifetimes are measured in a two colour experiment monitoring changes in the cross-rorrelation curve. The measured instrumental cross-correlation governs time resolution and determines the time zero in the experiment. One should note that lifetimes much shorter compared to the instrumental function can be resolved since small changes in the temporal response of electronic states with respect to the cross-correlation can be measured.

Once the duration of the probe pulse ($\approx$1.5 eV or $\approx$3 eV) is determined from an autocorrelation measurement, the length of the UV-pump pulse can be deduced from the FWHM of the cross-correlation. Figure 4.5b) displays a cross-correlation measurement with photon energies of 4.7 eV and 3.13 eV for the pump- and probe pulses, respectively. Together with the probe-pulse length at the sample of in this case 70 fs, measured in an electronic-autocorrelation setup, the obtained UV-pulse length is equal to the probe-pulse duration.

4.2 Electron detection

Photoelectrons were detected using a hemispherical analyzer (Leybold EA200) or a homebuilt time-of flight spectrometer (TOF). All 2PPE spectra were recorded in the normal-emission direction ($k_{||} = 0$). 2PPE measurements on the Pt(111) surface presented in chapter 5 have been performed using the hemispherical analyzer, while the data presented in chapter 6 were recorded using both techniques (Ni(111)) or the time-of flight technique only (Ni(100)). Both techniques are described in the

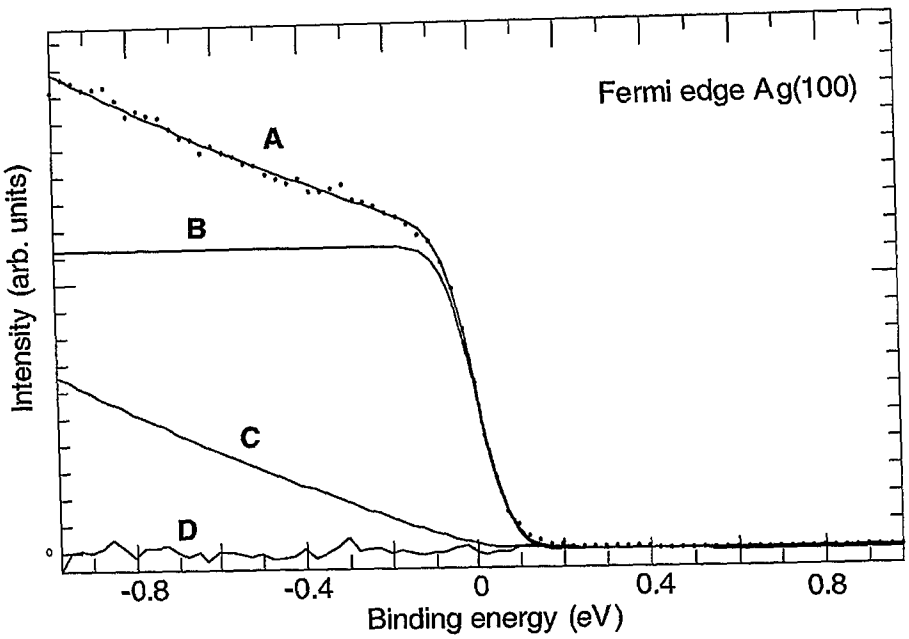

Figure 4.6: The Fermi edge of a Ag(100) single crystal obtained with a photon energy of 6 eV. The pass energy was set to 3 eV. Curve **A** shows the measured curve (filled dots) and a fit (solid line) to the data. The fit consists of the theoretical shape of the Fermi edge (curve **B**) and a background (curve **C**). The difference between fit and data is shown in curve **D**.

following two subsections.

4.2.1 Hemispherical analyzer

The hemispherical analyzer EA200 from Leybold consists of a system of lenses and apertures, a hemispherical capacitor and a multichannel-electron detector with spatial resolution. The system of lenses and apertures defines in a first step the detection area and the acceptance angle of the photoemitted electrons, which originate from a certain spot of the sample. In a second step the electrons are retarded (or accelerated) to the pass energy and focused into a 180° hemispherical capacitor with a nominal radius of 150 mm, which governs the spectroscopic energy resolution. The pass energy is determined by the applied voltages at the outer and inner hemispheres of the capacitor. At a defined retardation voltage only electrons with a kinetic energy corresponding to the pass energy follow the central trajectory of the capacitor and can therefore reach the detector.

The multichannel detector consists of 18 channels, so that at a constant retardation voltage and a selected constant pass energy electrons in a defined energy interval are detected simultaneously. This is accomplished since distinct electron energies in a certain energy interval lead to different trajectories within the capac-

itor resulting in different arrival points (different channels) at the detector. Before arriving at the detector, the electrons are accelerated after the exit plane of the capacitor. The detector is a secondary-electron multiplier, so that the signal of each counted electron is amplified in order to process the signal electronically.

The spectrometer was run at a constant pass energy and a variable retardation voltage. Since the pass energy determines the energy resolution, the energy resolution ΔE was thus kept constant over the whole energy range[7]. All photoelectron spectra were taken at a pass energy of 3 eV. The energy resolution was determined by analyzing the width of a Fermi edge from a metal sample. The width of the measured Fermi edge consists of two contributions: the "physical" and the "technical" broadening. The physical broadening is described by the Fermi-Dirac distribution for electrons

$$f(\epsilon, T) = \frac{1}{\exp(\frac{\epsilon-\mu}{k_B T}) + 1} \tag{4.3}$$

where ϵ denotes the electron energy, T is the absolute temperature, k_B Boltzmann's constant, and μ the chemical potential. The width can be defined by the full width at half maximum of its first derivative. It can be shown that the temperature dependent broadening is $\approx 3.525 k_B T$. This corresponds to the width of the edge obtained between 15 and 85% of its height [33].

On the other hand, the Fermi edge is broadened by the energy resolution of the spectrometer and the bandwidth of the used light source. This is the so called "technical" broadening. Fig. 4.6 displays the Fermi edge of a Ag(100) sample taken at room temperature with laser pulses of 6 eV photon energy and a bandwidth of 40 meV. The "technical" energy resolution of the analyzer was then deduced to 90 ± 5 meV[8].

A -10 V bias was applied to the sample in order to improve the transmission of the analyzer.

4.2.2 Time-of flight spectrometer

In order to improve the energy resolution and to reduce the data-acquisition time for an energy-distribution curve, a time-of flight spectrometer (TOF) was built and installed into the UHV apparatus instead of the hemispherical analyzer. The home-built TOF consists of a $\approx$60 cm long metal tube which guarantees an electric-field free drift zone for electrons. In addition, it is surrounded by two μ-metal tubes which keep magnetic fields out of the drift zone. At one side photoemitted electrons can enter the TOF through an electrostatic lens system and propagate through the drift zone. Afterwards the electrons are accelerated for further amplification by secondary-electron multiplication using again channelplates.

[7]The analyzer could also be run in a mode with constant relative energy resolution $\frac{\Delta E}{E}$. This could be achieved by holding the retardation ratio of the input imaging system constant.

[8]Fits to the spectra obtained with a HeI-discharge lamp yield identical results.

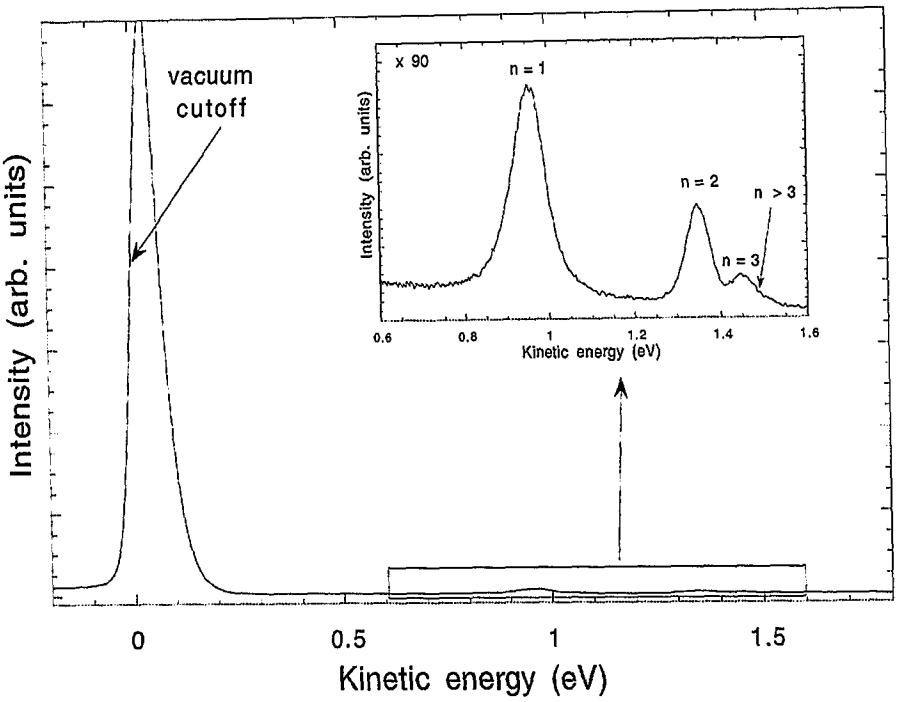

Figure 4.7: Two-colour 2PPE spectrum of the image-potential series on Cu(100) recorded with the homebuilt TOF.

The idea of the time-of flight technique is that electrons with different kinetic energies also need different times to travel through the field-free drift zone. The dispersive element, which also governs the energy resolution, therefore is the TOF length l. According to the relation between kinetic energy and velocity, the drift time t is inversely proportional to the square root of the electron energy E:

$$t \propto \frac{l}{\sqrt{E}} \quad . \tag{4.4}$$

According to equation 4.4, the drift-time difference becomes smaller the faster the electrons are. Hence, the energy resolution becomes worse with increasing kinetic energy.

The TOF output is monitored with an ultrafast multiple-event time digitizer (model P7886 from FAST ComTec) with a bin width of 500 ps. The board is capable of handling count rates of up to 2 GHz with no deadtime between timebins. In order to start its internal clock for the drift-time measurement, the P7886 PCI board is synchronized with the RegA output so that the laser pulses also serve as start signals for the electron detection. It should be noted that the energy resolution is limited if long laser pulses are used for the photoemission experiments. In our

case fs pulses are used so that the process of photoemission could be treated as an instantaneous process.

A problem arises for the detection of electrons with a kinetic energy close to zero, since these electrons are not able to reach the channelplates in a defined time. In addition, these electrons are sensitive even for small electric or magnetic stray fields between sample and TOF. In order to overcome this problem, all measurements were performed applying a small bias voltage of -1 V to the sample to detect the low-energy cutoff of the energy distribution curve. The energy calibration was determined from 2PPE measurements on a Cu(100) sample using variable photon energies. A variation in the photon energy leads to altered energy positions of several peaks and structures in the EDC. For instance, a change in the photon energy of 1.5 eV should therefore also result in a peak shift of 1.5 eV.

Figure 4.7 displays a typical two-colour 2PPE spectrum of the clean Cu(100) surface taken with the calibrated TOF. Photon energies of 4.65 eV and 1.55 eV were used for the pump- and probe pulses, respectively. The work function is deduced from the low energy cutoff to 4.63± 0.02 eV. The first three members of the image-potential state series are resolved with binding energies of 0.58±0.02 eV, 0.18±0.02 eV and 0.08±0.02 eV, respectively, relative to the vacuum level. These values are in excellent agreement with those reported in the literature[73]. The measured lifetimes for the first three states of 38 ± 7, 110 ± 18 and 295 ± 25 fs, respectively, are also in good agreement with previously published results [23].

The energy resolution of the TOF was determined from the full width at half maximum (FWHM) of the second image-potential state on Cu(100) when the pump pulse has already passed, i.e. at very long pump-probe delay times (see chapter 5). Since this state has a lifetime of more than 100 fs which corresponds to an intrinsic linewidth of around 5 meV, the measured linewidth is mainly governed by the instrumental function of the TOF spectrometer and the bandwidth of the probe pulse. Using a Gaussian lineshape accounting for the overall resolution, the fit procedure yields a value of $\Gamma = 50$ meV at a kinetic energy of 2.4 eV. The instrumental resolution of the TOF spectrometer can then be calculated by $\Gamma_{TOF} = \sqrt{\Gamma^2 - \Gamma^2_{probe}}$ since the contributions are additive upon convolution. The 25 nm bandwidth of the probe pulse corresponds to $\Gamma_{probe} = 40$ meV. Thus the energy resolution of the TOF spectrometer can be calculated to be 30 meV at a kinetic energy of 2.4 eV.

4.3 Sample preparation

All samples were cleaned in the preparation chamber under UHV conditions. Repeated cycles of Ar^+ sputtering (acceleration voltage: 500 eV, sample current: $\approx 6\mu$A), heating in oxygen at ≈700 K and subsequent annealing to 1000 K to remove any residual contamination were performed to obtain a clean and well ordered Pt(111) surface. The Ni surfaces were cleaned by a number of sputtering and

annealing (900 K) cycles. In order to remove remaining carbon from these surfaces, oxygen was adsorbed at 300 K followed by flash heating to 800 K.

The sample cleaness was checked using LEED, UPS and 2PPE. The samples were prepared as described above until

- a sharp low background LEED pattern was observed and
- the measured work function agrees within the limits of error with the value reported in literature.

It is worthwhile to note that the work function is very sensitive to surface contamination. Therefore, it could be used as a probe for the surface cleaness. H_2 or O_2 could be introduced into the UHV system through leak valves to cover the surfaces with adsorbates.

The Cu(100) crystal, which was used as reference system, was cleaned by cycles of sputtering and subsequent annealing to 600-700 K.

Chapter 5

Image-potential state dynamics on the Pt(111) surface

5.1 Introduction

A fundamental question in the investigation of unoccupied electronic states at solid surfaces deals with the decay and lifetimes of optically excited electrons. It is of great interest to understand the dynamics of electronic excitations on a fs timescale since they play a key role in a wide range of phenomena from chemical surface reactions to carrier dynamics at semiconductor interfaces[8, 74]. The advent of high-power lasersystems generating ultrashort light pulses has opened the possibility of studying electron dynamics on the fs- and ps timescale. A large number of experiments has been carried out to study both the dynamics of hot-electron distributions[9, 4, 17] and special electronic states (image-potential states, surface states) after optical excitation [23, 74]. Although Pt is widely used in catalysis and therefore a material of fundamental and practical interest [75, 76], up to now no time-resolved investigations on a fs timescale have been performed on those surfaces. This might be due to the fact that Pt surfaces possess large work functions which require the use of fs-pulses with photon energies between 5 eV and 6 eV. It is worthwhile to note that the use of ultrashort fs-laser pulses with photon energies close to 6 eV and a pulse duration shorter than 150 fs has not been realized so far. Thus, previous investigations on metals were restricted to photon energies below 5 eV which is insufficient for probing electronic states on Pt close to E_F or E_{Vac}.

So far, image-potential state dynamics have been investigated mainly on noble-metal surfaces of Cu and Ag[7, 22, 23, 56]. The obtained lifetimes can be understood quantitatively within the many-body framework of energy relaxation processes at surfaces[77, 78]. In contrast, little information is available about the time-dependent population of image-potential states on transition metal surfaces. A major difference of transition metals compared to noble metals is the presence of unoccupied d-bands. These states are expected to contribute to the decay of excited elctrons and may

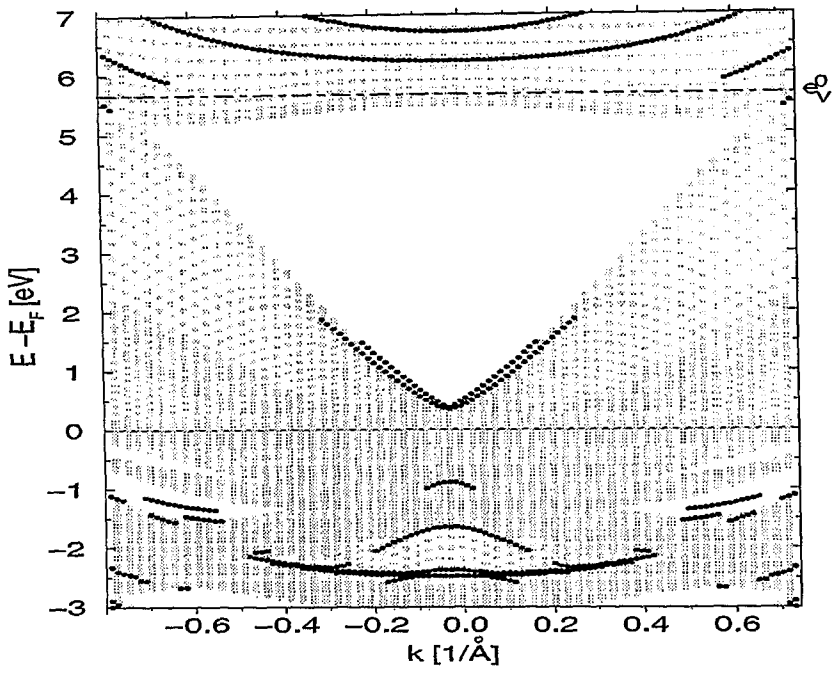

Figure 5.1: Projected bulk bandstructure (grey smbols) and states localized at the surface (black symbols) along the $\bar{K}-\bar{\Gamma}-\bar{M}$ direction. The $\bar{\Gamma}$ point corresponds to $k = 0$. From the Pt(111) film calculation only states have been included that had either more than 50% of their charge localized in the surface layer or more than 10% in the vacuum. The calculation has been performed by G. Bihlmayer and S. Blügel [79].

thus lead to different and much shorter relaxation times.

In the following sections we present our TR2PPE studies of the first two members of the image-potential state series on the clean and oxygen-covered Pt(111) surface. All measurements were performed using photon energies close to 6 eV and 3 eV in order to populate and probe the image-potential states, respectively. This chapter is arranged as follows. First the energy- and time-resolved measurements for the clean and oxygen-covered Pt(111) surface are presented. This is followed by the discussion of our results before a short summary concludes the chapter.

5.2 The clean Pt(111) surface

5.2.1 Electronic structure

Before we start our analysis with the determination of the image-potential state binding energies with respect to E_{Vac}, we first turn to a brief description of the electronic structure of the fcc-Pt(111) surface. Fig. 5.1 depicts the calculated two-dimensional bandstructure of the Pt(111) surface along the $\bar{K}-\bar{\Gamma}-\bar{M}$ direction. The surface electronic structure has been calculated by G. Bihlmayer and S. Blüegel with the use of the ab initio full-potential augmented plane wave (FLAPW) method [79]. The grey symbols correspond to regions in the projected Brillouin zone where electronic states exist. Black symbols represent states with an enhanced amplitude at the surface. The unoccupied surface state and the occupied surface resonance close to E_F are crystal-induced surface states. An occupied d-derived surface resonance observed below E_F has been reported in photoemission experiments [80, 81, 82], while the occupied sp-like surface state is visible in early IPE experiments about 0.5 eV above E_F [83].

As mentioned in chapter 3, the energy position of the image-potential series within the band gap plays a crucial role for their binding energies and lifetimes. Since image-potential states are pinned to the vacuum level E_{Vac}, the energy position of E_{Vac} relative to the upper band-gap edge is of enormous importance. Work-function values of 5.93 eV [84] and 5.98 eV [82, 85] for Pt(111) have been reported in the literature. Hence image-potential states on the Pt(111) surface lie close to the upper band-gap edge similar to the (111)-noble metal surfaces of Cu and Ag. Nevertheless, since the calculated value for the L_1 point is approximately 6 eV and may be also affected by some sort of error, the exact energy position of E_{Vac} with respect to the upper band-gap edge is still not known with an accuracy of less than 100 meV. According to equation 3.10, image-potential states with $n \geq 2$ are expected to converge rapidly towards E_{Vac} with binding energies of around 0.2 eV or less, so that states with higher n may be degenerate with bulk bands.

5.2.2 Energy-resolved spectra

In our experiment the work function of the clean Pt surface was determined from the width of the energy distribution curve obtained by using a HeI-discharge lamp (21.22 eV photon energy)[1]. Its value of 5.97±0.03 eV is in good agreement with the values reported previously [82, 84, 85]. In order to avoid space charge effects, the pump photon energy was set to 5.84 eV while a photon energy of 2.92 eV was used to probe the image-potential state population. The image-potential states can be populated via excitation from the occupied surface resonance or from a continuum of bulk states. From the 2PPE experiments presented here, we were not able to

[1]The work function could also be extracted from the low-energy cutoff in 2PPE experiments, if the position of the Fermi level is known.

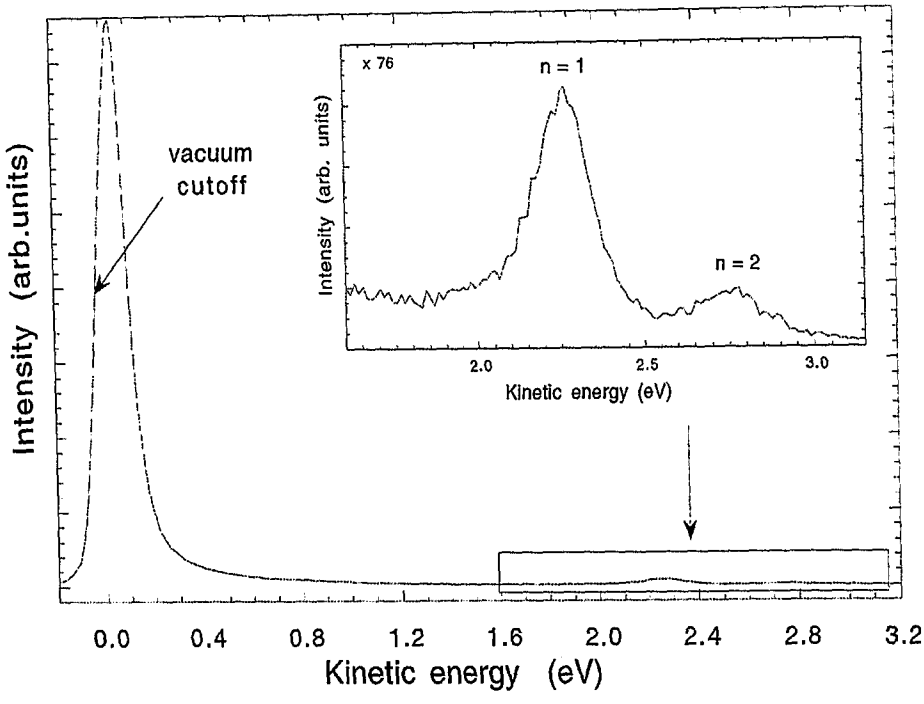

Figure 5.2: 2PPE spectrum of the Pt(111) surface obtained with photon energies of 5.84 eV and 2.92 eV for pump- and probe pulses, respectively. The EDC is dominated through the low energy cutoff. At higher kinetic energies the first two members of the image-potential series can be observed.

distinguish between these different excitation processes. The image-potential states can also be populated via a two-photon process involving two 2.92 eV photons (not shown) and probed with a third 2.92 eV photon. This would result in a background in the EDC independent of the pump-probe pulse delay. In order to avoid such three-photon processes, the pump-pulse intensity was reduced until the 3PPE signal of the image-potential states had been suppressed. Fig. 5.2 displays the EDC obtained at negligible time delay between pump and probe pulse. The electron energies are referenced to the low-energy cutoff which is the dominant feature in the 2PPE spectrum. The low-energy cutoff (or vacuum cutoff) is determined by the work function of the sample. Apart from the low-energy cutoff much weaker structures are visible at higher kinetic energies between 2 and 3 eV. This energy region is enlarged in the inset of Fig. 5.2. Two peaks are now clearly visible at kinetic energies of 2.27 eV and 2.76 eV which are

- sensitive upon contamination and
- exhibit relatively long lifetimes (see next section) and

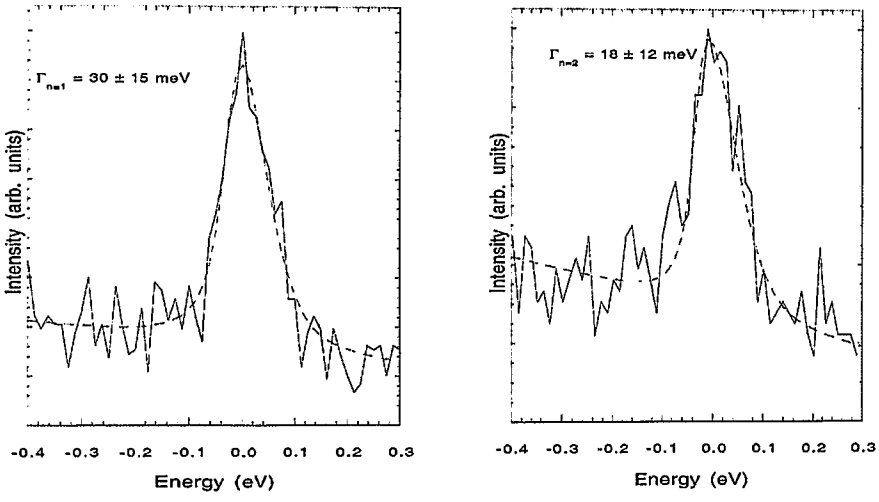

Figure 5.3: EDCs recorded at sufficiently large time delays between pump-and probe pulse. The $n = 1$ and $n = 2$ states are displayed in the left and right panel, respectively. In order to simplify the fit procedure, the spectra are referenced to the peak maxima. Accounting for the analyzer resolution of 90 meV and the bandwidth of the laser pulse, the overall instrumental energy resolution was deduced to 100 ± 5 meV. The fits (dashed lines) yield linewidths of $\Gamma_{n=1} = 30 \pm 15$ meV and $\Gamma_{n=2} = 18 \pm 12$ meV.

- also lie in the band gap (see next section).

The sensitivity upon contamination manifests itself in a decrease in intensity and a peak broadening with time. These observations demonstrate that the two peaks are surface states. In addition, a shift of the vacuum cutoff due to a work-function change goes along with similar shifts of the two observed peaks showing their fixed value to the vacuum level. Therefore the first two states with quantum numbers $n = 1$ and $n = 2$ are identified with binding energies of $E(1) = -0.65 \pm 0.05$ eV and $E(2) = -0.16 \pm 0.05$ eV with respect to E_{Vac}, respectively[2]. For the $n = 1$ state we obtained a quantum defect of $a = 0.144 \pm 0.041$ while the value for the second state is slightly higher. Nevertheless, they are identical within the experimental uncertainty[3].

The binding energy of the first image-potential state is close to the value of -0.63 eV obtained from inverse-photoemission spectroscopy [86, 87], but is 0.13 eV smaller than that reported by Kinoshita et al. [85]. The discrepancy between our

[2]The binding energy relative to E_{Vac} can be easily calculated by subtracting the probe-photon energy from the kinetic energy.

[3]A value of $E(2) = -0.185$ eV, which still lies within the given limits of error, also leads to a quantum defect $a = 0.144$.

value and the value reported by Kinoshitas group is unknown, since their reported work-function value of 5.98 eV is almost identical with our observation. However, our measured value for the binding energy of the $n = 1$ state agrees within the error margin with the calculated value of -0.70 ± 0.03 eV [88].

A peak narrowing of image-potential states with increasing pump-probe delay has been observed at various surfaces [23, 25, 89]. In a recent paper [23] this effect was assigned to the interplay between direct two-photon ionization and the step-by step photoemission process through an intermediate state [90]. Direct two-photon ionization occurs if pump and probe pulse are in temporal overlap and may cause a background in the EDC due to non-resonant 2PPE from initial states, which may contribute to the peak as well as the spectral widths of pump and probe pulses. However, these processes are only effective as long as the pulses are in temporal overlap. As soon as the population dynamics is decoupled from the pump pulse at longer delays times, the lifetime induced linewidths is measured. Therefore, using femtosecond pulses, the intrinsic linewidth in energy resolved spectra can only be detected at sufficiently large pump-probe pulse delays.

The spectra shown in Fig. 5.3 display the $n = 1$ (left panel) and the $n = 2$ state (right panel) at sufficient time delay when the pump pulse has already passed. The dashed lines are fits of a model function to the data points. Assuming a Lorentzian intrinsic lineshape, we used a convolution of a Lorentzian with a Gaussian to account for the finite analyzer resolution of 90 meV and the laser bandwidth of 40 meV. The overall energy resolution is then 100 meV. A linear background was substracted. The fit procedures yield the lifetime-dominated linewidths of $\Gamma = 30 \pm 15$ meV and $\Gamma = 18 \pm 12$ meV for the $n = 1$ and $n = 2$ state, respectively.

5.2.3 Fs-electron dynamics of image-potential states on Pt(111)

Time-resolved spectra

We now turn to the measurements of image-potential state populations on Pt(111) in the time domain. Fig. 5.4 displays a series of EDCs taken at different pump-probe delays. Each spectrum can be understood as a "snapshot" of the momentary image-potential state population after excitation. As mentioned in the previous chapter, the exact knowledge of the instrumental cross-correlation is of crucial importance for a precise determination of lifetimes in the fs-regime. The maximum of the cross-correlation curve corresponds to the maximum temporal overlap between pump- and probe pulse which determines the zero position in time ,$\Delta t = 0$, in our experiment. Hence a delay of 30 fs corresponds to a temporal shift of the maxima of pump-and probe pulses[4].

With increasing time delay Δt the relative intensities of the two image-potential states change. At very long delays the $n = 1$ state completely disappears and only the $n = 2$ state is still visible in the spectrum. This observation demonstrates

[4]It will be described later how we determined the $\Delta t = 0$ position.

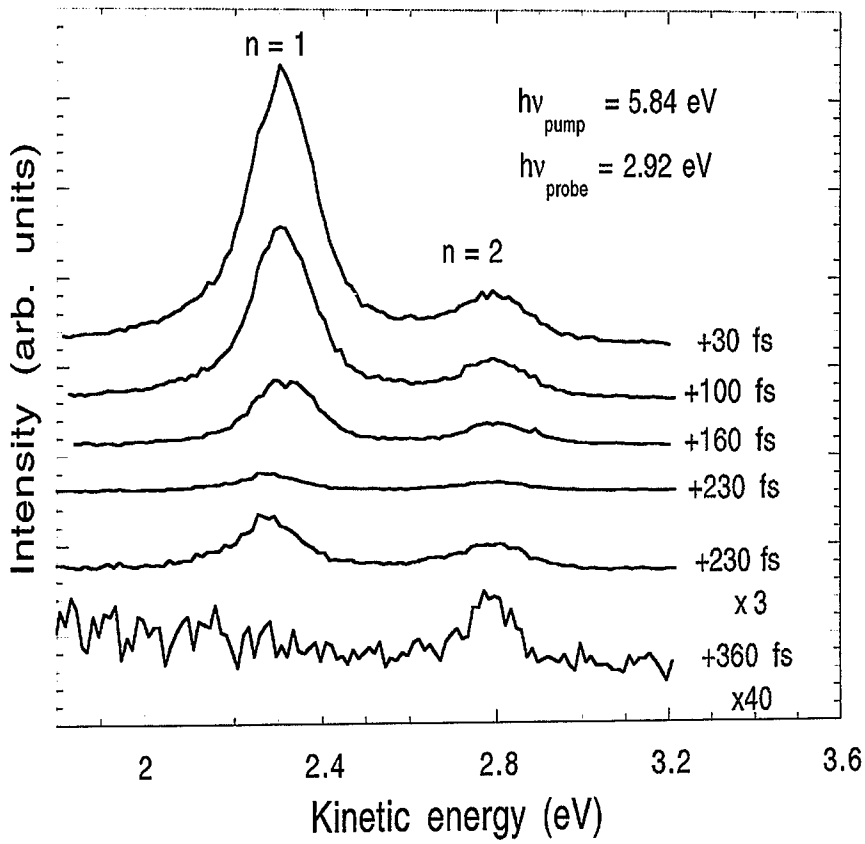

Figure 5.4: EDCs for the two resolved image-potential states on the clean Pt(111) surface taken at different times after $\Delta t = 0$.

qualitatively a longer lifetime of the second image-potential state. Another effect seen in the spectra espeacially for the $n = 2$ state is a decrease in the spectral width with increasing delay time. The broadening at short delay times is attributed to direct two-photon ionization as described in the previous section. In order to determine the image-potential state lifetimes quantitatively, the energy analyzer was set to the kinetic-energy values of the emitted photoelectrons corresponding to the two image-potential state peaks while the pump-probe delay was scanned. The results are shown in Fig. 5.5 for the $n = 1$ (b) and $n = 2$ (c) states (solid circles). The instrumental cross-correlation function was obtained on a contaminated Pt(111) surface where all surface states were quenched (curve (a) in Fig. 5.5, open squares)[5]. In order to ensure that the cross-correlation is not affected by hot electron lifetimes probed by a reversal excitation process, the energy analyzer was set to an energy

[5]An identical curve was obtained by setting the analyzer to kinetic energies around 1.9 eV on the clean Pt(111) surface.

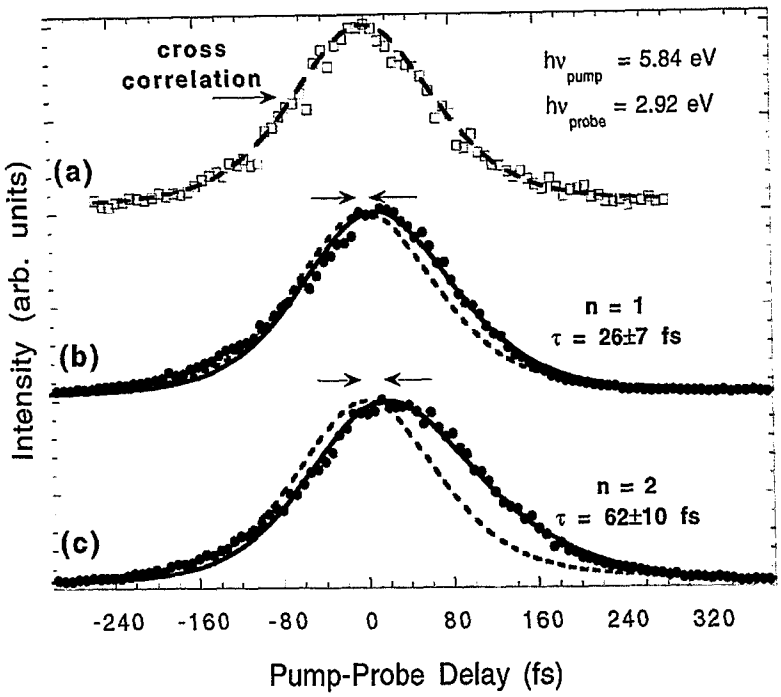

Figure 5.5: Transient responses of the $n = 1$ (middle panel) and $n = 2$ (bottom panel) image-potential states (filled circles). The cross-correlation trace (open squares, top panel) reflects the instrumental function described by a $sech^2$ function (dashed lines). From fits to the data (solid lines) lifetimes of 26 ± 7 fs and 62 ± 10 fs were obtained for the $n = 1$ and $n = 2$ state, respectively.

2.9 eV above E_F, where hot-electron lifetimes are negligible [8].

A "reversal excitation process" means that electrons are excited by the 2.92 eV pulse and probed by 5.84 eV pulses. The full width at half maximum of the instrumental cross-correlation trace was deduced to 152 fs by fitting a $sech^2$ function to the data (dashed line in Fig. 5.5). We determined the probe pulse length at the sample in an electronic autocorrelation setup to be 60 fs. The temporal resolution was, therefore, mainly limited by the pump pulse width of about 140 fs.[6].

The transient responses of the image-potential states are affected by lifetime effects in two different ways. We first concentrate on the transient response of the $n = 1$ state. The curve is shifted by 14 fs towards positive delay time. In addition, the curve is broadened by 18 fs. Both effects can be seen by comparing the data with the cross-correlation trace (dashed lines) indicating a clearly resolved finite lifetime

[6]Note that the pump pulse length was not bandwidth limited since it was not possible to compress this pulse after its generation. A compression setup would have been led to strong intensity attenuation of the fourth-harmonic beam.

of this state [39]. A by far stronger effect is seen in the transient response of the $n = 2$ state. The curve becomes significantly broader and shows a weak asymmetric line shape corroborating its longer lifetime seen in the 2PPE spectra of Fig. 5.4.

Analysis of the time-resolved spectra

For a quantitative evaluation of image-potential state population dynamics, one has to take into acount that the lifetimes are in the range of pump and probe pulse durations. Therefore, substantial changes of the image-potential state population occur during the pump pulse. Thus, a theoretical model must be applied which excplicitly takes into account the coupling of the pump-pulse laser field $E(t)\cdot cos(\omega t)$ with the transition-dipole moment [91], $E(t)$ denotes the envelope of the pulse. The response of the system to an optical perturbation can be described using the Liouville-von Neumann equation [65]

$$\frac{d\rho}{dt} = \frac{1}{i\hbar}[H_0 + V, \rho] + (\frac{d\rho_{diss}}{dt})_{relax} \tag{5.1}$$

which governs the evolution of the density matrix ρ in a three level system including an initial state $|i\rangle$ below E_F, the image-potential state as intermediate state $|n\rangle$ and a final state $|f\rangle$ above E_{Vac}. H_0 denotes the unperturbed Hamiltonian while V describes the perturbation due to the laser field.

The dissipative term ρ_{diss} describes energy and phase relaxation on a phenomenological basis. The energy relaxation is governed by inelastic electron scattering events leading to a decay via electron-hole pair creation while quasi elastic scattering processes with phonons and defects destroy the coherence between the different electronic levels $|i\rangle$, $|n\rangle$ and $|f\rangle$ but leave the electrons in their excited state. The loss in coherence is referred to as "pure" dephasing. Both energy and phase relaxation times contribute to the intrinsic linewidth Γ of an image-potential state according to

$$\Gamma = \hbar(\frac{2}{T_n^*} + \frac{1}{\tau_n}) \quad . \tag{5.2}$$

The parameters τ_n and T_n^* denote the energy-relaxation time (or lifetime) and the pure dephasing time, respectively.

Due to the small light intensities used in the experiments, the transitions $|f\rangle \rightarrow |n\rangle$ and $|n\rangle \rightarrow |i\rangle$ can be neglected [91]. To the lowest order perturbation theory, i.e. neglecting all saturation effects, the Liouville-von Neumann equation is referred to as optical Bloch equations [91, 23]. The formalism based on the optical Bloch equations is rather complex and is described in detail in the literature [91, 65, 92].

For some cases it has been shown that this formalism can be simplified [91, 92, 93]. For example, assuming a continuum of initial states and vanishing dephasing in the initial and intermediate states, the transient response of the intermediate state can be described by a convolution of the instrumental cross-correlation

$$I_{2PPE}(t) \propto \int_{-\infty}^{\infty} I_{pump}(t') I_{probe}(t - t') dt' \tag{5.3}$$

with an exponential function which accounts for the population decay [92]. $I_{pump,probe}$ denote the light intensities of the laser pulses and I_{2PPE} is the measured signal from

the electronic cross-correlation. This resembles the dependence of the excited state population obtained from the much simpler rate equation model:

$$\frac{d\rho_{nn}}{dt} = -\frac{\rho_{nn}}{\tau_n} + E(t) \quad . \tag{5.4}$$

ρ_{nn} denotes the population of the intermediate state $|n\rangle$, E denotes the laser field of pump and probe pulse.

However, dephasing processes are expected to occur during the excitation process [9, 94] and, thus, one may argue that the approximation made above seems to fail in the quantitative description of the temporal response. On the other hand, introducing the dephasing time to the fit procedure, the fit function is overdetermined [92]. Therefore, a precise analysis of the dephasing time can only be performed using the technique of interferometric TR2PPE [9]. Moreover, the transient response of the intermediate state is a direct measure of its population. Assuming that the elastic scattering events leave the electrons in the excited state [95] and that T_n^* exceeds the lifetime τ_n, which has been indeed observed [65, 23], to a first approximation the above mentioned model can be applied.

In fact, it has empirically been shown that the choice of a rate-equation model or the optical-Bloch equations yields identical lifetime values [56, 93, 39, 96]. Therefore, applying a rate equation model might be favourable [93, 96]. Examples for this are lifetimes of image states on Cu(111) and Cu(100) [56, 39]. On Cu(111), values of 20 ± 3 and 18 ± 5 fs for the $n = 1$ state have been reported using the rate-equation model or the optical Bloch equations, respectively. One should note that the lifetime value of 10 ± 3 fs [39] obtained using the optical-Bloch equations has been revised by the authors in a later paper [56]. Using a rate-equation model, we have obtained lifetime values for the first three image states on Cu(100) (see chapter 4) which are in excellent agreement with those reported in the literature [23].

We, therefore, used a convolution of the instrumental cross-correlation and an exponential decay function to model our data. The fits (solid lines in Fig. 5.5) yield lifetimes of $\tau_1 = 26 \pm 7$ fs and $\tau_2 = 62 \pm 10$ fs for the $n = 1$ and $n = 2$ state on Pt(111), respectively. For sufficient long lifetimes it has been demonstrated [23] that the decay of the image-potential state population shows a single-exponential behaviour after the pump pulse has passed. Therefore the lifetime can be deduced from the slope of the curve in a semi-logarithmic plot. Because of the relatively short lifetime of the $n = 1$ state, this procedure was only applied to the $n = 2$ state. The fit yields an identical lifetime value for the $n = 2$ state.

5.3 The oxygen-covered Pt(111) surface

The idea of controlling electron dynamics on ultrashort time scales can be extended to the manipulation of image-potential state lifetimes. A simple method to alter the physical properties of a surface consists of the adsorption of atoms or molecules.

Changes of the geometrical structure due to adsorbates affect the surface electronic structure and can alter binding energies and population dynamics of surface states. In addition, adsorbate induced work-function changes may also significantly affect image-potential state lifetimes. An example where a work-function change leads to an increasd lifetime is Cu(111) [56]. One monolayer Xe on Cu(111) reduces the work function of 4.90 eV (clean surface) to 4.40 eV. Due to the Xe adsorption the Rydberg series is shifted towards the band-gap center since the image-potential states are pinned to the vacuum level. This leads to stronger damping of the electron wave function inside the crystal and hence to an increased lifetime. An additional effect contributes from the decoupling of the image state from the crystal. The polarization of the Xe layer leads to a shift of the image plane away from the surface which in turn results in a weaker coupling of the electron with bulk states.

However, there are still open questions concerning the influence of the electronic surface structure on the image-potential state decay. The dynamics of both hot electron cascades and electronic states are governed by the number of available occupied and unoccupied states around E_F [78, 97]. Especially surface states are expected to serve as effective decay channels for electrons populating image states due to their localization at the surface. To our knowledge, up to now no direct observations in time-resolved experiments have been made which elucidate the influence of the altered electronic structure around E_F on the decay of image-potential states.

The adsorption of oxygen on the Pt(111) surface has been the focus of a large number of theoretical and experimental investigations [98, 99, 100, 101]. A modification of the geometrical surface structure has been reported [100] which implies significant changes in the electronic structure [82]. For our investigation two aspects of the oxygen induced adaptations are of relevance: the observed change of the electronic structure close to E_F and a small work-function variation which is expected to lead to only a small energy shift of the first-image potential state within the band gap [82, 98].

5.3.1 Energy-resolved spectra

On Pt(111), oxygen adsorbs dissociatively at temperatures above 170 K [99]. The adsorption at room temperature results in a well ordered p(2x2) LEED pattern at a saturation coverage of 0.25 monolayers (ML) [99, 100]. The work function for the Pt(111)-p(2x2)-O surface was deduced to 6.16 ± 0.04 eV. This corresponds to an increase of 0.19 eV relative to clean Pt(111) in good agreement to the work-function change observed by Parker et al. [98, 99].

Using a photon energy of 5.84 eV for the excitation process, only the $n = 1$ state was resolved in the EDC at delay times of $\Delta t \approx 0$ fs. The absence of the second state in the spectrum can be explained by the work-function change due to the adsorption of oxygen. As mentioned above, image-potential states are pinned to the vacuum level. A work-function increase, therefore, leads to an energy shift of the image-potential series away from E_F. Thus the excitation energy of 5.84 eV is

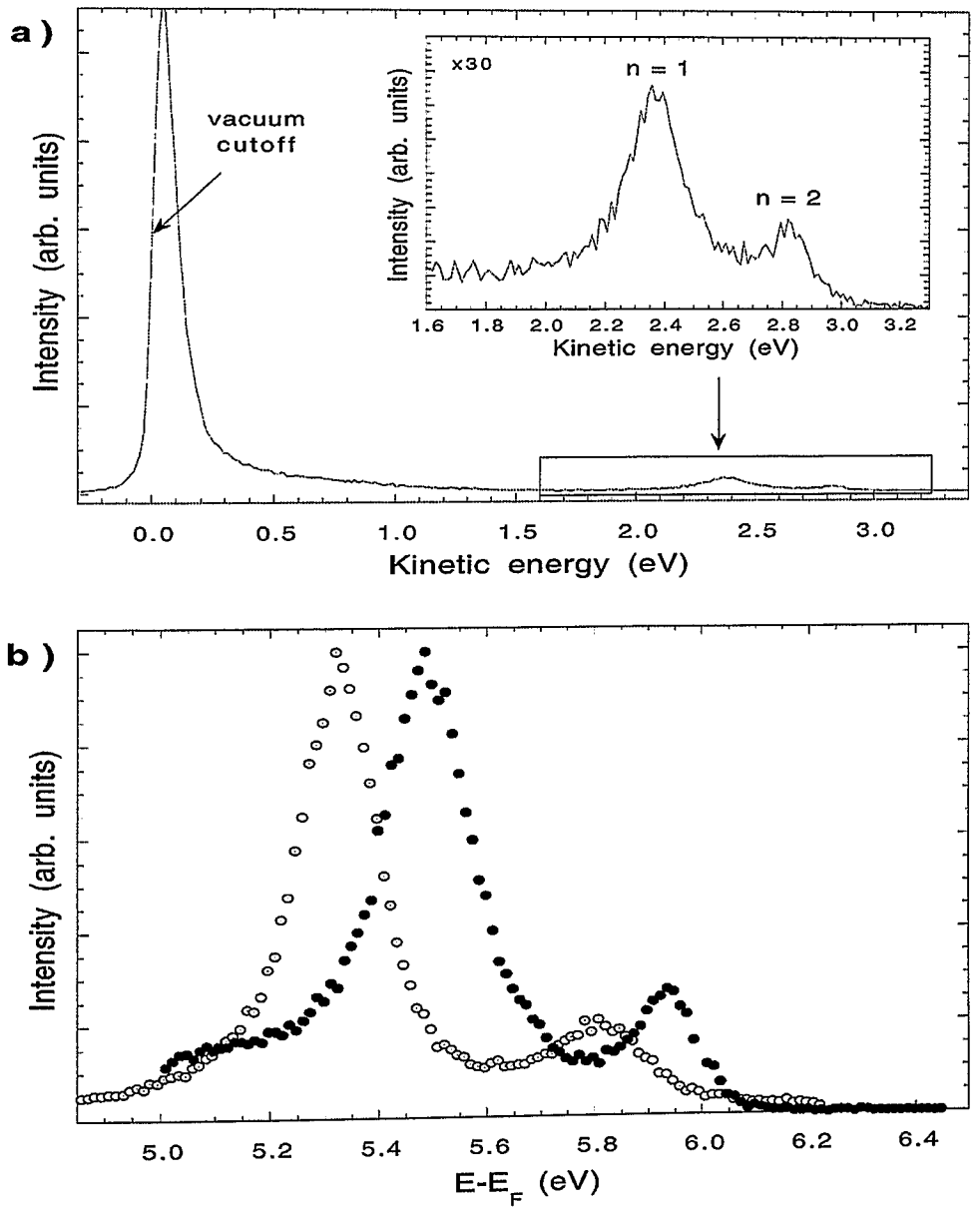

Figure 5.6: a) EDC of the Pt(111)-p(2x2)-O surface recorded in a two-colour experiment at $\Delta t = 0$ fs. Photon energies of 6.06 eV and 3.03 eV were used for the pump and probe pulses, respectively. The peaks between 2 eV and 3 eV correspond to the first two image-potential states. A work function of 6.16 eV was deduced from the low-energy cutoff. b) Due to the work-function change the image-potential states on the oxygen-covered surface (filled circles) are shifted to higher energies relative to E_F compared to those on the clean surface (open circles). This behaviour demonstrates the pinning relative to the vacuum level.

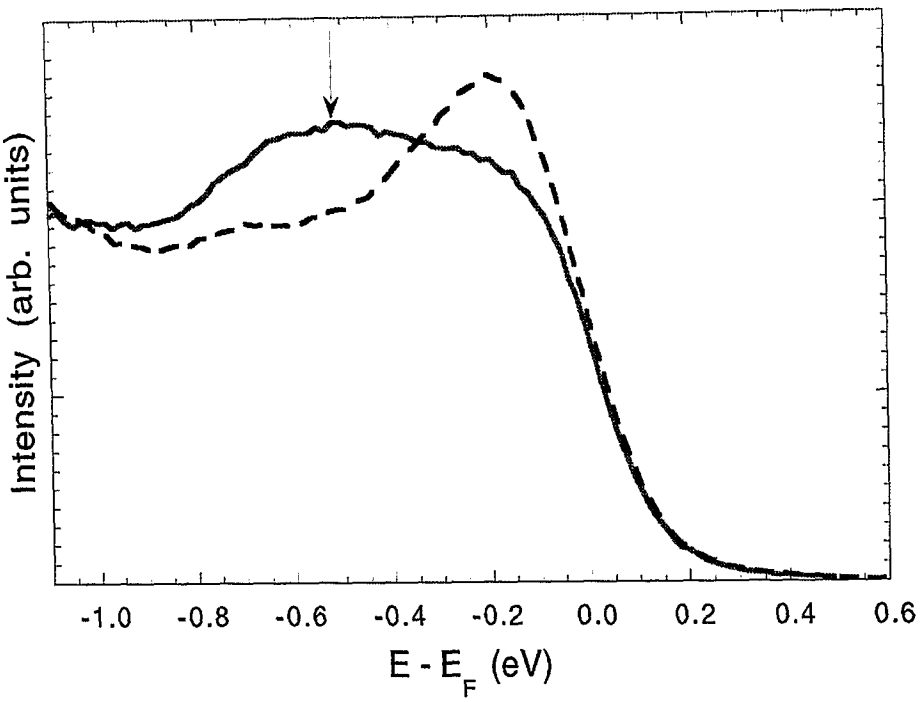

Figure 5.7: 2PPE spectra of the clean (solid line) and oxygen-covered (dashed line) Pt(111) surface obtained with a photon energy of 4.47 eV. The occupied surface resonance on the clean surface is marked by an arrow.

insufficient to populate the $n = 2$ state. We checked this by tuning the Ti:sapphire output to a wavelength of 820 nm. This gives us photon energies of 6.06 eV and 3.03 eV for the pump and probe pulse, respectively. The complete spectrum at zero delay time obtained with these photon energies is shown in Fig. 5.6a). Indeed two peaks are observed at kinetic energies between 2 eV and 3 eV which represent the first two Rydberg states on the Pt(111)-(2x2)-O surface with binding energies of -0.67 ± 0.05 eV and -0.19 ± 0.05 eV, respectively.

The increased binding energies reflect the altered energy positions of the two states within the gap of the projected bulk-band structure. Due to the work-function increase the image states are shifted towards the upper band-gap edge, thus, changing the phase Φ_c upon reflection at the crystal. This in turn leads to reduced quantum defects of $a = 0.126$ and $a = 0.115$ for the $n = 1$ and $n = 2$ state, respectively. Since the work function is the energy difference between E_{Vac} and E_F, the energy shift of the image-potential states can be visualized in a plot with an energy scale referenced to E_F. Fig. 5.6b) displays EDCs for the clean (open circles) and oxygen covered (filled circles) surface. The shifts towards higher energies with respect to E_F for states on the oxygen-covered surface are clearly visible. Since the

$n = 2$ state narrows upon oxygen adsorption, one would argue that its lifetime is increased according to equation 5.2. As will be shown later, the narrowing of the $n = 2$ peak on the oxygen-covered surface can not be explained by an increased lifetime of this state.

Additional measurements have been performed to investigate the influence of oxygen adsorption on the valence electronic structure. For this purpose the frequency-tripled laser output with a photon energy of 4.47 eV was used. Fig. 5.7 shows the energy distribution curves of the valence band from the clean (solid line) and oxygen-covered (dashed line) Pt(111) surface obtained with 2PPE. A feature at an energy of -0.55 ± 0.05 eV below E_F is seen for the clean surface (marked by an arrow) which is quenched under oxygen adsorption. This structure was also observed previously [80, 82] and was assigned to an occupied surface resonance. Such a surface resonance is also apparent in Fig. 5.1 near $\bar{\Gamma}$ at energy slightly lower than that observed in the experiments. In addition the density of states (DOS) near E_F is considerable enhanced by oxygen adsorption.

5.3.2 Image-potential state dynamics on the Pt(111)-(2x2)-O surface

The transient response of the $n = 1$ (curve b)) and $n = 2$ (curve c)) image-potential states on the oxygen-covered surface is displayed in Fig. 5.8. The instrumental cross-correlation with a full width at half maximum of 270 fs is also shown (curve a), the dashed curve is a fit to the data using a $sech^2$ function). Unfortunately, the cross-correlation width is larger than for the lower photon energies used on the clean Pt(111) surface. The decrease in time resolution is assigned to an increased pump-pulse duration since the probe-pulse length was still determined to 60 fs. The duration of the pump pulse was deduced from the instrumental cross-correlation trace to 260 ± 6 fs[7]. Nevertheless, we were able to reproduce the image-potential state lifetimes on clean Pt(111) for this higher photon energy. A lifetime of 32 ± 10 fs for the $n = 2$ state on Pt(111)-p(2x2)-O was deduced from a fit (solid line) to the data in Fig. 5.8. The lifetime for the $n = 1$ state is much shorter as can be seen from the transient response which follows directly the instrumental cross-correlation trace. We estimated an upper limit of 20 fs for the lifetime of this state keeping in mind that the temporal resolution is reduced due to the relatively broad cross-correlation at these photon energies.

[7]We assume that uncompensated chirps due to group-velocity dispersion effects dominate the broadening. However, we can not rule out losses in the high-energy tail of the frequency spectrum in the second frequency-conversion stage.

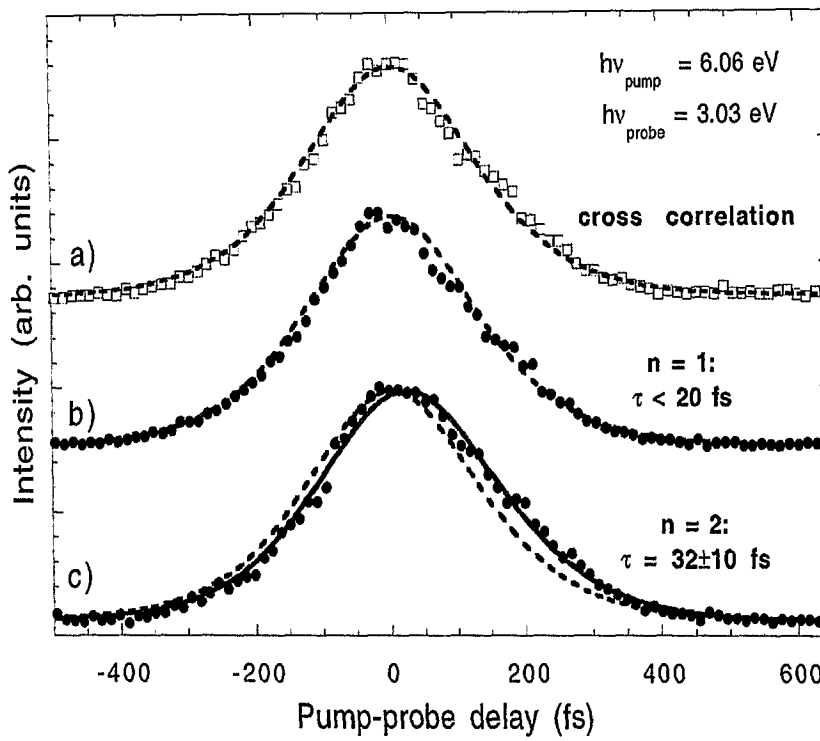

Figure 5.8: Transient response of the image-potential states on the oxygen covered surface are shown (curves b) and c)). Using a $sech^2$ function (dashed line) to model the instrumental cross-correlation trace (curve a)) one obtains a full width at half maximum of 270 fs. It can be seen that the transient response of the first image-potential state (middle panel, curve b)) can be described by the $sech^2$ fit of the cross-correlation curve (dashed line). The fit to the $n = 2$ state yields a value of 32 ± 10 fs.

5.4 Discussion

The clean Pt(111) surface

The measured longer lifetime for the $n = 2$ state of $\tau_{n=2}^{Pt(111)} = 62 \pm 10$ fs compared to the lifetime of $\tau_{n=1}^{Pt(111)} = 26 \pm 7$ fs for the first image-potential state can be explained by a weaker wave-function overlap of this state with bulk bands, the crystal-induced surface state and the surface resonance. As mentioned in chapter 3, image-potential states with increasing quantum number, n, are localized further and further into the vacuum region. This leads to a reduced wave-function overlap with bulk states and the lifetime is expected to increase according to the n^3 power law (equation 3.13).

However, it has been shown that on (111) surfaces of Cu and Ag the $n = 2$ lifetimes were dramatically reduced to below 20 fs [56, 25]. Both the measured value $\tau_{n=2}^{Cu(111)}$ and the estimated value $\tau_{n=2}^{Ag(111)}$ are slightly smaller than the lifetimes of the first image-potential states on those surfaces. In order to explain these results one has to take into account the energy position of states with $n \geq 2$ with respect to the band gap.

On those surfaces the $n = 2$ states lie above the upper band-gap edge (L_1 point) and are degenerate with bulk bands. Their wavefunctions penetrate deeper into the crystal and even hybridize with bulk bands. It has been shown that such an elastic resonance between the surface state and a continuum of bulk states yields the main contribution to the population decay of image states. This, thus, reduces the image-state lifetime dramatically.

As soon as the $n = 2$ state is shifted out of the gap, its lifetime is drastically reduced and even shorter than the lifetime of the $n = 1$ state. Wolf et al. [56] have demonstrated on the xenon-covered Cu(111) surface that the lifetime $\tau_{n=2}^{Cu(111)} = 40 \pm 10$ fs for the second image state is still significantly shorter than $\tau_{n=1}^{Cu(111)} = 75 \pm 15$ fs if the $n = 2$ state is moved close above ($\approx$ 100 meV) the upper gap edge[8]. One should note that the authors assign the lifetime increase for the $n = 2$ state to a decoupling of the image-state wave function from the substrate caused by the xenon monolayer.

Therefore we conclude that on Pt(111) both states still lie inside the band gap. This can also be inferred from an evaluation of the quantum defect a. The value obtained for Pt(111) is intermediate to those of Cu(111) and Cu(100) (and also to those of Ag(111) and Ag(100)), since on Cu(100) (Ag(100)) the image-potential series lies closer to the center of the band gap.

The lifetimes of image states on Pt(111) are between those measured on the (111) and (100) surfaces of the noble metals Cu and Ag. For example, the value of $\tau_{n=1}^{Pt(111)} = 26 \pm 7$ fs is slightly higher than that on clean Cu(111) ($\tau_{n=1}^{Cu(111)} =$

[8]The adsorption of one monolayer xenon reduces the work function of the clean Cu(111) surface by 0.5 eV thus shifting the $n = 2$ state towards the gap edge.

18 ± 5 fs), but somewhat smaller than the value $\tau_{n=1}^{Cu(100)} = 40 \pm 6$ fs obtained for Cu(100) [23]. A recent TR2PPE study [60] of the first image-potential state on the nearly isoelectronic Pd(111) surface yields a lifetime of $\tau_{n=1}^{Pd(111)} = 25 \pm 4$ fs which is comparable to our value. This result might be surprising since on Pd(111) the vacuum level and the image-potential state series lie closer to the center of the bulk-band gap. Unfortunately no experimental lifetime values for higher image states were presented since the available pump-photon energies were insufficient to populate higher states on Pd(111).

The measured intrinsic linewidth for the two image-potential states on Pt(111) obtained at large time delays Δt between pump and probe pulse (see section 5.2.1) correspond to lifetimes of 22 ± 11 and 36 ± 24 fs for the $n = 1$ and $n = 2$ state, respectively. The agreement between the measured intrinsic linewidths and the lifetimes is only satisfying for the first image state. A possible explanation for the deviation in the lifetime values for the second state could be the limited resolution of the hemispherical analyzer. Nevertheless, both linewidth values lead to shorter lifetimes compared to those obtained in the time-resolved experiment. This effect was also observed on the Pd(111) surface [60] and was explained by pure dephasing. According to equation 5.2, the linewidth of an image-potential state is also affected by quasi-elastic scattering processes which do not change the occupancy of the state. Such processes could be attributed to quasi-elastic scattering with phonons or residual defects on the surface.

Following our measurements the group of Chulkov and Echenique have carried out calculations on the basis of a many particle formalism. Within this theoretical approach [78] electron-electron scattering is assumed to govern the decay via electron-hole pair creation. The excited electron is scattered from a state of energy E_i to a final state of energy $E_f > E_F$ by promoting an electron below E_F to a final state above E_F. For the calculation of the damping rate (inverse lifetime) for the $n = 1, 2$ image states they have constructed a one-dimensional model potential for the direction perpendicular to the surface [102]. To this end they used the width and position of the energy gap at $\bar{\Gamma}$, the *sp*-surface state energy position of 0.4 eV together with the experimentally determined binding energy of -0.65 eV relative to E_{Vac} for the $n = 1$ image state. Their calculations yield lifetimes of $\tau_{n=1}^{Pt(111)} = 29$ fs and $\tau_{n=2}^{Pt(111)} = 73$ fs for the two image-potential states.

The lifetime values for the $n = 1$ state obtained from experiment and theory agree within the accuracy. Nevertheless, the calculated lifetimes are slightly higher than those measured with TR2PPE, especially the value for the second image state. A possible explanation for this behaviour is that the theoretical model does not account for *d*-electrons which also contribute to the decay. Bulk Pt possesses d-orbitals which cross the Fermi level. These *d*-states are also involved in the decay and, thus, should explain the lower measured lifetime values.

The Pt(111)-p(2x2)-O surface

We now turn the discussion to the oxygen-covered surface. The adsorption of oxygen results in a well ordered Pt(111)-p(2x2)-O surface structure that was found to involve a slight rearrangement of the Pt substrate atoms [100]. Compared to the clean surface, the lifetime of the $n = 2$ state is reduced by a factor of 2, whereas for the lifetime of the first image state only an upper limit can be estimated. Several effects can be responsible for the decrease in the image-state lifetime:

- The oxygen atoms at the surface may act as additional scattering centers for electrons in image-potential states.

  Schuppler et al. have observed a linewidth broadening of image-potential states on a Ag(100) surface under the disordered adsorption of oxygen [55]. The linewidths of the image states were observed to increase linearly with oxygen exposure indicating shorter lifetimes because of more effective scattering of electrons in image states with O-atoms. This may play a role on a surface with disordered adatoms, but is expected to be negligible on surfaces with well ordered layers of adatoms [22, 56, 103]. On the contrary, McNeill et al. and Wolf et al. demonstrated independently that ordered layers of rare-gas adatoms increase the image-state lifetimes.

- A shift of the image-potential states towards the upper band-gap edge due to the increased work function may reduce the damping of their wave functions.

  Due to the increased work function of 0.19 eV only the second image-potential state can be shifted out of the band gap. As a result its wave function penetrates deeper into the crystal leading to a much stronger coupling with adjacent bulk bands. This resembles the situation on Ag(111) and Cu(111) [25, 56]. As described above, in this system the $n = 2$ state shows a shorter lifetime compared to the first image-potential state. However, on the Pt(111)-(2x2)-O surface this effect is unlikely since both image-state lifetimes are reduced compared to clean Pt(111).

- The occurence and occupation of crystal-induced surface states located mainly in the topmost layer leads to an enhanced overlap with image-potential states. This also changes the available phase space for electron-hole pair decay.

It has been shown that for the decay of image-potential electrons into electron-hole pairs other surface states play a dominant role [77, 78]. For example as will be shown in the next chapter, surface states are assumed to be one reason for the relatively broad linewidth of the $n = 1$ state on Ni(111). As mentioned in the previous section, the surface resonance observed -0.55 eV below E_F is quenched under oxygen adsorption. It is presently not clear whether this state is simply depopulated and shifted above E_F [81] or whether a major reorganization of the valence electronic structure occurs. The latter seems more likely since a small oxygen

surface	method	$\tau_{n=1}$ fs	$\tau_{n=2}$ fs
Pt(111)	TR2PPE	26 ± 7	62 ± 9
	2PPE	22 ± 11	36 ± 24
	theory	29	73
Pt(111)-p(2x2)-O	TR2PPE	< 20	32 ± 10

Table 5.1: Lifetimes for the first two image-potential states on the clean and oxygen-covered Pt(111) surface obtained with different methods. The values obtained with TR2PPE were measured directly in the time domain whereas the values of 22 ± 11 and 36 ± 24 fs result from the deduced linewidths obtained with 2PPE. The theoretical values were calculated by the group of E.V. Chulkov and P.M. Echenique.

induced buckling reconstruction of the Pt substrate was observed [100]. Fig 5.7 provides evidence that this leads to a rearrangement in the DOS around E_F. This could also create additional unoccupied states that influence the relaxation process, hence accelerating the decay of the image-potential states. In addition, the work function increase for the oxygen-covered surface increases the number of available final states for the decay process. This is also expected to shorten the image-state lifetimes.

Concluding remarks

The results for the clean and oxygen-covered surface are listed in table 5.1. The lifetime values obtained using 2PPE are deduced from the intrinsic linewidths and are somewhat shorter than those obtained in the time domain. This observation is attributed to elastic scattering at defects or phonons. In addition, we have shown that experimental and theoretical data are in excellent agreement. The observed long lifetime of the $n = 2$ state on the clean surface reflects its energy position inside the band gap. This is in contrast to the (111) surfaces of Cu and Ag, where the $n = 2$ lifetime is strongly reduced. After oxygen adsorption a Pt(111)-p(2x2)-O structure is formed leading to a quenching of the occupied surface resonance and a major rearrangement of the surface DOS. This is in turn mainly responsible for a faster depopulation of the image-potential states due to an increased number of available final states.

Chapter 6

Nickel: unusually short lifetimes of image-potential states

6.1 Introduction

Although the $3d$-transition metals Fe, Co, and Ni are of great fundamental and technical importance, it is remarkable that the first direct lifetime investigations of excited electrons in the time domain have only been reported as late as 1997 [104]. This doesn't mean that electron relaxation phenomena on these surfaces are of minor interest. On the contrary, since d-bands cross the Fermi level it becomes possible to study the inluence of d-states on the decay of optically excited electrons. This is of importance for magnetic materials which also provide the opportunity to study spin-dependent interactions and electron lifetimes for minority and majority spins [97, 104, 105]. Finally the hot-electron distribution following an intense optical excitation governs the demagnetisation speed of ferromagnetic samples [13]. Nevertheless, demagetization processes and scattering dynamics of excited electrons on magnetic surfaces are still quite poorly understood and remain controversial.

Surface states provide further information about the physical properties of a surface. Due to their extreme surface sensitivity, surface states can be used as probes for the magnetic properties of the topmost atomic layer. In fact, it has been shown that the exchange splitting of bulk d-bands also causes an exchange splitting of surface states[106]. Such a splitting has also been observed for image-potential states [107, 108]. However, this splitting is somewhat smaller compared to crystal induced surface states since image states are localized further away from the surface in the vacuum region [107].

There remain open questions concerning the lifetimes of image-states on magnetic surfaces. Using high resolution 2PPE, intrinsic linewidth measurements of the $n = 1$ state on Fe, Co, and Ni surfaces linewidth values have been reported which are more than 4 times larger than those on noble metal surfaces [61, 67]. Since the $n = 1$ states on Ni(111) and Ni(100) are located closer to the gap center compared to those

on Cu(111) or Ag(111), one would expect an opposite trend, i.e. smaller linewidths. From the localization of the $n = 1$ state on Ni(100) a lifetime similar to the (100) faces of Cu and Ag can be expected [23]. The large linewidth can be a consequence of the exchange splitting of the image states. Nevertheless, a splitting could not be made exclusively responsible for the observed linewidths since 2PPE experiments suggest only upper limits for the splitting on Ni [61], while spin-polarized inverse photoemission experiments yield values of 13 ± 13 and 18 ± 3 meV for Ni(100) and Ni(111), respectively [108, 109]. The reported values are too small to account for the observed linewidth alone [61, 108, 109]. In addition, theory predicts a splitting between 6 and 13 meV for Ni(100) [111] which is also insufficient to explain the large measured linewidth.

As mentioned earlier, the measured intrinsic linewidth Γ of an excited state obtained with 2PPE does not necessarily correspond to the lifetime τ via the relation

$$\Gamma = \frac{\hbar}{\tau} \tag{6.1}$$

since elastic scattering processes (scattering with phonons, electrons, or defects) may contribute to the observed linewidth.

Moreover, it has been shown that initial state effects may affect the measured linewidth in 2PPE experiments, as well. Early 2PPE studies on Cu(111) yield a linewidth of 16 ± 4 meV [61] which corresponds to a lifetime of 40 fs (equation 6.1). Using TR2PPE, a lifetime of only 18 ± 5 fs was obtained [56] which in combination with the intrinsic linewidth therefore would lead to a non-physical negative dephasing time. In a later paper this discrepancy was explained by the photon energy used in the linewidth measurement [19]. If the $n = 1$ state is resonantly ($\hbar\omega = 4.48$ eV) populated from the occupied *sp*-derived surface state, a peak narrowing can be observed compared to the non-resonant case, so that the initial state from which the excitation starts has also to be taken into account.

The problematic nature of linewidth studies in combination with the still open question concerning the exact lifetimes of image states on magnetic $3d$-transition metal surfaces warrants a more accurate investigation. Time-resolved measurements directly probe the population dynamics of image states so that these techniques are superior in the exact determination of lifetimes. Pure dephasing and initial state effects do not affect the time-dependent population of those states and can be separated.

In the following two sections, we present time-resolved studies of image-potential states on Ni(100) and Ni(111), which are in fact the first measurements of image-potential states on magnetic surfaces in the time domain. These experiments demand excellent time resolution due to the short lifetimes. This is followed by a discussion which includes a general theoretical approach in order to calculate the damping of the image-state wave function which in turn is expected to influence the lifetime. A short summary concludes the chapter.

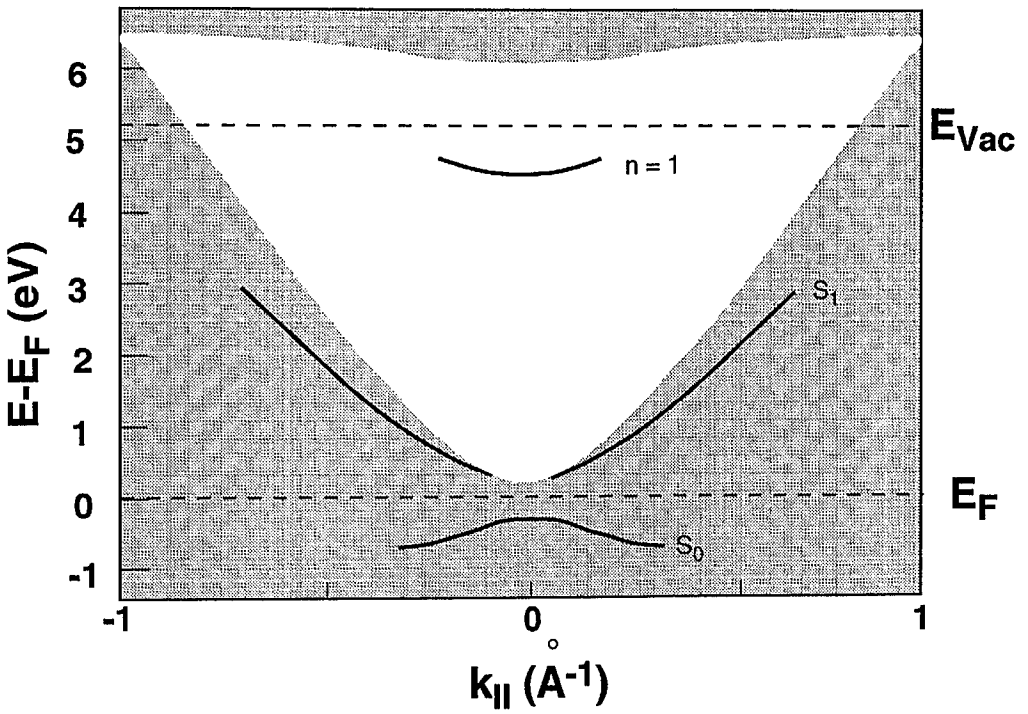

Figure 6.1: Projected bulk bandstructure along the $\bar{\Gamma}\bar{M}'$ direction for the (111) orientation of Ni taken from reference [87]. Thick lines represent states with an enhanced amplitude at the surface. The states labeled S_0 and S_1 are bulk induced surface states [87, 112]. The vacuum level lies well below the upper band gap edge and is positioned 5.2 eV above E_F. At a binding energy of around -0.8 eV with respect to E_{Vac} the first member of the image-potential series is shown.

6.2 Image-potential state dynamics on Ni(111)

Electronic structure of Ni(111)

First, results for the image-potential state dynamics on Ni(111) are presented. Before we start the presentation of our 2PPE data, a short description of the surface electronic structure of Ni(111) is given. Fig. 6.1 displays the projected bulk bandstructure along the $\bar{\Gamma}\bar{M}'$ direction of the surface Brillouin zone taken from reference [87]. Electronic states above the upper band-gap edge have *sp* character. Note that the $L_{2'}$ point lies -0.9 eV below the Fermi energy and that the shaded area of up to 0.2 eV at $k_{||} = 0$ above E_F have *d*-band character [88].

The first image-potential state $n = 1$ with a reported binding energy of -0.80 ± 0.03 eV [113] lies approximately 1.6 eV below the upper band-gap edge [88]. The two states labeled S_0 and S_1 have been observed in photoemission- and inverse pho-

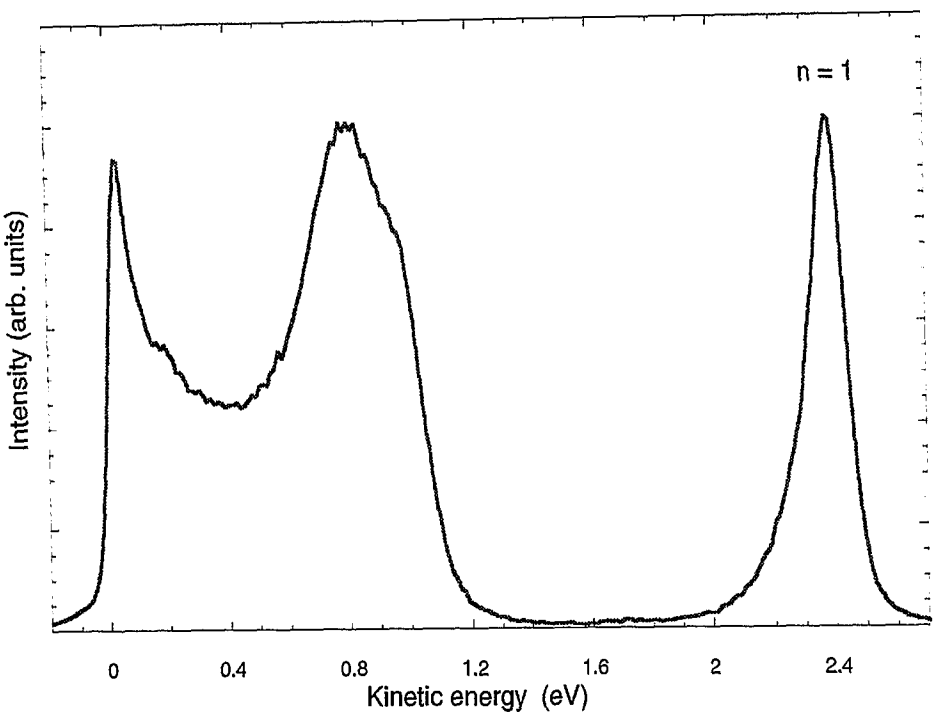

Figure 6.2: Normal emission 2PPE spectrum of Ni(111) recorded at photon energies of 4.71 and 3.14 eV for the pump and probe pulse, respectively. Next to the vacuum cutoff the electronic structure below E_F could be seen at kinetic energies of up to 1.1 eV. The peak at 2.37 eV kinetic energy could be attributed to the first image-potential state.

toemission experiments, respectively [87, 112] and were identified as states with an enhanced wave-function amplitude at the surface. These states are, therefore, expected to have large wave-function overlap with image-potential states. They may significantly contribute to the decay of image states via electron-hole pair production.

To populate the $n = 1$ state we used the third harmonic with a photon energy of 4.71 eV. Unfortunately no higher Rydberg members could be populated due to restrictions of the fundamental wavelength of the Ti:sapphire laser system used in the experiments. Since the $n = 2$ state has a reported binding energy of -0.25 ± 0.05 eV [62] a photon energy close to 5 eV is required which corresponds to a wavelength below 250 nm. On the other hand, the photon energy has to be kept below the work function to avoid space charge effects so that the used photon energy should not exceed a value of about 5.2 eV[1]. The frequency doubled output with a photon

[1]Note that the fourth harmonic $4\hbar\omega$ is only tunable in a range between 5.8 and 6.06 eV.

energy of 3.14 eV was used to probe the population dynamics of the $n = 1$ state. It will be shown later that this photon energy also allows us to monitor the electronic structure below the Fermi energy in situ.

Fig. 6.2 shows a typical 2PPE spectrum recorded in the normal-emission geometry obtained with photon energies of 4.71 and 3.14 eV at zero time delay between pump and probe pulses. The energy scale is referenced to the vacuum level and gives directly the photoelectron kinetic energy[2].

Apart from the vacuum cutoff two main features can be seen below 1.1 eV and at around 2.37 eV kinetic energy. By blocking the 4.71 eV laser pulse, the sharp peak at 2.37 eV vanishes completely while the other part of the spectrum remains unchanged. This part is, therefore, caused by the simultaneous absorption of two 3.14 eV photons within the same laser pulse via nonresonant transitions. It, therefore, monitors the occupied electronic structure below E_F. The relatively sharp structure around 0.8 eV kinetic energy can be assigned to the state labeled S_0 in Fig. 6.1 which has been observed in photoemission measurements [112, 114]. The work function was deduced to be 5.20 ± 0.05 eV from the width of the EDC obtained with the probe pulse only (3.14 eV) in agreement with previously reported values [112, 113]. The peak at 2.37 eV can only be observed if the delay between both pulses is small and is therefore attributed to the excitation of an electron below E_F into the $n = 1$ image-potential state and the subsequent emission by absorbing photons of 4.71 and 3.14 eV, respectively[3].

The binding energy of the $n = 1$ state relative to E_{Vac} can be easily calculated by subtracting the probe-puls photon energy of 3.14 eV from the kinetic-energy position. We obtain a binding energy of -0.77 ± 0.03 eV for the first image-potential state on Ni(111). This result is in agreement within the experimental error with the value of -0.80 ± 0.03 eV reported by the group of Steinmann [62, 113]. The binding energy of the $n = 1$ state depends critically on the surface cleanliness. We observed an increase of the $n = 1$ binding energy with time after the surface preparation cycle which is accompanied by an increase of the work function. Therefore the slightly higher binding energy reported earlier might be a consequence of surface contamination due to longer measuring times. The $n = 1$ peak is slightly asymmetric on its low energy side which has also been observed by Giesen et al. at a comparable photon energy [113]. By increasing the photon energy the peak becomes more and more symmetric. We, therefore, attribute the asymmetry to two-photon absorption from initial states below E_F via a nonresonant transition.

In order to investigate the influence of adsorbates on the image-potential state lifetime, hydrogen was adsorbed on the Ni surface by filling the preparation chamber with H_2 gas. It is known that hydrogen forms a disordered atomic layer on Ni(111) [115] at room temperature.

[2]The bias voltage which has been applied to the sample, has already been substracted.

[3]The simultaneous absorption of two 4.71 eV photons results in an additional $n = 1$ peak at a kinetic energy of 3.94 eV (not shown in the spectrum).

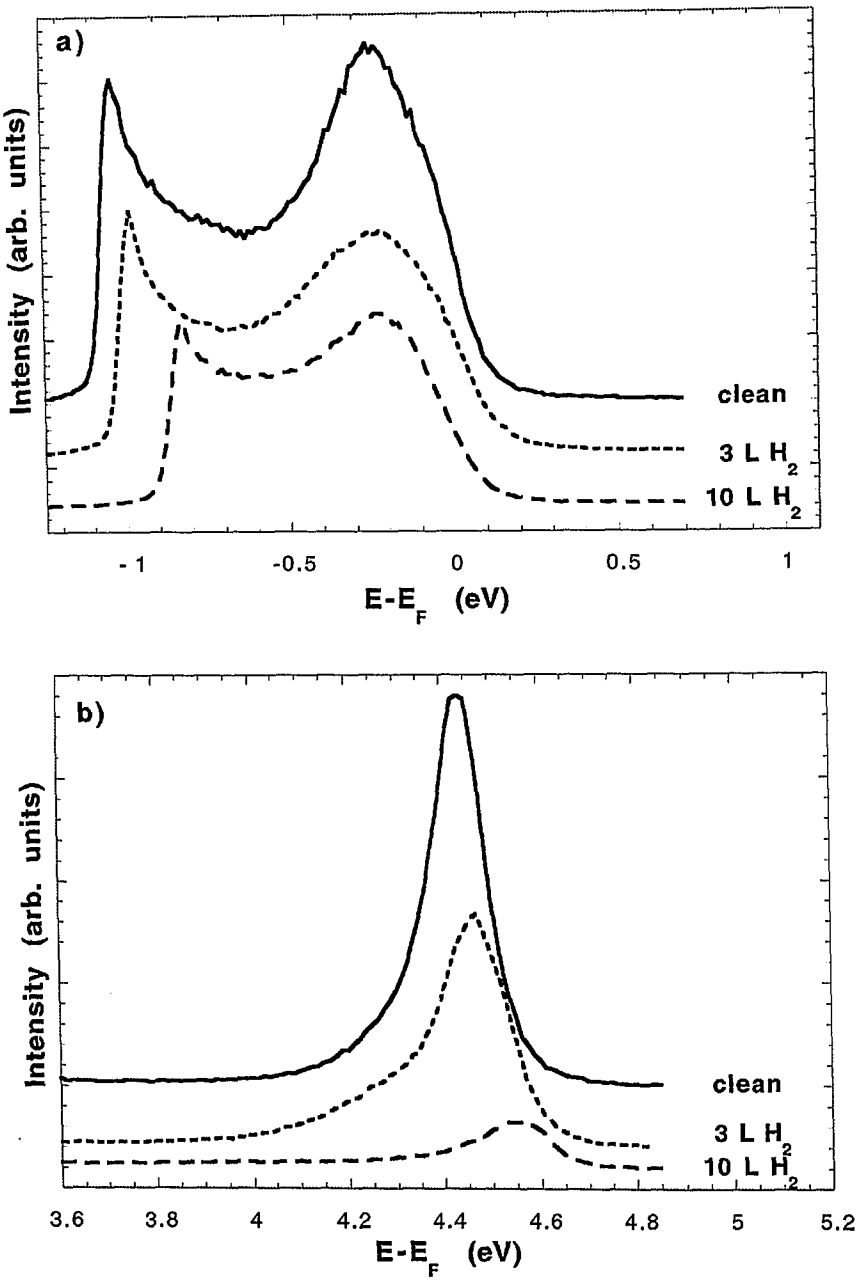

Figure 6.3: 2PPE energy-distribution curves obtained for the clean Ni(111) surface (solid line) and for different hydrogen exposures (dashed lines). **a)** The simultaneous absorption of two 3.14 eV photons causes non-resonant emission from states below E_F. **b)** The energy position of the $n = 1$ image-potential state relative to E_F. With increasing hydrogen exposure the image state shifts to higher energies compared to the initial value of 4.43 eV for the clean surface. (1 L correponds to 10^{-6} mbar s).

The features in the EDC shown in Fig. 6.2 are caused by 2PPE processes with different combinations of photon energies (3.14+3.14 eV, 4.71+3.14 eV). We, therefore, introduce an overall energy scale with respect to E_F as shown in Fig. 6.3 where the photoelectron spectra are separated into two parts. Fig. 6.3a) displays the energy region close to E_F, while Fig. 6.3b) shows the $n = 1$ state. Apart from the EDC obtained from the clean surface (solid lines), Fig. 6.3 also displays EDCs for different hydrogen exposures (dashed lines) up to saturation coverage. As expected, a significant work function change can be observed in Fig. 6.3a) which manifests itself in a shift of the vauum cutoff.

There are clear intensity variations with hydrogen doses up to a saturation exposure of 10L (1L = 10^{-6} mbar s). Especially the feature located 0.25 eV below the Fermi energy is attenuated due to the quenching of the S_0 surface state in agreement with earlier studies by Himpsel et al. [112] who assigned the remaining intensity to a transition from a *d*-like bulk state.

With increasing hydrogen coverage, the binding energy of the $n = 1$ state increases monotonously up to a value of 0.83 ± 0.03 eV. This can be explained by the shift towards the upper band-gap edge which changes the quantum defect a. Since the image-potential states are pinned to the vacuum level, the work-function change leads to a shift of the $n = 1$ state relative to E_F. In addition, a strong attenuation of its intensity is observed. This is mainly caused by the quenching of the occupied S_0 surface state which provides a very efficient excitation channel due to a large wavefunction overlap with the image state [113].

Image-potential state dynamics

In order to measure the lifetime of the $n = 1$ state, the analyzer was set to the $n = 1$ peak position while scanning the pump-probe delay. The instrumental cross-correlation, which serves as reference and determines the time zero in the experiment, was measured below the image-potential state at energies between 2.5 and 2.9 eV above E_F. Hot electron lifetimes which may contribute and could cause deviations from the intrumental cross-correlation can be neglected since those lifetimes at energies > 2 eV above E_F are ($\ll 5fs$) [97].

Fig. 6.4 displays the transient responses of the clean (middle panel, filled circles) and hydrogen covered (top panel, open circles) Ni(111) surface. The instrumental cross-correlation with a full width at half maximum of 120 fs is shown at the bottom (open squares). Assuming a $sech^2$ function to describe the laser pulse shape, we obtained equal durations for pump and probe pulse of 80 fs. The probe-pulse length was measured independently in an autocorrelation setup at the sample for the same intermediate-state energies above E_F. Compared to the instrumental function the finite lifetime of the image state affects mainly the center position of the transient response. Fits to the data (dashed lines) based on a $sech^2$ function result in shifts of the $n = 1$ response of 10 ± 3 and 15 ± 4 fs towards positive delay for the clean and hydrogen saturated Ni(111) surface, respectively. In addition, the curves are

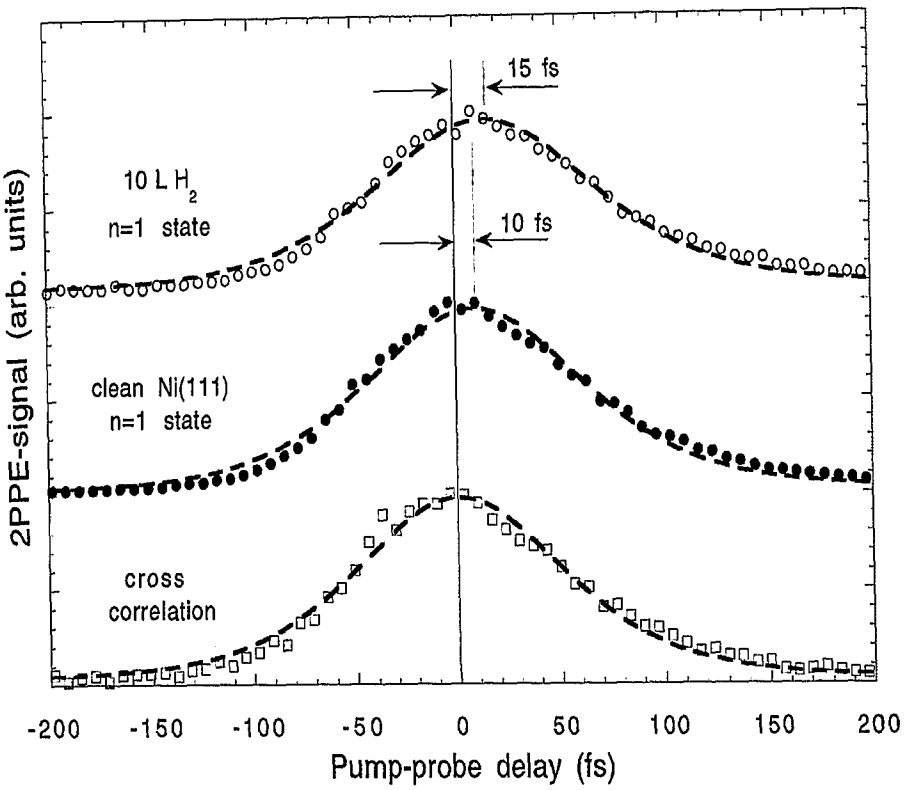

Figure 6.4: Transient responses of the $n = 1$ state for the clean (filled circles, middle panel) and hydrogen saturated (open circles, top panel) Ni(111) surface.The instrumental cross-correlation trace (open squares) with a full width at half maximum of 120 fs is shown at the bottom.

slightly broadened by 4 ± 2 and 7 ± 2 fs, respectively.

In this context it should be mentioned that the apparently small deviations of the transient response from the instrumental cross-correlation require very precise measurements and short pulses. In order to give reliable values for both shift and broadening, the above values given for the clean Ni(111) surface are the result of averaging more than 10 individual lifetime measurements. This included simultaneous measurement of the instrumental function.

In the previous chapter we discussed the theoretical approach using a rate-equation model as suitable method for the interpretation of the observed time response in TR2PPE experiments. The shift towards positive time delay of the image-state response with respect to the instrumental cross-correlation is a sensitive measure for the finite lifetime of this state. Regarding short-lived states with lifetimes much shorter than the pulse durations, the observed shift is approximately proportional to the lifetime [56, 60, 116]. Keeping this in mind we deduce a lifetime

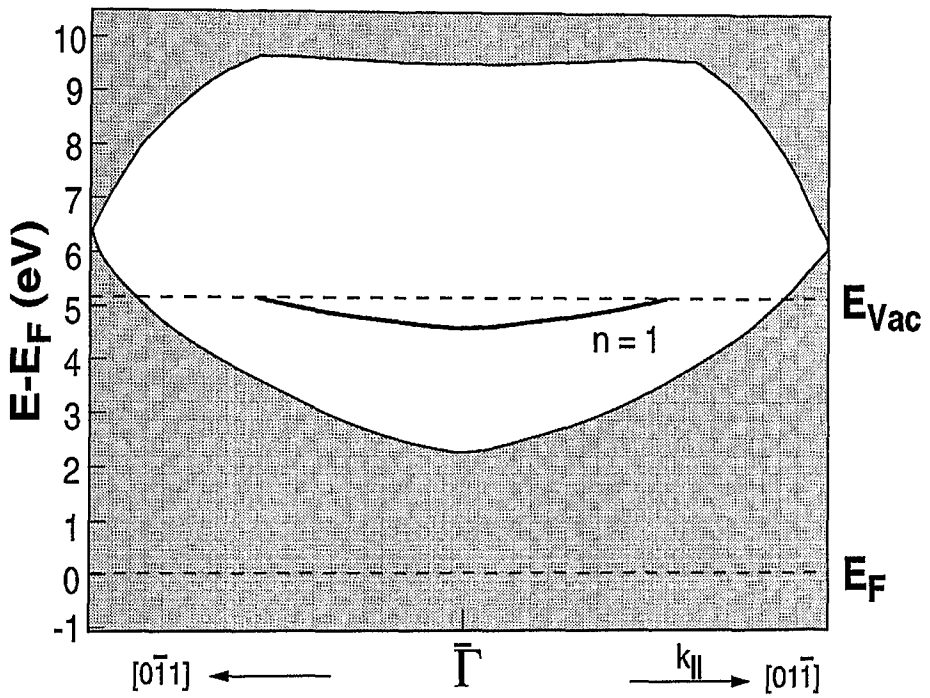

Figure 6.5: Projected band structure of the Ni(100) surface along the $\bar{\Gamma}\bar{X}$ direction [108]. The unshaded area represents a gap in the projected bulk-band structure. The values for the upper and lower band-gap edges are taken from reference [88]. In contrast to the (111) faces of Ni and Pt, the first image-potential state is localized in the lower half of the gap since the work function has a value of around 5.1 eV.

of $\tau^{n=1}_{Ni(111)} = 10 \pm 3$ fs for the $n = 1$ state on clean Ni(111) while the lifetime increases to $\tau = 15 \pm 4$ fs after hydrogen exposure. A description by the rate equation model results in lifetimes of 13 ± 5 fs and 17 ± 6 fs for the clean and hydrogen covered surface, respectively. Thus, both methods give almost identical answers.

6.3 Time-resolved study of the $n = 1$ image-potential state on Ni(100)

Electronic structure and energy-resolved spectra for Ni(100)

In order to illustrate the position of image-potential states inside the gap of the projected bulk-band structure we introduce the Ni(100) surface with a schematic diagram of the surface-electronic structure. Fig. 6.5 sketches the band structure along the $\bar{\Gamma}\bar{X}$ direction of the surface-Brillouin zone, taken from the references [88,

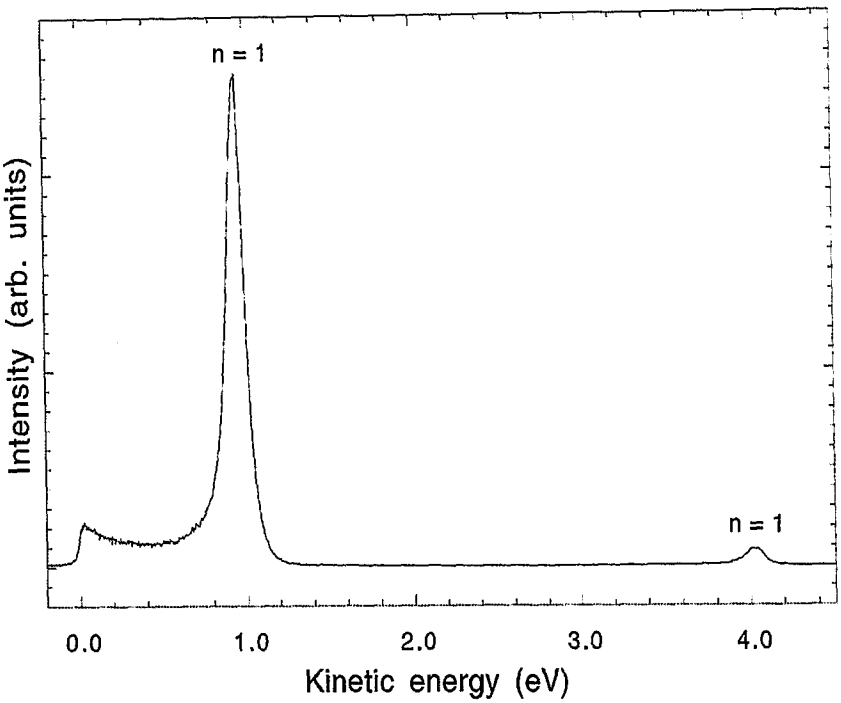

Figure 6.6: 2PPE spectrum recorded at $\Delta t = 0$ of the Ni(100) surface using photon energies of 1.55 and 4.65 eV. Two sharp peaks are resolved at kinetic energies close to 1 and 4 eV. Both peaks result from emission of the $n = 1$ image-potential state.

108]. The upper (X_1) and lower ($X_{4'}$) band-gap edges are localized at 9.4 eV and 2.1 eV above the Fermi energy, respectively. The value of the work function reported in the literature is 5.09 ± 0.03 [61]. This implies that the image-potential states are localized in the lower half of the band gap as shown in Fig. 6.5.

In contrast to the (111) surfaces discussed above, no unoccupied crystal-induced surface states have been reported on Ni(100) near $\bar{\Gamma}$ [108]. The observation of an occupied surface state at $\bar{\Gamma}$ was reported by Erskine [117]. However, this state was neither found in other experiments [118] nor in theoretical calculations [119]. This absence of major decay channels at $\bar{\Gamma}$ is, therefore, expected to cause a longer image-state lifetime. This trend might ever be enhanced by the mid-gap position of the image-potential states which are therefore less strongly hybridized with bulk bands.

In order to populate the first image-potential state on Ni(100), we used the frequency tripled output of the Ti:sapphire system while the fundamental with a photon energy of 1.55 eV was used to probe its occupancy. Similar to the Ni(111) surface, higher members of the Rydberg series could not be populated due to restrictions of the available photon energies. The pulse lengths at the sample of pump and probe pulse were determined to 115 and 70 fs, respectively. Fig. 6.6 depicts

a typical 2PPE spectrum recorded in normal-emission geometry using the time-of flight photoelectron detection technique. The x-axis is referenced to the kinetic energy after substracting an applied bias voltage of -1 eV. The dominant feature in the EDC at a kinetic energy close to 1 eV results from 1.55 eV photoemission of $n = 1$ state electrons. The peak at 4.02 eV kinetic energy corresponds to a resonant 2PPE process via the $n = 1$ state by the simultaneous absorption of two photons from the frequency tripled beam.

We determined the work function to 5.08 ± 0.03 eV and the $n = 1$ binding energy to -0.61 ± 0.02 eV. These values are in excellent agreement with literature values of 5.09 ± 0.03 and -0.61 ± 0.03, respectively [61].

Time-resolved measurements on Ni(100)

The transient response of the image-potential state was measured by recording the 2PPE signal of the $n = 1$ peak obtained with the frequency tripled and fundamental beams as function of the pump-probe pulse delay. Using the time-of flight technique it was possible to monitor the instrumental cross-correlation in situ, that means that both, the transient response of the image-potential state and the instrumental function were obtained in the same measurement cycle. Different cross-correlation curves have been scanned off resonance at different energies far above the Fermi level. They all show an identical lineshape, thus we can rule out lifetime contributions of hot electrons within the accuracy of the experiment.

The results are shown in Fig. 6.7. A fit (dashed lines) to the recorded instrumental cross-correlation (open squares, bottom panel) based on a $sech^2$ function yields a full width at half maximum of 138 fs. The maximum of the transient response of the image-potential state (top panel, filled circles) is shifted 13 fs towards positive time delay. In addition, the curve is slightly broadened by 6 fs. As described in the last section this gives an image-potential state lifetime of $\tau^{n=1}_{Ni(100)} = 13 \pm 3$ fs. A fit based on the rate-equation model (top panel, solid line) leads to a lifetime of $\tau^{n=1}_{Ni(100)} = 16 \pm 5$ fs. Similar to the case of Ni(111) both methods agree within the experimental error. For simplicity, we will thus make use of the values obtained from the rate-equation model in the following discussion. We also like to mention that the conclusions made in the discussion below are independent of the choice of the model used for the data analysis.

6.4 Discussion

Due to the uncertainty principle the finite image-state lifetime, τ, corresponds to an energy broadening Γ which can be observed in high-resolution 2PPE experiments. However, Γ also contains an additional broadening due to dephasing effects. The two contributions have been separated on Pt(111) (see chapter 5) and the Pd(111) surface [60]. Recent high-resolution 2PPE measurements on Pd(111) [60] observed

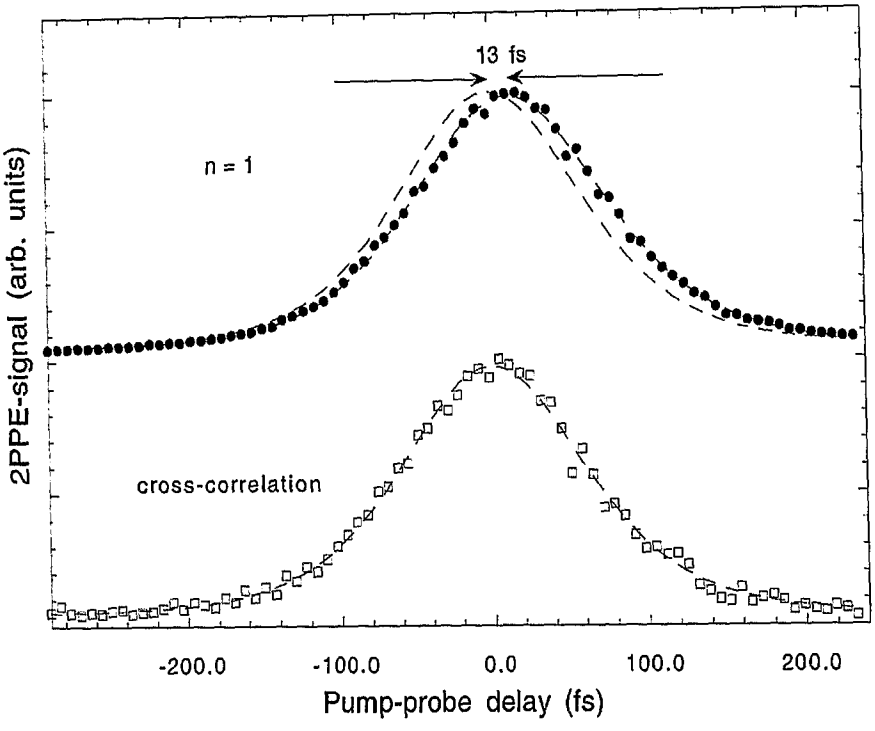

Figure 6.7: Time-resolved spectra obtained on the clean Ni(100) surface. The instrumental cross-correlation trace (bottom panel, open squares) with a full width at half maximum of 138 fs was recorded off resonance of the $n = 1$ image state. The transient response of the first image state is sketched in the top panel (filled circles). Fits to the data (dashed and solid lines) yield a curve shift of 13 fs towards positive pump-probe delay and a broadening of 6 fs for the $n = 1$ response with respect to the instrumental function.

a $n = 1$ state linewidth of 32 ± 4 meV. The linewidth expected from the image-potential state lifetime on Pd(111) of $\tau = 25 \pm 4$ fs measured in the same experiment corresponds to 21 meV. Those differences are assigned to dephasing effects of the image-state electrons.

Our 2PPE studies on Ni(111) and Ni(100) reveal[4] intrinsic linewidths of 81 ± 12 and 66 ± 12 meV for the $n = 1$ states, which corresponds to lifetimes of 8 and 10 fs, respectively. The obtained linewidth values are in excellent agreement with the values of 84 ± 10 and 70 ± 8 meV reported previously for the two surfaces, respectively [61]. Since the lifetimes obtained from the measured intrinsic linewidth on both Ni surfaces are only slightly shorter than those measured with TR2PPE, dephasing effects are smaller than on Pd(111) and Pt(111).

[4]The linewidth measurement of the $n = 1$ state on Ni(111) has also been performed with our TOF spectrometer because of the improved energy resolution by a factor of 2.

After hydrogen adsorption, the occupied surface state of Ni(111) 0.25 eV below E_F is quenched which is accompanied by a significant lifetime increase. This change in lifetime may have different reasons. First of all, adsorbed hydrogen atoms may affect the lifetime. Hydrogen is adsorbed unordered on Ni(111) at room temperature and one would therefore argue that hydrogen atoms may act as additional scattering centers for electrons in image states which may shorten the lifetime. In fact, it has been demonstrated that the unordered adsorption of atoms and molecules decreases the lifetime of image states [55].

Second, the image-state position inside the band gap changes due to the work function increase after hydrogen adsorption. However, since the image state on the clean surface is localized above the band-gap center, the work-function increase leads to a shift away from the center towards the upper band-gap edge. This in turn should lead to a stronger damping of the wave function which in turn would also decrease the lifetime [120].

On the contrary, the observed lifetime after hydrogen adsorption increases. Among all electronic states, surface states can be expected to have the largest wave-function ovelap with image-states due to their localization at the surface. As depicted in Fig. 6.1, two surface states have been observed on the Ni(111) surface which therefore may contribute to the decay of the $n = 1$ state. Therefore we attribute the lifetime increase to the quenching of the occupied surface state[5] which no longer can contribute to the population decay of the image-state.

Nevertheless, even after hydrogen adsorption the lifetime is still short and is comparable to that of the $n = 1$ state on Ni(100), where no surface states are observed at $\bar{\Gamma}$. Both lifetimes obtained for the $n = 1$ states are significantly shorter compared to those obtained on other surfaces[6] with the only exception of the $n = 1$ state on Cu(111) [23, 56, 103], which is only slightly larger. Hence the general trend for both Ni surfaces can only be explained by another mechanism to be involved which is responsible for the shortened lifetimes on those surfaces. Since image states decay via the creation of electron-hole pairs, states below and above the Fermi energy have to be taken into account.

In contrast to the noble metals, in the case of Ni the more localized d-bands cross the Fermi level and lead to a large occupied and unoccupied density of states (DOS) around E_F. The enhanced DOS at E_F thus provides a large number of electronic states in k-space which could be involved in the decay process. This so called "phase space argument" has been frequently used to describe the differences of hot-electron dynamics between noble and transition metals [97, 104]. Using TR2PPE, the measured hot-electron lifetimes on the transition-metal surfaces Fe, Co and Ni are at least one order of magnitude shorter than those on the noble metals Cu, Ag and Au [4, 97]. These differences are explained by the enhanced DOS at E_F due to the narrower d-bands in transition metals compared to the sp-derived bands around

[5]Note, that we can not rule out the additional quenching of the unoccupied surface state.

[6]This will also be discussed in chapter 7.

E_F in the noble metals. Thus we can expect a significant contribution of d-bands into the decay of image states which could explain the observed short lifetimes. We come back to this discussion later in chaper 7.

For Fe and Co, the observed large intrinsic linewidths go along with a magnetic exchange splitting of the $n = 1$ states [67]. The exchange splitting of bulk bands leads to slightly different gap edges for majority- and minority-spin bands. Thus, according to equation 3.10 the exchange splitting of image states reflects shifts in binding energy due to different relative positions within the majority and minority band gap. Though an image-state splitting has been theoretically predicted for the Ni(100) and Ni(111) surfaces [106, 111], only upper limits for the splitting have been reported in the literature using 2PPE [61], while the values reported using inverse photoemission are below 20 meV [108, 109]. We also tried to observe such a splitting on Ni. By using s- and p-polarized light, the excitation from different initial states $|i\rangle$ with different symmetries to the image state $|n\rangle$ can be selected. Since only transitions between bands of the same spin orientation have to be considered [110], the population of spin up and spin down components of the image state can be varied by changing the light polarization which leads to a shift of the image-state peak maximum [107]. We didn't observe such a shift in our experiments. Reasonable explanations for that are (i) a very small spin splitting and (ii) the indirect method, which requires a splitting of the initial bands with different symmetries [110].

Therefore we conclude that d-bands, which are also responsible for the magnetic properties of $3d$-transition metals play a significant role in the decay of image-potential states on these surfaces.

Unfortunately, up to now no precise theoretical calculations for image-state lifetimes on Ni surfaces have been reported in the literature. An early calculation performed by S. Gao et al. [121] predicts an 8 times larger linewidth for the $n = 1$ state on Ni(111) compared to Cu(111), which supports the trend observed in TR2PPE experiments. Following our measurements, the group of E.V. Chulkov and P.M. Echenique has just started calculations based on a many-particle formalism. Unfortunately, final values are not available. However, they predict lifetimes between 12 and 18 fs for the $n = 1$ states on Ni(111) and Ni(100) [122], which would be in excellent agreement with our measured values.

6.5 Concluding remarks

In summary, with our experiments we have measured lifetimes of the first image-potential state on the (111) and (100) faces of Ni. We have demonstrated on Ni(111) that surface states indeed serve as efficient decay channels in the relaxation process of image-potential states. Our measurements reveal unusual short lifetimes for the $n = 1$ state on Ni(111) and Ni(100). We attribute the observed short lifetimes to a significant contribution of d-bands to the decay of image-states. According to our conclusion, one therefore would also expect similar short lifetimes on Co and Fe

surfaces. A deeper understanding thus requires additional measurements on those surfaces in combination with an enhanced theoretical approach.

Chapter 7

Comparison of image-state lifetimes on different surfaces: dependence on the electronic structure

It is the purpose of this chapter to identify the microscopic mechanisms able to reproduce the trend of the observed lifetimes for the $n = 1$ states on different metal surfaces.

From Ni to Cu, the bandstructure is filled with electrons and the d-bands become occupied. As has been shown on Pt(111)-p(2x2)-O, the density of states near E_F plays an important role in the decay of the image-state population. Therefore, the large density of states around E_F on transition-metal surfaces has to be taken into account.

On the other hand, the energy position of the image-state inside the band gap governs its wave-function damping into the bulk. The damping affects the overlap with bulk bands and, hence, the lifetime of image-potential states.

By taking into account the wave-function damping and the involved electronic states , it can be expected that the decay of electrons populating image states might change in a systematic way for different surfaces.

This chapter is arranged in the following way. We first estimate the damping of the image-state wave functions in dependence of the energy position inside the band gap and compare the damping with the measured lifetimes. In a second step the contributions of the density of states around E_F to the decay are discussed. Finally, both aspects are combined to model the trend observed for image-state lifetimes on different surfaces.

Before we start the discussion, we summarize measured lifetimes of image-potential states up to the $n = 3$ state. Table 7.1 shows a compilation of image-state lifetimes on a number of different surfaces obtained with TR2PPE. The calculated theoretical values are added for comparison. We would like to mention early TR2PPE measure-

surface	$\tau_{n=1}$ (fs)	$\tau_{n=2}$ (fs)	$\tau_{n=3}$ (fs)	method	reference
Cu(100)	40 ± 6	120 ± 15	300 ± 20	TR2PPE	[23]
	38 ± 7	110 ± 18	295 ± 25	TR2PPE	this work
	30	132	367	theory	[77]
Cu(111)	18 ± 5	17 ± 5	-	TR2PPE	[56]
	17.5	-	-	theory	[77]
Ag(100)	25 ± 10	180 ± 20	-	TR2PPE	[7, 25]
	55 ± 5	160 ± 10	360 ± 15	TR2PPE	[23]
	26.5	132	-	theory	[102]
Ag(111)	< 20	$< \tau_{n=1}$	-	TR2PPE	[25]
	30 ± 10	-	-	TR2PPE	[103]
	6	-	-	theory	[102]
Pd(111)	25 ± 4	-	-	TR2PPE	[60]
	22	89	-	TR2PPE	[60]
Pt(111)	26 ± 7	62 ± 7	-	TR2PPE	this work
	29	73	-	theory	[122]
Ni(111)	13 ± 5	-	-	TR2PPE	this work
Ni(100)	16 ± 5	-	-	TR2PPE	this work

Table 7.1: Lifetimes of up to the third image state on different surfaces, measured with TR2PPE. Calculated values are also shown for comparison.

ments on Ag surfaces [7, 25]. The authors reported only low count rates and they did not present a precise measurement of the instrumental cross-correlation. This may lead to smaller lifetime values for the $n = 1$ states. Therefore, the recent values of 30 ± 10 [103] and 55 ± 5 fs [23] for the $n = 1$ states on Ag(111) and Ag(100), respectively, seem to be more reliable.

The overlap with bulk bands

The energy position of an image-potential state inside the band gap of the projected bulk-band structure affects the penetration of its wave function into the crystal [77, 120]. If the image state is localized near the band-gap center, its wave function is strongly damped inside the crystal. On the other hand, if the image state lies close to the band-gap edge, the penetration of the wave function is larger and the maximum of the probability density is shifted towards the crystal surface. Hence, the lifetime of image-potential states located close to the band-gap edge should be reduced. In order to visualize that the mid-gap energy position of an image-potential state should imply longer lifetimes compared to a position close to the band-gap edge, one can estimate the damping of the image-state wave function inside the crystal.

A convenient way of considering the two-dimensional band structure of solids

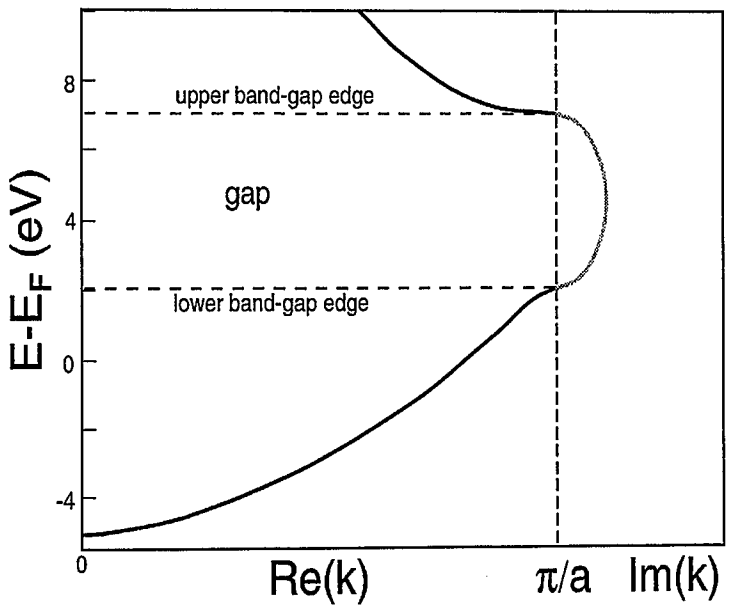

Figure 7.1: Complex band structure obtained using the approximation of the one-dimensional nearly free electron model. Within the gap, which has opened at the zone boundary, only at the surface solutions with real E and complex wave vectors $k = p + iq$ are possible.

starts with the approximation of the nearly-free electron two-band model [123]. This model has been frequently applied for the calculation of image-potential states [46, 124].

Within this model only electronic states perpendicular to the surface (z-direction) are considered. The problem is, therefore, only one dimensional. One obtains a complex band structure $E(k)$ as depicted in Fig. 7.1. In this figure, k and a denote the wave vector and the lattice constant, respectively. At the zone boundary $\frac{\pi}{a}$ a gap opens. Solutions for the Schrödinger equation within this gap do not exist in the bulk. Only at the surface, solutions with real E and complex $k = p + iq$ are still possible. Their wave functions exponentially decay away from the surface into the bulk. The imaginary part q of the wave vector, which describes the damping, reaches its maximum at the gap center and decreases to zero at the gap edges. The overlap between the image-state wave functions and bulk bands is proportional to $\frac{1}{q}$. A large imaginary part, therefore, results in a strong wave-function damping which should enhance the lifetime of the corresponding state.

In the two-band approximation eigenstates with

$$\Psi_{k,E}(z) = A\exp(ikz) + B\exp(i(k-g)z) \tag{7.1}$$

are viewed. $g = \frac{2\pi}{a}$ is the reciprocal lattice vector in one dimension. The electron energies can be calculated by solving [123]

$$det \begin{pmatrix} \epsilon_k - E & U \\ U & \epsilon_{k-g} - E \end{pmatrix} = 0 \tag{7.2}$$

where U denotes the potential Fourier coefficient for g. $\epsilon_k = \frac{(\hbar k)^2}{2m}$ describes the energy of an electron with given k.

We now turn our attention to the direction perpendicular to the surface. In this case g is along the surface normal. The evaluation of equation 7.2 yield the standard result

$$E = \pm\sqrt{U^2 + \frac{1}{4}(\epsilon_k - \epsilon_{k-g})^2} + \frac{1}{2}(\epsilon_k + \epsilon_{k-g}) \quad . \tag{7.3}$$

One obtains the energy at the bottom of the valence band for $k = 0$, while at the zone boundary ($k = \frac{g}{2} = \frac{\pi}{a}$) a gap of magnitude $2|U|$ opens. As mentioned above, within the gap solutions with real E and complex wave vectors $k = p + iq$ are still possible. The wave function of such a solution exponentially decays into the crystal and can be written as

$$\Psi_{k,E}(z) \propto \exp(-qz)\sin(\frac{g}{2}z + \delta) \quad . \tag{7.4}$$

In our case, E denotes the energy position of the image-potential state. Using equation 7.3 one finally obtains an expression for q:

$$q^2 = (\sqrt{U^2 + 4\epsilon_g E} - (\epsilon_g E)) \cdot \frac{2m}{\hbar^2} \tag{7.5}$$

with

$$\epsilon_g = \frac{(\hbar g)^2}{8m} \quad . \tag{7.6}$$

Despite of the simplicity of the used model it is capable to give a rough overview for the estimated damping of the wave-function with respect to the energy position within the band gap.

The calculated results for a number of $n = 1$ states on different surfaces are plotted against the observed lifetimes measured with TR2PPE in Fig. 7.2. The data for the upper and lower band-gap edges used within the calculation are taken from the references [65, 88, 125, 126]. As mentioned above, recent lifetime values for Ag [23, 103] are more reliable compared to those reported in the references [7, 25]. We, therefore, use only the data published by Shumay et al. [23] and McNeill et al. [103].

In the case of Cu(111), temperature dependent lifetime measurements for the $n = 1$ state have been reported [65]. The lifetime ranges from 22 ± 3 fs at 25 K to 14 ± 3 fs at 350 K. This dependence can be explained by a shift of the upper band-gap edge towards E_F with increasing temperature. Since the $n = 1$ state

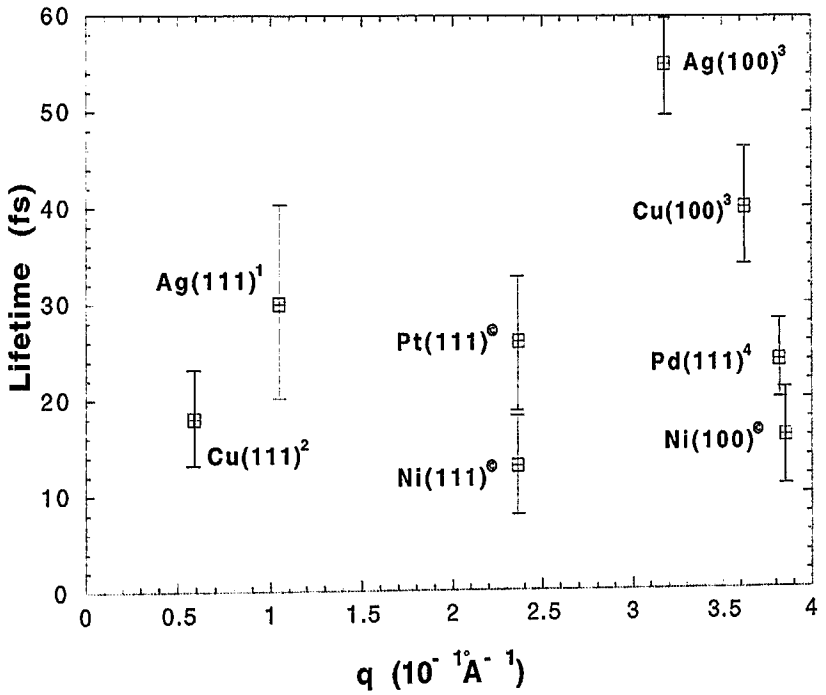

Figure 7.2: Liftetimes of $n = 1$ image-states measured with TR2PPE plotted against the estimated imaginary part q of the wave function. A general behaviour can not be observed especially with regard to the transition metals Ni and Pd. However, the differences observed between the (100) and (111) faces of Cu, Ag and Ni demonstrate the trend that an increase in q leads to longer image-state lifetimes. [1] J.D. McNeill et al. [103], [2] M. Wolf et al. [56], [3] I.L. Shumay et al. [23], [4] A. Schäfer et al. [60], © this work.

on Cu(111) is localized close to the upper band-gap edge, the damping of its wave function inside the crystal is highly sensitive upon the energy position with respect to the gap edge as can be inferred from Fig. 7.1. The change of q is large at the gap edges, while it varies only slightly within the gap. Therefore, if the $n = 1$ state is localized close to a gap edge, its lifetime is expected to become sensitive upon temperature variation. The lifetime value used for the $n = 1$ state in Fig. 7.2 was measured at 90 K [56, 65].

Under the assumption that image-potential state lifetimes depend exclusively on the wave-function penetration inside the crystal one should expect an universal curve for all surfaces. Such a general behaviour can not be observed in Fig. 7.2. Even considering the error bars the data scatter significantly. A closer analysis reveals, however, the expected tendency for the (100) and (111) surfaces of Cu, Ag, and Ni. On the (111) surfaces q is significantly smaller compared to the respective (100) faces in accordance with a decreased lifetime.

Due to the near mid-gap positions of the $n = 1$ states on Ni(111) and Ni(100) the estimated q values are large. Nevertheless, the $n = 1$-image states on Pd(111), Ni(111) and Ni(100) possess, despite of large calculated q values, relatively short lifetimes. Concerning the large damping factor specially for Ni(100) and Pd(111), the lifetimes of the $n = 1$ states might be in the range of those obtained on Cu(100) and Ag(100). In contrast, the $n = 1$ lifetimes of $\tau^{n=1}_{Cu(111)} = 18 \pm 5$ and $\tau^{n=1}_{Ag(111)} = 30 \pm 10$ fs are still larger compared to the values for Ni(100).

Consequently, based on the above discussion, the description of the population decay of image-potential states has to include the density of states around E_F. The argument concerning the energy position inside the gap might be useful for image states of different surface orientations of only one material as could be seen on Ag, Cu and Ni. Nevertheless, it is not appropriate for the general description of image-potential state lifetimes. As a consequence, the discussion has to include possible electronic states involved in the decay process.

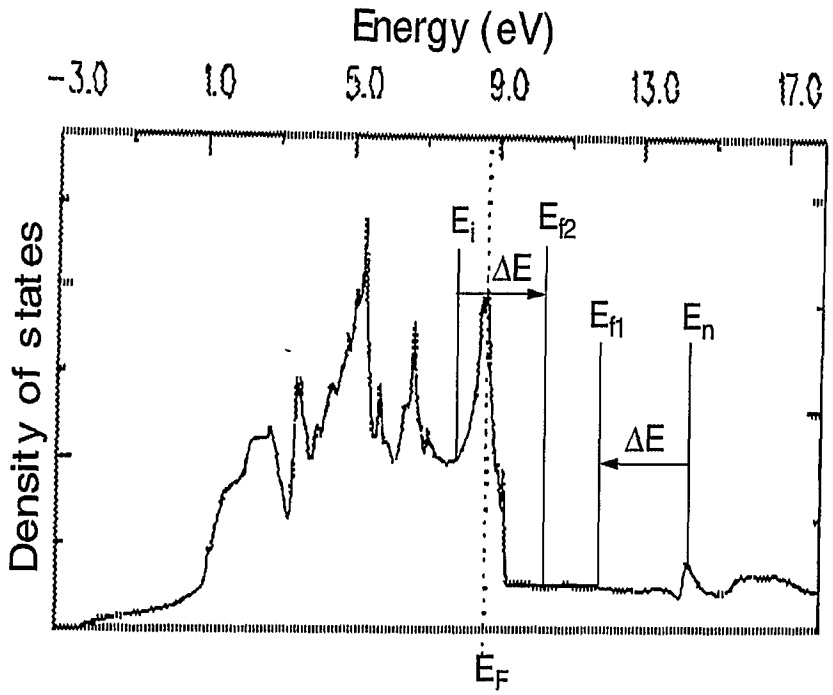

Figure 7.3: Calculated density of states for Pt taken from reference [127]. The population decay of image-potential states is schematically shown. It is mainly determined by electron-hole pair creation and is, thus, affected by the available phase space.

Decay via electron-hole pair creation

The depopulation of image-potential states is governed by the generation of electron-hole pairs. These processes are schematically shown in Fig. 7.3. An electron populating an image state with energy E_n interacts with the Fermi sea. It is scattered into a previously unoccupied state $|E_{f1}\rangle$ with energy E_{f1} above the Fermi energy by simultaneously exciting an electron from the Fermi sea with energy E_i above E_F into a final state with energy E_{f2}.

In the decay process, therefore, all possible interactions of the image-state electrons with the Fermi sea should be taken into account. Within all interactions, the transitions $|E_n\rangle \rightarrow |E_{f1}\rangle$ and $|E_i\rangle \rightarrow |E_{f2}\rangle$ should satisfy energy and momentum conservation. The energy conservation requires $\Delta E = E_n - E_{f1} = E_{f2} - E_i$ where ΔE denotes the energy loss of the electron in the image state. The probability per unit time for such scattering events can then be written as

$$P = \frac{2\pi}{\hbar}|\langle E_{f1}E_{f2}|H_{scatt}|E_nE_{E_i}\rangle|^2\delta((E_n - E_{f1}) - (E_{f2} - E_i)) \quad . \qquad (7.7)$$

H_{scatt} is the perturbation Hamiltonian applicable to the electron-electron scattering process [128]. Note that the state $|E_n\rangle$ exponentially decays into the bulk. Therefore, the probability P depends on the imaginary part q of the wave vector of the image state.

The number of all possible transitions is governed by the density of states ρ of initial and final states $|E_i\rangle$ and $|E_{f1,2}\rangle$, respectively. To account for the available "phase space", one should first integrate over all possible transitions $|E_i\rangle \rightarrow |E_{f2}\rangle$ at given $\Delta E \in [0, E_n - E_F]$. Starting with the assumption that states with *s*,*p*, and *d*-character are involved, four possible processes contribute to the integral if we combine *s* and *p* states:

$$|E_i^{sp}\rangle \rightarrow |E_{f2}^{sp}\rangle \tag{7.8}$$
$$|E_i^{sp}\rangle \rightarrow |E_{f2}^{d}\rangle \tag{7.9}$$
$$|E_i^{d}\rangle \rightarrow |E_{f2}^{sp}\rangle \tag{7.10}$$
$$|E_i^{d}\rangle \rightarrow |E_{fs}^{d}\rangle \tag{7.11}$$

In a second step, a convolution of this integral with all possible final states $|E_{f1}\rangle$ should be integrated over ΔE. Accounting again for *sp*- and *d*-states, there are two possibilities for transitions of an image-potential state electron:

$$|E_n\rangle \rightarrow |E_{f1}^{sp}\rangle \tag{7.12}$$
$$|E_n\rangle \rightarrow |E_{f1}^{d}\rangle \tag{7.13}$$

The result of this calculation is then inversely proportional to the lifetime τ:

$$\frac{1}{\tau} \propto \mathrm{S} = \int_0^{E_n - E_F} d(\Delta E) \quad \rho(E_n - \Delta E) \int_{E_F - \Delta E}^{E_F} dE_i \quad \rho(E_i)\rho(E_i + \Delta E) \quad . \tag{7.14}$$

Noble metals have no *d*-holes. Hence, the processes 7.9, 7.11, and 7.13 can not occur. Since the *d*-bands of Ag lie energetically lower with respect to E_F compared with Cu, the contribution of process 7.10 might be smaller. Based on this argument, the image states on Ag are expected to live longer. This has indeed been observed on the (100) and (111) surfaces of Ag and Cu as shown in table 7.1.

The existence of *d*-holes in transition metals provide additional decay channels involving the processes 7.9, 7.11, and 7.13. According to equation 7.14, this should lead to larger calculated inverse lifetimes. Hence, one can expect that the lifetimes of image states on these surfaces are reduced. Following our results on Ni and Pt, this trend can be observed. The $n = 1$ lifetime on Pd(111), reported recently by Schäfer et al. [60], supports this view. Since on the Ni surfaces the $n = 1$ state lifetimes are the shortest observed with TR2PPE, the *d*-band contribution to the decay must be larger compared with Pd and Pt.

In order to calculate the "phace-space factors" S for the population decay of image-potential states on various surfaces according to equation 7.14, we used the

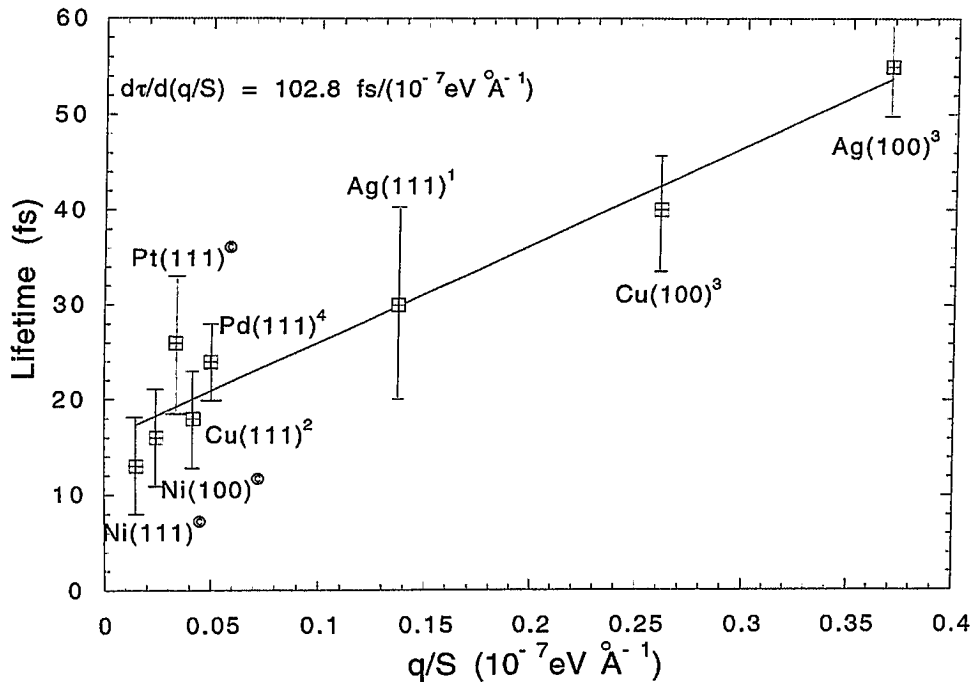

Figure 7.4: Liftetimes of $n = 1$ image-states measured with TR2PPE plotted against $q \cdot \frac{1}{\mathbf{S}}$. A general behaviour can clearly be observed. The solid line is a linear least-square fit to the data. The trend of the curve manifests the influence of d-bands to the population decay. Therefore, the short lifetimes measured on Ni can be explained by a large contribution of d-states to the decay. [1] J.D. McNeill et al. [103], [2] M. Wolf et al. [56], [3] I.L. Shumay et al. [23], [4] A. Schäfer et al. [60], © this work.

calculated density of states for the respective elements from reference [127]. The calculation indeed demonstrates that $\mathbf{S}$ is largest for Ni and smallest for Ag: $\mathbf{S}_{Ni} \approx 20 \cdot \mathbf{S}_{Ag}$. From Ag to Cu, $\mathbf{S}$ increases by a factor of almost 2, while $\mathbf{S}_{Pt,Pd} \approx 10 \cdot \mathbf{S}_{Ag}$. Note that, the higher the factor $\mathbf{S}$, the shorter is the expected lifetime τ of an image-potential state.

A combination of this "phase-space" argument with the estimated values for q, which describe the damping of the image-state wave function, seems to be very promising to result in an universal and simple description of image-state lifetimes on different surfaces. According to equation 7.7, the damping of the image-potential state wave function mediates the strength of the scattering probability per unit time. Thus, the product of the imaginary part q and the reciprocal of the phase-space factor $\mathbf{S}$ should be a qualitative measure for the lifetime of an image-potential state.

The lifetimes τ for a variety of $n = 1$ states are plotted against the product $q \cdot \frac{1}{\mathbf{S}}$

in Fig. 7.4. The solid line is a linear least square fit to the data. Despite of the simplicity of the used model, the linear fit models the data reasonably well.

Hence, the lifetime of an image-state qualitatively is found to depend linear on the product of q and $\frac{1}{\mathbf{S}}$:

$$\tau \propto q \cdot \frac{1}{\mathbf{S}} \quad . \tag{7.15}$$

Our model, in addition, is in excellent agreement with the observed temperature dependent lifetimes[1] measured on Cu(111) [65]. The observed short lifetimes on Ni can, therefore, be explained by the large, partially occupied density of d-states which cross the Fermi level. Moreover, the longer lifetimes on Ag compared to Cu are a consequence of the localization of the d-bands with binding energies below ≈ 3.5 eV with respect to E_F. On Cu, the d-bands start at -2 eV below E_F and give, thus, a larger contribution to the decay than those on Ag.

As mentioned in the previous chapter, recently the phase-space argument has also successfuly been employed for the description of hot-electron dynamics on noble and transition metal surfaces [97, 104].

Therefore, our calculations performed as described above are capable to visualize the lifetimes of image states in dependence of the metal surface in a simple, but elegant way.

[1]The lifetime value for Ag(111) was measured at 40 K. Unfortunately, up to now, temperature dependent measurements for this surface are not available.

Chapter 8

Summary

Within this thesis the optical setup for fs pulses with a large bandwidth - resulting in pulse lengths shorter than 100 fs - has been designed and realized. In addition, a time-of flight electron spectrometer (TOF) has been constructed and used in first experiments. Compared with the previously used hemispherical analyzer, the advantages of the TOF are an improved energy resolution and a substantial reduction of the needed measuring time per photoelectron spectrum.

The population dynamics of image-potential states on clean and adsorbate covered transition-metal surfaces of Pt and Ni[1] have been investigated using time-resolved two-photon photoemission spectroscopy. This has provided useful information on the interaction of excited surface electrons with the underlying substrate. In particular, various decay channels have been separated such as the interaction of image-potential states with d-bands and crystal induced surface states.

On the Pt(111) surface, the first two image-potential states have been resolved exhibiting lifetimes of 26 ± 7 and 62 ± 10 fs, respectively. These values are shorter than the calculated lifetimes for both states, indicating the importance of d-bands which are not included in the calculation. The large lifetime value for the second image state, $\tau_{n=2} > \tau_{n=1}$, is a consequence of a weaker wave-function overlap with bulk bands. This is due to the fact that image states with increasing n are localized further and further in the vacuum. Moreover, its energy position is still located inside the band gap.

The adsorption of oxygen on Pt(111) at room temperature results in a well ordered Pt(111)-p(2x2)-O structure which was observed with LEED. The geometrical rearrangement of the surface causes a change of the electronic structure near the Fermi level. This is accompanied by an observed decrease of the lifetime for both image states by a factor of ≈ 2. The decrease in lifetime was, therefore, addressed to the redistribution of the density of states near the Fermi level. This result demonstrates

[1]It was the purpose of this thesis to measure the first image-potential state on Pd(111), as well. This has been, though, published by the group of Th. Fauster in May 2000 [60].

the importance of inelastic decay channels for the image-potential state lifetime.

On Ni(111) and Ni(100) we found lifetimes shorter than 20 fs for the $n = 1$ states. These lifetimes could not be explained by the overlap with bulk bands only, which is governed by the energy position of the image states inside the band gap. Therefore, we have stressed the importance of d-states to the decay. The lifetimes observed on Ni are, thus, a consequence of the partially filled d-bands, which cross the Fermi level.

For Ni(111), the contribution of the occupied surface state to the image-state population decay has been resolved. After hydrogen adsorption this state was quenched and, thus, an effective decay channel was no longer available. This led to a remarkable lifetime increase of the $n = 1$ state.

A general description of image-potential state lifetimes on different surfaces has been given in chapter 7. Following our TR2PPE results, the model included

- the damping of the wave function inside the crystal which governs the overlap with bulk bands and
- the available phase space which accounts for the possible electronic states involved in the decay.

Although this model is relatively simple, it was found to be capable of describing the trend for image-state lifetimes observed in TR2PPE experiments reasonably well. According to our considerations, the lifetime of an image-potential state is proportional to the imaginary part of its wave vector, which is a measure for the wave-function damping inside the crystal, and inversely proportional to a so called "phase-space factor", which accounts for the available phase space. Due to the simplicity of this approach, the population decay of image states can easily be understood on a phenomenological basis.

This model, therefore, can be used to predict lifetimes of $n = 1$ states on other surfaces including the temperature dependence, as long as they are localized inside a band gap. In addition, within the framework of this model the individual contributions of $s-, p-$, and d-states to the population decay of image-potential states can be calculated.

Appendix A

Optical paths for the different experiments

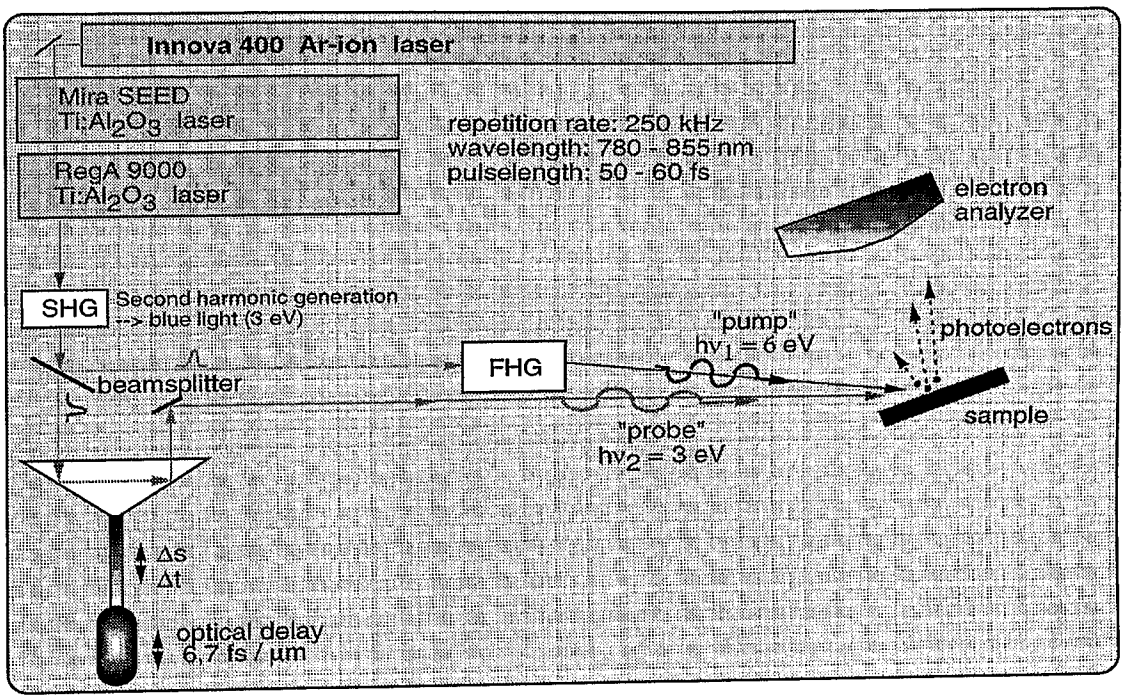

Figure A.1: Experimental setup for the investigation of image-potential states on Pt(111).

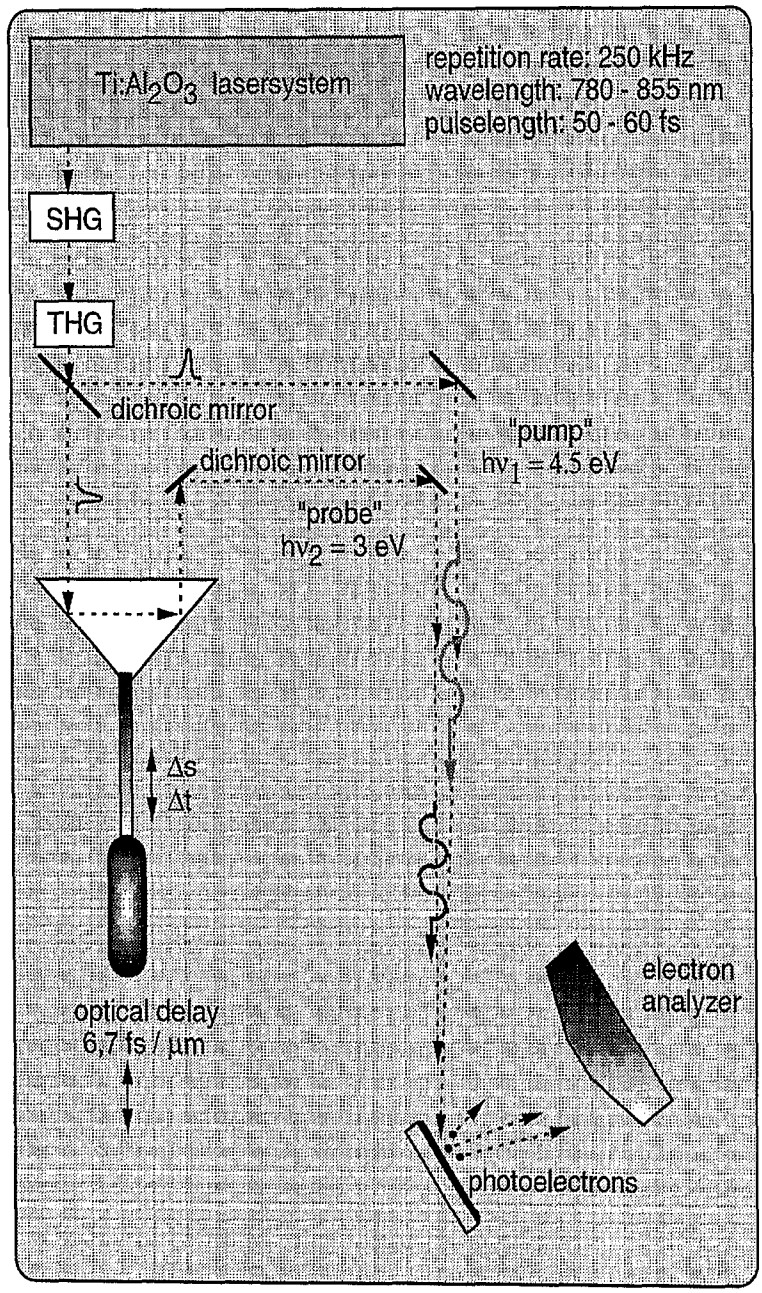

Figure A.2: Experimental setup for the investigation of image-potential states on Ni(111).

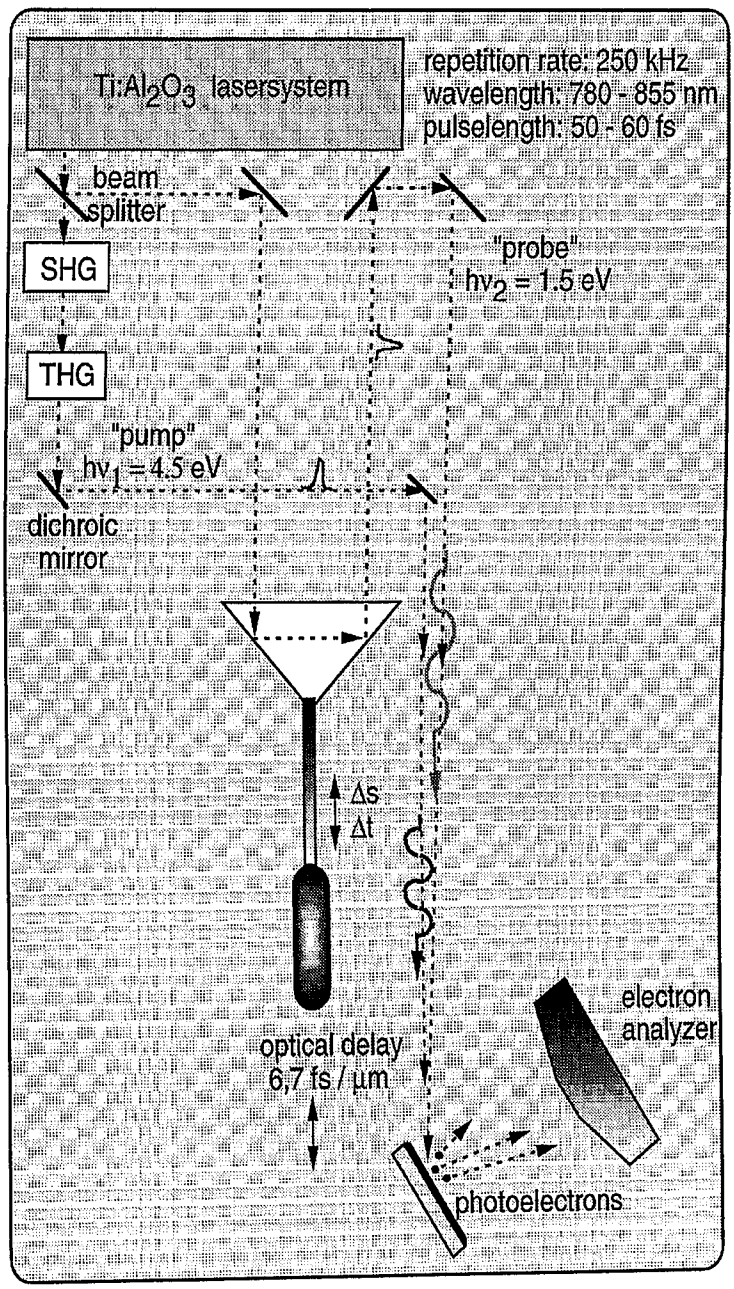

Figure A.3: Experimental setup for the investigation of image-potential states on Ni(100).

Bibliography

[1] R. Haight, Surf. Sci. Rep. **21**, 275 (1995).

[2] H. Petek, M. J. Weida, H. Nagano, and S. Ogawa, Science **288**, 1402 (2000).

[3] T. Baumert, M. Grosser, R. Thalweiser, and G. Gerber, Phys. Rev. Lett. **67**, 3753 (1991).

[4] C. A. Schmuttenmaer, M. Aeschlimann, H. E. Elsayed-Ali, R. J. D. Miller, D. A. Mantell, J. Cao, and Y. Gao, Phys. Rev. B. **50**, 8957 (1994).

[5] M. J. Rosker, M. Dantus, and A. H. Zewail, Science **24**, 1200 (1988).

[6] M. Nisoli, S. Stagira, S. De Silvestri, O. Svelto, S. Sartania, Z. Cheng, M. Lenzner, Ch. Spielmann, and F. Krausz, Appl. Phys. B **65**, 189 (1997).

[7] R. W. Schoenlein, J. G. Fujimoto, G. L. Eesley, and T. W. Capehart, Phys. Rev. Lett. **61**, 2596 (1988).

[8] M. Aeschlimann, M. Bauer, and S. Pawlik, Chem. Phys. **205**, 127 (1996).

[9] S. Ogawa, H. Nagano, H. Petek, and A. P. Heberle, Phys. Rev. Lett. **78**, 1339 (1997).

[10] M. Bonn, S. Funk, Ch. Hess, D. N. Denzler, C. Stampfl, M. Scheffler, M. Wolf, and G. Ertl, Science **285**, 1042 (1999).

[11] M. Aeschlimann, M. Bauer, S. Pawlik, R. Knorren, G. Bouzerar, K. H. Bennemann, Appl. Phys. A **71**, 485 (2000).

[12] R. Jacquemin, S. Kraus, and W. Eberhardt, Solid State Commun. **105**, 449 (1998).

[13] A. Scholl, L. Baumgarten, R. Jacquemin, and W. Eberhardt, Phys. Rev. Lett. **79**, 5146 (1997).

[14] F. Quéré, S. Guizard, P. Martin, G. Petite, O. Gobert, P. Meynadier, and M. Perdrix, Appl. Phys. B **68**, 459 (1999).

[15] M. Bonn, D. N. Denzler, S. Funk, M. Wolf, S. S. Wellershoff, and J. Hohlfeld, Phys. Rev. B. **61**, 1101 (2000).

[16] R. Haight, J. Bokor, J. Stark, R. H. Storz, R. R. Freeman, and P.H. Bucksbaum, Phys. Rev. Lett. **54**, 1302 (1985).

[17] R. Haight and J. A. Silberman, Phys. Rev. Lett. **62**, 815 (1989).

[18] R. G. Tobin, Surf. Sci. **183**, 226 (1987).

[19] W. Wallauer and Th. Fauster, Surf. Sci. **374**, 44 (1997).

[20] Ch. Reuß, I. L. Shumay, U. Thomann, M. Kutschera, M. Weinelt, Th. Fauster, and U. Höfer, Phys. Rev. Lett. **82**, 153 (1999).

[21] E. Knoesel, A. Hotzel, T. Hertel, M. Wolf, and G. Ertl, Surf. Sci. **368**, 76 (1996).

[22] N.-H. Ge, C. M. Wong, R. L. Lingle, Jr., J. D. McNeill, K. J. Gaffney, and C. B. Harris, Science **279**, 202 (1998).

[23] I. L. Shumay, U. Höfer, Ch. Reuß, U. Thomann, W. Wallauer, and Th. Fauster, Phys. Rev. B. **58**, 13974 (1998).

[24] U. Höfer, I. L. Shumay, Ch. Reuß, U. Thomann, W. Wallauer, and Th. Fauster, Science **277**, 1480 (1997).

[25] R. W. Schoenlein, J. G. Fujimoto, G. L. Eesley, and T. W. Capehart, Phys. Rev. B. **43**, 4688 (1991).

[26] M. Weinelt, Ch. Reuß, M. Kutschera, U. Thomann, I. L. Shumay, Th. Fauster, U. Höfer, F. Theilmann, and A. Goldmann, Appl. Phys. B **68**, 377 (1999).

[27] H. Hertz, Ann. Physik **31**, 983 (1887).

[28] J. J. Thompson, Phil. Mag. **44**, 293 (1897).

[29] P. Lenard, Ann. Physik **2**, 359 (1900).

[30] A. Einstein, Ann. Physik **17**, 132 (1905).

[31] E. W. Plummer, and W. Eberhardt, *Angle-Resolved Photoemission as a Tool for the Study of Surfaces*, in *Advances in Chemical Physics*, **Vol. XLIX**, ed. by I. Prigogine and S. A. Rice, Wiley, New York (1982).

[32] V. Dose, Surf. Sci. Rep. **5**, 337 (1985).

[33] R. Jacquemin, *Experimental Setup for Time-Resolved Photoelectron Spectroscopy*, Diplomarbeit, Universität zu Köln (1993).

[34] D. R. Penn, Phys. Rev. B. **13,** 5248 (1976).

[35] T. N. Rhodin and J. W. Gadzuk, in *The Nature of the Surface Chemical Bonds*, ed. by Rhodin and Ertl, Amsterdam, North Holland (1979).

[36] F. Reinert, G. Nicolay, S. Schmidt, D. Ehm, and S. Hüfner, Phys. Rev. B. **63,** 115415 (2001).

[37] J. Kliewer, R. Berndt, E. V. Chulkov, V. M. Silkin, P. M. Echenique, and S. Crampin, Science **288,** 1399 (2000).

[38] J. Shah, *Ultrafast Luminescence Studies of Carrier Relaxation and Tunneling in Semiconductor Nanostructures*, in *Hot Carriers in Semiconductor Nanostructures: Physics and Applications*, ed. by J. Shah, Academic Press, Boston (1992).

[39] T. Hertel, E. Knoesel, M. Wolf, and G. Ertl, Phys. Rev. B. **76,** 535 (1996).

[40] I.E. Tamm, Z. Phys. **76**, 849 (1932).

[41] W. Shockley, Phys. Rev. **56**, 317 (1939).

[42] S. Hüfner, *Photoelectron Spectroscopy*, Springer Ser. Solid-State Sci., Vol. **82** (Springer-Verlag, Berlin, 1995).

[43] W. Eberhardt, *Bandstrukturbestimmung von Festkörpern mit winkelaufgelöster Photoemission und Synchrotronstrahlung*, in *23. IFF-Ferienkurs der KFA-Jülich*, ed. by W. Eberhardt and W. Schilling (1992).

[44] M. Cole and M. H. Cohen, Phys. Rev. Lett. **23,** 1238 (1969).

[45] P. M. Echenique and J. B. Pendry, J. Phys. C **11**, 2065 (1978).

[46] N. V. Smith, Phys. Rev. B. **32,** 3549 (1985).

[47] W. Steinmann, Appl. Phys. A **49,** 365 (1989).

[48] E. G. McRae, Rev. Mod. Phys. **51**, 541 (1979).

[49] E. G. McRae and M. L. Kane, Surf. Sci. **108,** 435 (1981).

[50] Th. Fauster, Appl. Phys. A **59,** 479 (1994).

[51] P. D. Johnson and N. V. Smith, Phys. Rev. B. **27,** 2527 (1983).

[52] D. Straub and F. J. Himpsel, Phys. Rev. Lett. **52,** 1922 (1984).

[53] V. Dose, W. Altmann, A. Goldmann, U. Kolac, and J. Rogozik, Phys. Rev. Lett. **52,** 1919 (1984).

[54] K. Giesen, F. Hage, F. J. Himpsel, H. J. Riess, and W. Steinmann, Phys. Rev. Lett. **55**, 300 (1985).

[55] S. Schuppler, N. Fischer, Th. Fauster, and W. Steinmann, Appl. Phys. A **51**, 322 (1990).

[56] M. Wolf, E. Knoesel, and T. Hertel, Phys. Rev. B. **54**, R5295 (1996).

[57] D. F. Padowitz, W. R. Merry, R. E. Jordan, and C. B. Harris, Phys. Rev. Lett. **69**, 3583 (1992).

[58] Ch. Reuß, Diplomarbeit, Universität München (1994).

[59] R. Fischer, S. Schuppler, N. Fischer, Th. Fauster, and W. Steinmann, Phys. Rev. Lett. **70**, 654 (1993).

[60] A. Schäfer, I. L. Shumay, M. Wiets, M. Weinelt, Th. Fauster, E. V. Chulkov, V. M. Silkin, and P. M. Echenique, Phys. Rev. B. **61**, 13159 (2000).

[61] S. Schuppler, N. Fischer, Th. Fauster, and W. Steinmann, Phys. Rev. B. **46**, 13539 (1992).

[62] S. Schuppler, N. Fischer, W. Steinmann, R. Schneider, and E. Bertel, Phys. Rev. B. **42**, 9403 (1990).

[63] K. Giesen, F. Hage, F. J. Himpsel, H. J. Riess, W. Steinmann, and N. V. Smith, Phys. Rev. B. **35**, 975 (1987).

[64] P. M. Echenique, F. Flores, and F. Sols, Phys. Rev. Lett. **55**, 2348 (1985).

[65] E. Knoesel, A. Hotzel, and M. Wolf, J. Electron Spectrosc. Relat. Phenom. **88-91**, 577 (1998).

[66] R. Fischer, Dissertation, Universität München (1993).

[67] R. Fischer, N. Fischer, S. Schuppler, Th. Fauster, and F. J. Himpsel, Phys. Rev. B. **46**, 9691 (1992).

[68] Mira Model Seed, *Operator's manual*, COHERENT Laser Group, Santa Clara, CA 95054 (1999).

[69] P.S. Bechthold, *Ultrashort Light Pulses: Generation, Handling, Detection*, in *31. Ferienkurs des Instituts für Festkörperforschung des Forschungszentrums Jülich*, ed. by Th. Brückel and W. Eberhardt (2000).

[70] Zs. Bor, and B. Rasz, Opt. Commun. **54**, 165 (1985).

[71] A Nebel, and R. Beigang, Opt. Lett. **16**, 1729 (1991).

[72] E. Knoesel, T. Hertel, M. Wolf, and G. Ertl, Chem. Phys. Lett. **240**, 409 (1995).

[73] K. Giesen, F. Hage, F. J. Himpsel, H. J. Riess, and W. Steinmann, Phys. Rev. B. **35**, 971 (1987).

[74] J. Bokor, R. Storz, R. R. Freeman, and P. H. Bucksbaum, Phys. Rev. Lett. **57**, 881 (1986).

[75] S. Völkening, K. Bedürftig, K. Jacobi, J. Wintterlin, and G. Ertl, Phys. Rev. Lett. **83**, 2672 (1999).

[76] V. P. Zhdanov and B. Kasemo, Surf. Sci. **415**, 403 (1998).

[77] E. V. Chulkov, I. Sarría, V. M. Silkin, J. M. Pitarke, and P. M. Echenique, Phys. Rev. Lett. **80**, 4947 (1998).

[78] P. M. Echenique, J. M. Pitarke, E. V. Chulkov, and A Rubio, Chem. Phys. **251**, 1 (2000).

[79] G. Bihlmayer and S. Blügel, private communication.

[80] W. Eberhardt, F. Greuter, and E. W. Plummer, Phys. Rev. Lett. **46**, 1085 (1981).

[81] N. Memmel and E. Bertel, Phys. Rev. Lett. **75**, 485 (1995).

[82] P. Roos, E. Bertel, and K. D. Rendulic, Chem. Phys. Lett. **232**, 537 (1995).

[83] R. Drube, V. Dose, and A. Goldmann, Surf. Sci. **197**, 317 (1988).

[84] B. E. Nieuwenhuys and W. H. M. Sachtler, Surf. Sci. **34**, 317 (1973).

[85] I. Kinoshita, T. Anazawa, and Y. Matsumoto, Chem. Phys. Lett. **259**, 445 (1996).

[86] D. Straub and F. J. Himpsel, Phys. Rev. B. **33**, 2256 (1986).

[87] A. Goldmann, V. Dose, and G. Borstel, Phys. Rev. B. **32**, 1971 (1985).

[88] N. V. Smith, C. T. Chen, and M. Weinert, Phys. Rev. B. **40**, 7565 (1989).

[89] T. Hertel, E. Knoesel, A. Hotzel, M. Wolf, and G. Ertl, J. Vac. Sci. Technol. A **15**, 1503 (1997).

[90] V. P. Chebotayev, in *High Resolution Laser Spectroscopy*, ed. by K. Shimoda (Springer-Verlag, Berlin, 1976).

[91] R. Loudon, *The Quantum Theory of Light*, Oxford University Press, New York (1983).

[92] M. Wolf, A. Hotzel, E. Knoesel, and D. Velic, Phys. Rev. B. **59**, 5926 (1999).

[93] A. Hotzel, Dissertation, Freie Universität Berlin (1999).

[94] W. Nessler, S. Ogawa, H. Nagano, H. Petek, J. Shimoyama, Y. Nakayama, and K. Kishio, J. Electron Spectrosc. Relat. Phenom. **88-91**, 495 (1998).

[95] U. Höfer, Appl. Phys. B **68**, 383 (1999).

[96] D. Velic, A. Hotzel, M. Wolf, and G. Ertl, J. Chem. Phys. **109**, 9155 (1998).

[97] R. Knorren, K. H. Bennemann, R. Burgermeister, and M. Aeschlimann, Phys. Rev. B. **61**, 9427 (2000).

[98] G. N. Derry and P. N. Ross, J. Chem. Phys. **82**, 2772 (1985).

[99] D. H. Parker, M. E. Bartram, and. B. E. Koel, Surf. Sci. **217**, 489 (1989).

[100] N. Materer, U. Starke, A. Barbieri, R. Döll, K. Heinz, M. A. Van Hove, and G. A. Somorjai, Surf. Sci. **325**, 207 (1995).

[101] M. Lynch and P. Hu, Surf. Sci. **458**, 1 (2000).

[102] E. V. Chulkov, V. M. Silkin, and P. M. Echenique, Surf. Sci. **391**, L1217 (1997).

[103] J. D. McNeill, R. L. Lingle Jr., N.-H. Ge, C. M. Wong, R. E. Jordan, and C. B. Harris, Phys. Rev. Lett. **79**, 4645 (1997).

[104] M. Aeschlimann, M. Bauer, S. Pawlik, W. Weber, R. Burgermeister, D. Oberli, and H. C. Siegmann, Phys. Rev. Lett. **79**, 5158 (1997).

[105] M. Aeschlimann, R. Burgermeister, S. Pawlik, M. Bauer, D. Oberli, and W. Weber, J. Electron Spectrosc. Relat. Phenom. **88-91**, 179 (1998).

[106] M. Nekovee and J. E. Inglesfield, Progr. Surf. Sci. **50**, 149 (1995).

[107] W. Wallauer and Th. Fauster, Phys. Rev. B. **54**, 5086 (1996).

[108] K. Starke, K. Ertl, and V. Dose, Phys. Rev. B. **45**, 6154 (1992).

[109] F. Passek and M. Donath, Phys. Rev. Lett. **69**, 1101 (1992).

[110] U. Thomann, Ch. Reuß, Th. Fauster, F. Passek, and M. Donath, Phys. Rev. B. **61**, 16163 (2000).

[111] R. Schneider, K. Starke, K. Ertl, M. Donath, V. Dose, J. Braun, M. Graß, and G. Borstel, J. Phys. Condens. Matter 4, 4293 (1992).

[112] F. J. Himpsel, J. A. Knapp, and D. E. Eastman, Phys. Rev. B. **19**, 2872 (1979).

[113] K. Giesen, F. Hage, F. J. Himpsel, H. J. Riess, and W. Steinmann, Phys. Rev. B. **33**, 5241 (1986).

[114] F. J. Himpsel and D. E. Eastman, Phys. Rev. Lett. **41**, 507 (1978).

[115] J. Behm, K. Christmann, and G. Ertl, Solid State Commun. **25**, 763 (1978).

[116] Th. Fauster, private communication.

[117] J. L. Erskine, Phys. Rev. Lett. **45**, 1446 (1980).

[118] E. W. Plummer and W. Eberhardt, Phys. Rev. B. **20**, 1444 (1979).

[119] E. Wimmer, A. J. Freeman, H. Krakauer, Phys. Rev. B. **30**, 3113 (1984).

[120] P. de Andrés, P. M. Echenique, and F. Flores, Phys. Rev. B. **35**, 4529 (1987).

[121] S. Gao and B. I. Lundqvist, Progr. Theoretical Phys. Suppl. **106**, 405 (1991).

[122] E. V. Chulkov, private communication.

[123] N. W. Ashcroft and N. D. Mermin, *Solid State Physics*, Saunders College, Philadelphia (1976).

[124] Th. Fauster, Appl. Phys. A **59**, 639 (1994).

[125] E. V. Chulkov, V. M. Silkin, and P. M. Echenique, Surf. Sci. **437**, 330 (1999).

[126] G. Leschik, R. Courths, H. Wern, S. Hüfner, H. Eckardt, and J. Noffke, Solid State Commun. **52**, 221 (1984).

[127] D. A. Papaconstantopoulos, *Handbook of the Band Structure of Elemental Solids*, Plenum Press, New York (1986).

[128] C. N. Berglund and W. E. Spicer, Phys. Rev. **136**, A1030 (1964).

Acknowledgements

First and foremost, I sincerely like to thank *Prof. Dr. Wolfgang Eberhardt*, who gave me the opportunity to perform this thesis in his institute. I gratefully acknowledge his continuous support and the inspiring and fruitful discussions concerning physical problems.

I am very grateful to *Prof. Dr. G. Hohlneicher* for his kindness to co-referee this thesis.

I also want to thank *Prof. Dr. G. Eilenberger* for his spontaneous readiness to assume the chair of the board of examiners.

A heartly thank you to *Dr. Hermann A. Dürr*. The work with him was always pure fun and I profited from his great knowledge and experience in physics. I also want to thank him for the thorough reading of this thesis.

I enjoyed the work together with *Prof. Dr. Neville V. Smith*. Many thanks for the fruitful ideas and support in finding an "universal rule" for the understanding of image-state lifetimes. The time he spent here in the institute has been full of pleasure and was -undoubtfully- too short.

Special thanks to *Heinz Pfeifer* and *Jürgen Lauer* for the permanent and immediate support by solving electronic, hard- and software problems. I want also to thank *Bernd Küpper* for the repair of several turbo-molecular pumps and support in the construction of UHV components. The work they do is uncountable and makes the work in the lab much easier. What would we do without them?

I am indebted to *Prof. Dr. E. V. Chulkov*, *Dr. V. M. Silkin* and *Prof. Dr. Pedro M. Echenique* for putting their calculations on the image states of Pt(111) at our disposal and for many fruitful discussions. I also want to thank *Prof. Dr. Stefan Blügel* and *Dr. Gustav Bihlmayer* for sharing their band-structure calculations for the Pt(111) surface with us.

Additional thanks to *Dr. Rainer Jacquemin* and *Dr. Andreas Scholl* for teaching me the basics of laser technology, TR2PPE and ultrafast phenomena, and to *Dr. Michael Löken* and *Dipl. Phys. Nikolaus Pontius* for the nice cooperation concerning the use of the laser system.

Furthermore, I want to thank *Jan Sievers* and *Dipl.-Phys. Hyoung Seub Rhie* for their assistance during some of the experiments.

Many thanks to *Jutta Gollnick* for keeping away administrative problems and for organising so many coffee breaks and meetings in the Pinocchio with subsequent dart tournaments in the Irish pub. In this context I also want to thank *Dr. Arne Dallmeyer* for giving me the opportunity to stay in the hotel "Dallmeyer" and introducing me into the history of the fictional city of Stenkelfeld.

Many, many thanks to all the members of the IEE group, who have not been mentioned here, for the warm welcome four years ago and the friendly and constructive atmosphere during the last years. Due to the wonderful time I have spent here, the time has run as fast as a quasiparticle exists and the first day seems not to be so far away.

I especially would like to thank my parents for the love, the freedom to decide what to do, and the support they gave me in the last 30 years. It has been a good feeling to know that there is someone who is always there for you. I also want to thank my grandparents for the wonderful relationship we always had throughout the years.

Finally, a heartly thank you to Sabine Böttcher for the uncountable beautyful moments in our common life.

Publication list

"The dimpling in the CuO_2 planes of $YBa_2Cu_3O_x$ (x = 6.806-6.984, T = 20-300 K) measured by Yttrium EXAFS"
J. Röhler, S. Link, K. Conder, and E. Kaldis, J. Phys. Chem. Solids **59**, 1925 (1998).

"Electron dynamics at a Ag/C_{60} metal-semiconductor interface"
S. Link, A. Scholl, R. Jacquemin, and W. Eberhardt, Solid State Commun. **113**, 689 (2000).

"Lifetimes of image-potential states on the Pt(111) surface probed by time-resolved two-photon photoemission spectroscopy"
S. Link, H. A. Dürr, and W. Eberhardt, Appl. Phys. A **71**, 525 (2000).

"Lifetimes of image-potential states on the clean and hydrogen-covered Ni(111) surface"
S. Link, J. Sievers, H. A. Dürr, and W. Eberhardt, J. Electron Spectrosc. Relat. Phenom. **114-116**, 351 (2001).

"Femtosecond electron dynamics of image-potential states on clean and oxygen-covered Pt(111)"
S. Link, H. A. Dürr, G. Bihlmayer, S. Blügel, W. Eberhardt, E. V. Chulkov, V. M. Silkin, and P. M. Echenique, Phys. Rev. B **63**, 115420 (2001).

"Femtosecond spectroscopy"
S. Link, H. A. Dürr, and W. Eberhardt, submitted to J. Phys.: Condens. Matter.

Forschungszentrum Jülich

Jül-3878
Juni 2001
ISSN 0944-2952